

60
7.1
P82
1982

THE DYNAMICS OF UNSTEADY STRAIT AND SILL FLOW

Lawrence J. Pratt

B.S., University of Wisconsin (1975)
M.S., University of Wisconsin (1977)

Submitted in Partial Fulfillment of the
Requirements for the Degree of
DOCTOR OF PHILOSOPHY

at the

Massachusetts Institute of Technology

and the

Woods Hole Oceanographic Institution

April, 1982

Signature of Author

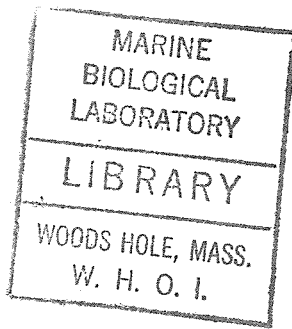
Joint Program In Oceanography, Massachusetts
Institute of Technology - Woods Hole Oceanographic
Institution, April, 1982.

Certified by

Thesis Supervisor

Accepted by

Chairman, Joint Committee for Physical
Oceanography, Massachusetts Institute of
Technology - Woods Hole Oceanographic
Institution.



i.

The Dynamics of Unsteady Strait and Sill Flow

by

Lawrence J. Pratt

Submitted to the Massachusetts Institute of Technology, Woods Hole Oceanographic Institution Joint Program in Oceanography on April 30, 1982, in partial fulfillment of the requirements for the Degree of Doctor of Philosophy.

Abstract

The dynamics of steady and unsteady channel flow over large obstacles is studied analytically and numerically in an attempt to determine the applicability of classical hydraulic concepts to such flows. The study is motivated by a need to understand the influence of deep ocean straits and sills on the abyssal circulation.

Three types of channel flow are considered: nonrotating one dimensional (Chapter 2); semigeostrophic, constant potential vorticity (Chapter 3); and dispersive, zero potential vorticity (Chapter 4). In each case the discussion centers around the time-dependent adjustment that occurs as a result of sudden obstruction of an obstacle into a uniform initial flow or the oscillatory upstream forcing of a steady flow over topography.

For nondispersive (nonrotating or semigeostrophic) flow, nonlinear adjustment to obstacle obstruction is examined using a characteristic formulation and numerical results obtained from a Lax-Wendroff scheme.

The adjustment process and asymptotic state are found to depend upon the height of the obstacle b_0 in relation to a critical height b_c and a blocking height b_b . For $b_0 < b_c < b_b$, isolated packets of nondispersive (long gravity or Kelvin) waves are generated which propagate away from the obstacle, leaving the far field unaffected. For $b_c < b_0 < b_b$, a bore is generated which moves upstream and partially blocks the flow. In the semigeostrophic case, the potential vorticity of the flow is changed by the bore at a rate proportional to the differential rate of energy dissipation along the line of breakage. For $b_b < b_0$ the flow is completely blocked.

Dispersive results in the parameter range $b_0 < b_c$ are obtained from a linear model of the adjustment that results from obstacle obstruction into a uniform, rotating-channel flow. The results depend on the initial Froude number F_d (based on the Kelvin wave speed). The dispersive modes set up a decaying response about the obstacle if $F_d < 1$ and (possibly resonant) lee waves if $F_d > 1$. However, the far-field upstream response is found to depend on the behavior of the nondispersive Kelvin modes and is therefore nil.

Nonlinear steady solutions to nondispersive flow are obtained through direct integration of the equations of motion. The characteristic formulation is used to evaluate the stability of various steady solutions with respect to small disturbances. Of the four types of steady solution, the one in which hydraulic control occurs is found to be the most stable. This is verified by numerical experiments in which the steady, controlled flow is perturbed by disturbances generated upstream. If the topography is

complicated (contains more than sill, say), then controlled flows may become destabilized and oscillations may be excited near the topography.

The transmission across the obstacle of energy associated with upstream-forced oscillations is studied using a reflection theory for small amplitude waves. The theory assumes quasi-steady flow over the obstacle and is accurate for waves long compared to the obstacle. For nonrotating flow, the reflection coefficients are bounded below by a value of $1/3$. For semigeostrophic flow, however, the reflection coefficient can be arbitrarily small for large values of potential vorticity. This is explained as a result of the boundary-layer character of the semigeostrophic flow.

ACKNOWLEDGEMENTS

I wish to thank Nelson Hogg, my advisor and friend, for his patient guidance and support throughout the development of the thesis. I also wish to give special thanks to Joseph Pedlosky for his encouragement and criticism during my days at Woods Hole and Chicago. I am also indebted to thesis committee members Erik Mollo-Christensen, Jack Whitehead, and Glen Flierl for their useful suggestions during preparation of the thesis, and to Mary Ann Lucas and Karin Bohr for help in preparing the manuscript.

Finally, I would like to thank Mindy for putting up with me during the final month before the defense.

TABLE OF CONTENTS

	Page
Abstract	i
Acknowledgements	iv
Chapter 1 Introduction	1
Chapter 2 The Unsteady Hydraulics of Nonrotating flow	7
2.1 Background and Equations	7
2.2 Weak Solutions	12
2.3 Adjustment of a Steady Flow to Small Disturbances	14
2.4 Upstream Influence in Quasi-linear Hyperbolic Systems..	22
2.5 Establishment of Steady Solutions	26
2.6 Unsteady Flow	37
2.7 Disruption of Control	44
2.8 Semi-steady Flow	49
2.9 Summary	53
Chapter 3 Unsteady Semigeostrophic Hydraulics	55
3.1 The Model	55
3.2 The Semigeostrophic Limit	57
3.3 Characteristics and Riemann Functions	60
3.4 Steady Solutions	62
3.5 The Location of the Critical Point and Multiple Bifuractions	64

	Page
3.6	Establishment of Steady Solutions 67
3.7	Free-surface Shocks 72
3.8	The Change in Potential Vorticity Across a Shock 79
3.9	Total Blockage of the Obstacle 85
3.10	Kelvin Wave Reflection 90
3.11	Self-excited Oscillations 97
Chapter 4	Dispersive Effects 100
4.1	Introduction 100
4.2	Adjustment in a Wide, Rotating Channel 103
Chapter 5	Summary 120
Appendices	
A	The Numerical Model 126
B	Proof that $G = 2[\delta^{-1/2}(T^{-1} - T^3)h + \delta^{-3/2}(T^3 - T)]$... 133
C	Computation of u and η from v 134
References 139

1. Introduction

The world's ocean is naturally divided into a set of basins which are interconnected by submarine passages, many of them narrow and containing shallow sills. These passages may play an important dynamical role in the abyssal circulation by exercising hydraulic control in the same way that a dam controls the upstream level of a reservoir. This is suggested by the sharp drop in isotherm level that is often observed downstream of a sill and which resembles the surface configuration of water flowing over a dam (see Figure 1.1, for example).

The concept of hydraulic control has a basis in classical (and primarily one-dimensional) problems in free surface and high speed flow. A discussion of the hydraulics of open-channel flow can be found in the textbook of Chow (1959). 'Control' is said to occur when an obstacle or contraction influences conditions in the far field. In the ocean, the 'far field' refers to the basins which lie upstream and downstream of the dividing passage. To understand the hydraulics of deep strait and sill flow, the classical hydraulics theories must be extended to include complications such as rotation, stratification, friction, and time dependence which influence the abyssal circulation. Such extensions are difficult, however, since control is a nonlinear phenomenon and models of ocean currents which, say, linearize about a mean flow or bottom topography are inherently unsatisfactory.

A great deal of work has been devoted to the study of geophysical flows over large obstacles. The subject arises in mountain meteorology and a review of the associated literature has been given by Smith (1979).

The subject of selective withdrawal from reservoirs is also relevant, and much of the associated literature has been reviewed by Fandry, et al. (1977).

However, the problem of deep strait and sill flow presents a feature unaccounted for in most prior research. In particular, rotation occurs in combination with side wall effects. The first to investigate this complication were Whitehead, et al. (1974) who found nonlinear solutions for a channel flow with zero potential vorticity. A criterion for hydraulic control of the flow was put forth on the basis of a minimization principle. Gill (1977) later extended this theory to include finite (but constant) potential vorticity flows and clarified the use of the minimization principle. At present, it is possible to describe the hydraulics of a continuous, steady stream with constant potential vorticity as it passes through a slowly varying channel. The conditions for the stability of such a stream are unknown, but the problem is presently under investigation.⁺

One aspect of rotating hydraulics (and hydraulics in general) which has received little attention is time dependence. This is odd, since time dependence is implicit in the definition of hydraulic control. In classical hydraulics 'control' implies a permanent response upstream to a small change in the geometry of the conduit. The response must, of course, be set up by some sort of time-dependent adjustment. This idea was established by Long (1954), who towed an obstacle through a tank of

⁺ Griffiths, Killworth and Stern (1982), submitted to Geophysical and Astrophysical Fluid Dynamics.

fluid and measured the response set up ahead of the obstacle. For obstacle heights less than some minimum height, the fluid away from the obstacle was disturbed temporarily by the passage of long gravity waves generated during the initial acceleration of the obstacle. After passage of these waves the fluid returned to its initial state. For obstacle heights greater than the minimum height, however, the flow away from the obstacle was permanently altered by the generation of a bore which moved ahead of the obstacle, leaving behind an altered state.

Long's results indicate that the presence of the obstacle in a steady flow is either (1) felt nowhere away from the obstacle; or (2) felt everywhere away from the obstacle. We would like to know whether or not such dramatic differences are typical of the way in which deep strait and sills influence flow in the upstream basin. We would also like to know how such flows adjust to sudden changes in topography, whether or not bores are important and, if so, how they alter the initial flow. Finally, we would like to know what the downstream response is to sudden changes in geometry. (Historically, it is the upstream response that has been emphasized.)

Although time dependence is implicit in the classical ideas about control of steady flows, it is not clear whether these ideas hold if the basic flow is unsteady. How stable, for example, is the hydraulically controlled state to time-dependent forcing and how are the forced waves affected by the strait or sill? How are the unsteady flow fields upstream and downstream of an isolated obstacle influenced by the height of the obstacle? These questions are relevant to deep strait and sill flow, as

indicated in the deep current meter records from the Denmark Strait and Jungfern Passage (Figure 1.2). Both of these deep passages serve as conduits for the transfer of bottom water between basins, and it can be seen that the velocity records are dominated by unsteady motions.

The purpose of this work is to explore the influence of time dependence on the hydraulics of deep strait and sill flow. It is clear that this subject is important to the understanding of the steady hydraulics of these flows as well as the response to unsteady forcing. Two types of problems will therefore be emphasized. The first involves time-dependent adjustment of a deep current to isolated topography. The second involves the subjection of a steady, hydraulically controlled flow to periodic disturbances.

Chapter 2 is devoted to one-dimensional nonrotating flows. The classical problem of hydraulic control by an obstacle is reviewed and a characteristic formulation is introduced which allows for an interpretation of time-dependent hydraulic effects and flow stability. We next review, through a numerical experiment, the establishment of steady solutions by time-dependent adjustment to an obstacle. Included is a discussion of some previously unexplored aspects of the problem involving the dependence of the solution on the initial data. The remainder of Chapter 2 is devoted to oscillatory flows which are set up by some type of unsteady upstream forcing. The applicability of the ideas of steady hydraulics are explored using both the characteristic formulation and the numerical model. The reverse problem -- that of wave propagation in a controlled flow -- is also explored.

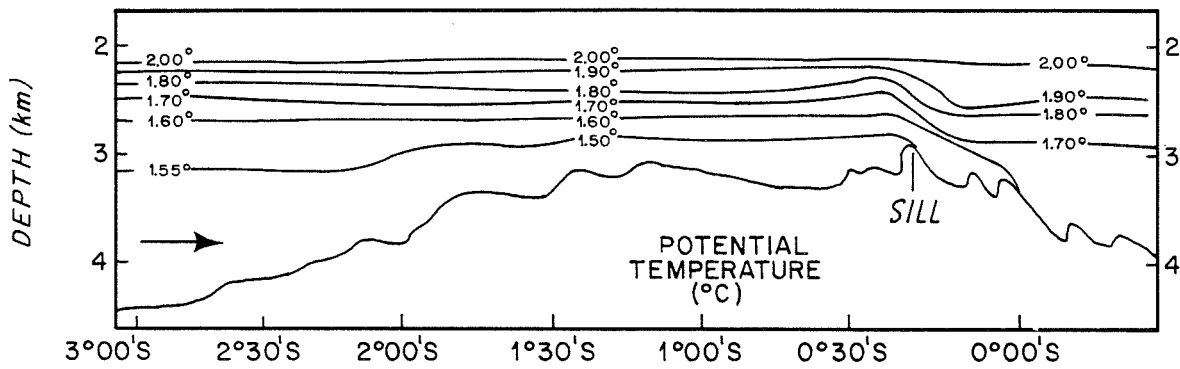
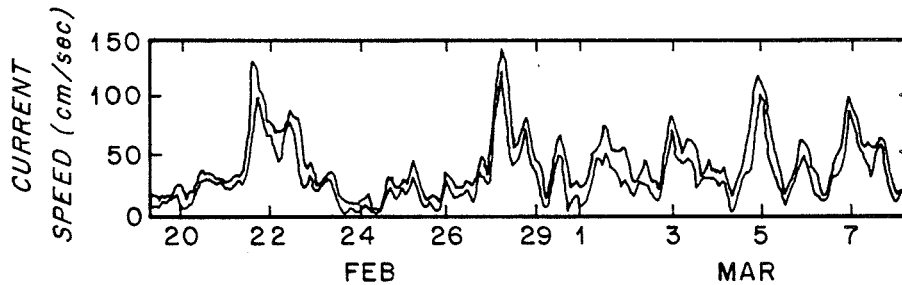
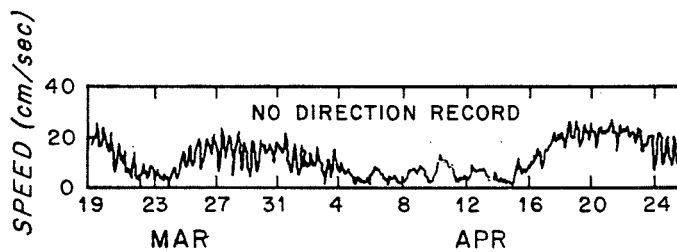


Figure 1.1

Potential temperature along the axis of the Ecuador Trench (after Lonsdale, 1974).



(a)



(b)

Figure 1.2

Current meter records from (a) the Denmark Strait (after Worthington, 1969) (b) the Jungfern Passage (after Stalcup, 1975).

Chapter 3 is devoted to the time-dependent hydraulics of semigeostrophic flow in a channel. The discussion proceeds along the same lines as Chapter 2 although the treatment of periodic flows is more limited due to numerical difficulties. The constant potential vorticity solutions of Gill (1977) in a channel with both width contractions and bottom topography are introduced in the first section and some additional remarks concerning this theory are made. A characteristic formulation of the semigeostrophic problem is then introduced and this allows for the same interpretations of unsteady hydraulic effects and stability which were made earlier. Next, the problem of semigeostrophic adjustment to an obstacle is treated numerically and we discuss some questions concerning free surface shocks that are raised by the results. This is followed by a treatment of the influence of the obstacle on Kelvin waves generated upstream. The chapter ends with an example in which waves are excited as a result of the interaction of a steady flow with unusual topography.

Chapter 3 establishes a clear connection between the properties of semigeostrophic flows and the hydraulics of more classical flows. This connection is due primarily to the fact that, as in the classical case, a semigeostrophic flow supports only nondispersive waves. In Chapter 4 we relax this restriction, and ask how the ideas of control and upstream influence are altered when dispersive waves are present. The discussion again centers around time-dependent adjustment of a channel flow to an obstacle.

2. The Unsteady Hydraulics of Nonrotating Flow

2.1 Background and Governing Equations

In all that follows we make use of the fact that deep strait and sill flow, like other large scale ocean currents, have depth scales several orders of magnitude smaller than their horizontal scales, so that the hydrostatic approximation can be made. Furthermore, we avoid the problem of continuous stratification by assuming the flow to be confined to a deep single layer of constant density ρ_1 and that the lighter inactive fluid above has constant density ρ_2 . Under these conditions the inviscid flow in the lower layer is described by the shallow-water equations (Pedlosky, 1979):

$$u_t + uu_x + vu_y - fv = -g'h_x - gb_x$$

$$v_t + uv_x + vv_y + fu = -g'h_y - gb_y$$

$$h_t + (uh)_x + (vh)_y = 0$$

where $g' = g(\rho_1 - \rho_2)/\rho_1$ is a reduced gravity. Here, x and y are east and north coordinates and u and v corresponding velocities. The thickness of the lower layer is denoted by h and the elevation of the bottom by b .

The flow will be confined to a channel aligned in the x -direction (see Figure 3.1). The channel bottom will vary in the x -direction on a horizontal scale L . The width of the channel will have horizontal scale W while the depth and bottom elevation will have vertical scale D . Based on these, we choose the horizontal velocity scales as $U = (g'D)^{1/2}$ and $V = UW/L$. The former scaling implies that the advective terms in the x -momentum equation are important and is consistent with the observed

scales of many deep strait and sill flows (see Lousdale (1969), for example).

Dimensionless variables are now chosen as

$$x' = x/L, \quad y' = y/W, \quad t' = t(g'D)^{1/2}/L,$$

$$u' = u/U = u/(gD)^{1/2}, \quad v' = v/V = vL/(g'D)^{1/2}W,$$

$$h' = h/D, \quad b' = b/D.$$

substituting these into the shallow-water equations and dropping primes, we find the following dimensionless set of equations:

$$u_t + uu_x + vu_y - Fv = -h_x - b_x \quad (2.1.1a)$$

$$\delta^2(v_t + uv_x + vv_y) + Fu = -h_y - b_y \quad (2.1.2a)$$

$$h_t + (uh)_x + (vh)_y = 0 \quad (2.1.3a)$$

where

$$\delta = W/L = (\text{horizontal aspect ratio})$$

and

$$F = Wf/(g'D)^{1/2} \quad (\text{width scale/Rossby radius of deformation})$$

Solutions to (2.1.1a-2.1.3a) will be discussed according to the following program:

$$\text{Chapter 1: } \delta \ll 1, \quad F \ll 1, \quad \frac{\partial}{\partial y} = 0$$

$$\text{Chapter 2: } \delta \ll 1, \quad F = 0(1), \quad b_y = 0$$

$$\text{Chapter 3: } \delta = 0(1), \quad F = 0(1)$$

We start by considering the first parameter range, for which the flow is one dimensional and nonrotating (see Figure 2.1). The governing equations are

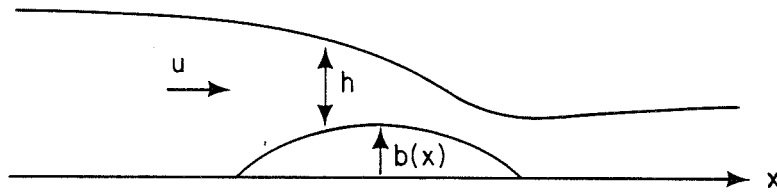


Figure 2.1
Definition sketch.

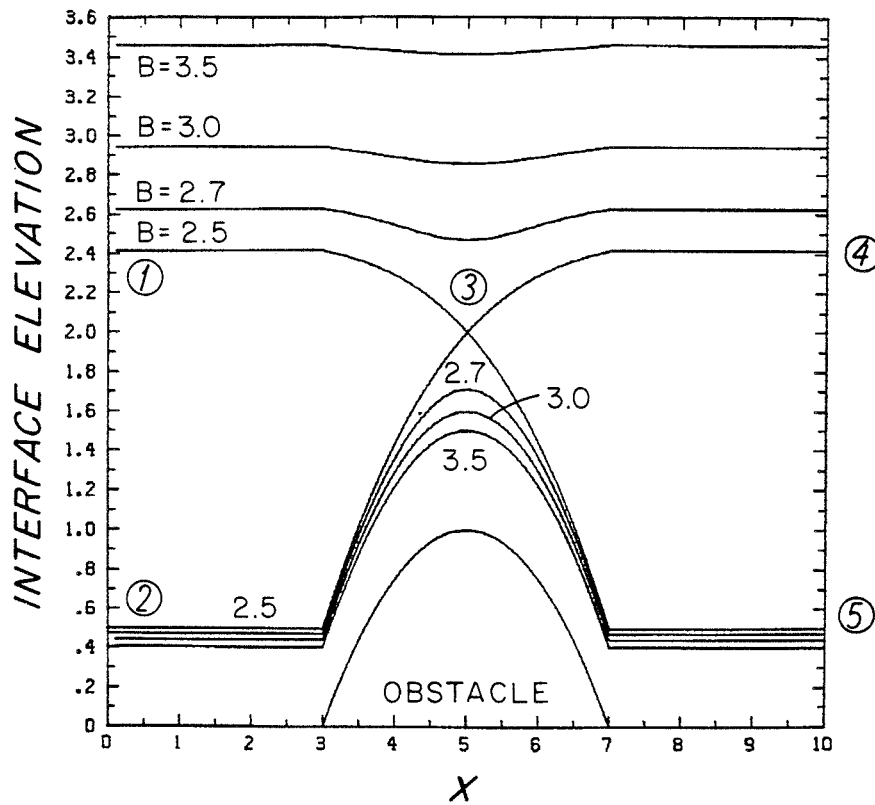


Figure 2.2

Steady surface profiles for $Q = 1$, $b_0 = 1$.

$$u_t + uu_x + h_x = - \frac{db}{dx} \quad (2.1.1)$$

$$h_t + (uh)_x = 0 . \quad (2.1.2)$$

Equations (2.1.1) and (2.1.2) have been studied extensively in connection with open-channel hydraulics (Chow, 1959) and shallow-water waves (Stoker, 1957). Steady solutions can be found by direct integration with respect to x , resulting in

$$\frac{u^2}{2} + h + b = B = (\text{flow energy/unit mass}) \quad (2.1.3)$$

$$uh = Q = (\text{flow rate}) , \quad (2.1.4)$$

and these can be combined into a single equation for the fluid depth:

$$\frac{Q^2}{2h^2} + h + b = B . \quad (2.1.5)$$

A family of interface elevation curves are drawn in Figure 2.2 for flow over an isolated obstacle. The flow rate Q is held constant while the Bernoulli constant B is allowed to vary. It can be seen that two distinct solutions exist for each large value of B and that each maintains the same depth on either side of the obstacle. As B is reduced, however, a critical value ($B = 2.5$) is reached at which the two curves coalesce over the sill of the obstacle. Here it is not obvious which branch is correct. After moving along the interface curve from ① to ③, for example, it is not clear whether one should proceed to ④ or ⑤. Based on physical intuition we would likely choose ⑤ since this branch resembles the commonly observed configuration of fluid flowing over a dam or weir.

If B is further reduced the solutions no longer extend across the entire obstacle. The energy of the flow has been reduced to the point where the fluid is unable to surmount the sill. The solution for $B = 2.5$ contains the minimum energy necessary and is therefore 'controlled' in the sense that a small increase in the sill height would necessitate a time-dependent change in the upstream conditions for flow to continue. Such upstream influence would not be necessary for the other continuous solutions since they contain energy in excess of the required amount.

The steady solutions of Figure 2.2 also have distinguishing properties in terms of wave propagation. The only small-amplitude waves allowed by (2.1.1) and (2.1.2) are long gravity waves with speeds

$$\lambda_{\pm} = u \pm (h)^{1/2} \quad (2.1.6)$$

At the coalescence point (labeled ③ in Figure 2.2) the Bernoulli constant B has the minimum for all the profiles, $\frac{\partial B}{\partial h} = 0$. It follows from (2.1.3) and (2.1.4) that the flow there is critical ($\lambda_- = 0$). Using u_c, h_c to denote the flow at the critical point, it also follows from (2.1.6) that

$$u_c = h_c^{1/2}, \quad (2.1.7)$$

and from (2.1.4) that

$$Q = h_c^{3/2}, \quad (2.1.8)$$

so that

$$\lambda_- = \frac{h_c^{3/2}}{h} - h^{1/2} = h^{1/2} \left(\frac{h_c^{3/2}}{h^{3/2}} - 1 \right)$$

It is further evident from the latter relation that the flow is subcritical ($\lambda_- < 0$) for $h > h_c$ and supercritical ($\lambda_- > 0$) for

$h < h_c$. Along interface ① - ⑤, for example, the flow is subcritical between ① and ③. The solutions which lie above interface ① - ③ - ④ are completely subcritical, while those lying below ② - ③ - ⑤ are completely supercritical.

There exists a relation between the principle of upstream influence and the presence of a critical point and this will be explored in section 2.3.

2.2 Weak Solutions

We would like to know how the steady solutions of the last section undergo time-dependent adjustment to some sort of disturbance. The disturbance might take the form of a sudden change in the upstream conditions or change in the topography of the obstacle. Since the hydrostatic assumption implicit in Equations (2.1.1) and (2.2.2) permits nonlinear steepening but not dispersion (Stoker, 1957), it is expected that this adjustment might result in wave breakage. We seek to describe the resulting discontinuities, or shocks, as 'weak' solutions in which the flow fields satisfy (2.1.1) and (2.1.2) at all but a finite number of points. At these points the height and velocity and their derivatives can be discontinuous, at least in the shrunken horizontal space of the shallow water approximation. In reality, the shocks occur over small but finite regions in which the shallow approximation breaks down. One example is the common hydraulic jump.

How does one connect the upstream and downstream states across a shock? Even in the presence of nonhydrostatic and viscous forces, the fluid

contains no internal sources of momentum or mass.[†] We can therefore integrate the continuity and momentum equations (in their conservation law form) across the shock. Upon doing so and shrinking the interval of integration to zero we find the Rankine-Hugoniot conditions (Stoker, 1957):

$$c \begin{bmatrix} h \\ \end{bmatrix}_{A B} = \begin{bmatrix} uh \\ \end{bmatrix}_{A B} \quad (2.2.1)$$

$$c \begin{bmatrix} uh \\ \end{bmatrix}_{A B} = \begin{bmatrix} u^2 h + h^2/2 \\ \end{bmatrix}_{A B}, \quad (2.2.2)$$

where $\begin{bmatrix} \\ \end{bmatrix}_{A B}$ denotes the jump from $x = A$ to $x = B$ and c is the propagation speed of the shock. The steps leading to (2.2.1) and (2.2.2) are worked out in Section 3.7 in connection with more general, two dimensional shocks.

If c , u_A , and h_A are known then (2.2.1) and (2.2.2) provide two equations for u_B and h_B . These can be combined to form a cubic equation for h_B containing at most two real roots -- one corresponding to a drop in depth, the other an increase in depth. It can further be shown that the rate of energy dissipation per unit mass of fluid crossing the jump from side 'A' to side 'B' is as given by (Rayleigh, 1914)

$$\frac{dE}{dt} = \frac{m (h_A - h_B)^3}{h_A h_B}, \quad (2.2.3)$$

where $m = h_A(u_A - c) = h_B(u_B - c)$.

[†] The conservation of mass within the shock is, of course, exact. The fluid may, however, gain momentum from viscous boundary layer or topographic effects at a rate proportional to the distance over which the shock is smeared.

Since viscous effects act as energy sinks through the generation and dissipation of turbulence and small waves, we demand that a fluid parcel passing through the shock lose energy. Equation (2.2.3) then demands that the parcel's depth should increase upon passing the shock and this determines the appropriate root.

2.3 Adjustment of a Steady Flow to Small Disturbances

The remark has been made that hydraulically controlled flows are distinguished by the way they adjust to changes in obstacle height. We would now like to ask how this adjustment occurs and what the relevance of the critical condition is.

We are therefore posed with an initial value problem in which one of the steady solutions to (2.1.1) and (2.1.2) is perturbed by a sudden change in topography. A convenient method of solving such a problem is provided by characteristics and characteristic equations. Multiplying (2.1.2) by $h^{-1/2}$ and adding the result to (2.1.1) gives

$$\left(\frac{\partial}{\partial t} + \lambda_+ \frac{\partial}{\partial x}\right)u + h^{-1/2} \left(\frac{\partial}{\partial t} + \lambda_+ \frac{\partial}{\partial x}\right)h = -\frac{db}{dx}$$

where λ_+ given by (2.1.6). Subtracting the product of $h^{-1/2}$ and (2.1.2) from (2.1.1) leads to

$$\left(\frac{\partial}{\partial t} + \lambda_- \frac{\partial}{\partial x}\right)u - h^{-1/2} \left(\frac{\partial}{\partial t} + \lambda_- \frac{\partial}{\partial x}\right)h = -\frac{db}{dx}.$$

These equations can be written in the more compact forms

$$\frac{d_+ u}{dt} + h^{-1/2} \frac{d_+ h}{dt} = \frac{-db}{dx}, \quad (2.3.1)$$

and

$$\frac{d_- u}{dt} - h^{-1/2} \frac{d_- h}{dt} = \frac{-db}{dx}, \quad (2.3.2)$$

where the operator

$$\frac{d_{\pm}}{dt} = \frac{\partial}{\partial t} + (u \pm h^{1/2}) \frac{\partial}{\partial x} \quad (2.3.3)$$

denotes differentiation following a wave with speed $dx_{\pm}/dt = \lambda_{\pm} = (u \pm h^{1/2})$. The characteristic curves, $x_{\pm}(t)$, map out the paths of wavelets as they carry information along the channel.

Equations (2.3.1) and (2.3.2) determine the evolution of u and h along characteristic curves $x_{\pm}(t)$. A simpler form can be achieved if it is noted that $h^{-1/2}dh/dt = d(2h^{1/2})/dt$ in (2.3.1) and (2.3.2). This leads to evolution equations for the Riemann functions defined by

$$\frac{d_+}{dt} (u + 2h^{1/2}) = \frac{d_+ R_+}{dt} = \frac{-db}{dx}, \quad (2.3.4)$$

and

$$\frac{d_-}{dt} (u - 2h^{1/2}) = \frac{d_- R_-}{dt} = \frac{-db}{dx}. \quad (2.3.5)$$

The Riemann functions, R_{\pm} , are therefore invariant along appropriate characteristics if the channel bottom is flat.

If R_{\pm} are known then height and velocity fields can be determined from them through

$$u = \frac{1}{2} (R_+ + R_-) \quad (2.3.6)$$

$$h = \frac{1}{16} (R_+ - R_-)^2. \quad (2.3.7)$$

Given initial data along some line OQ (Figure 2.3a) not a characteristic, we can integrate (2.3.4, 5) or (2.3.1, 2) along characteristics which intersect OQ to find a solution in the region POQ . Furthermore, the information specified along OQ will continue to propagate away from POQ along characteristics which cross characteristics OP and QP .

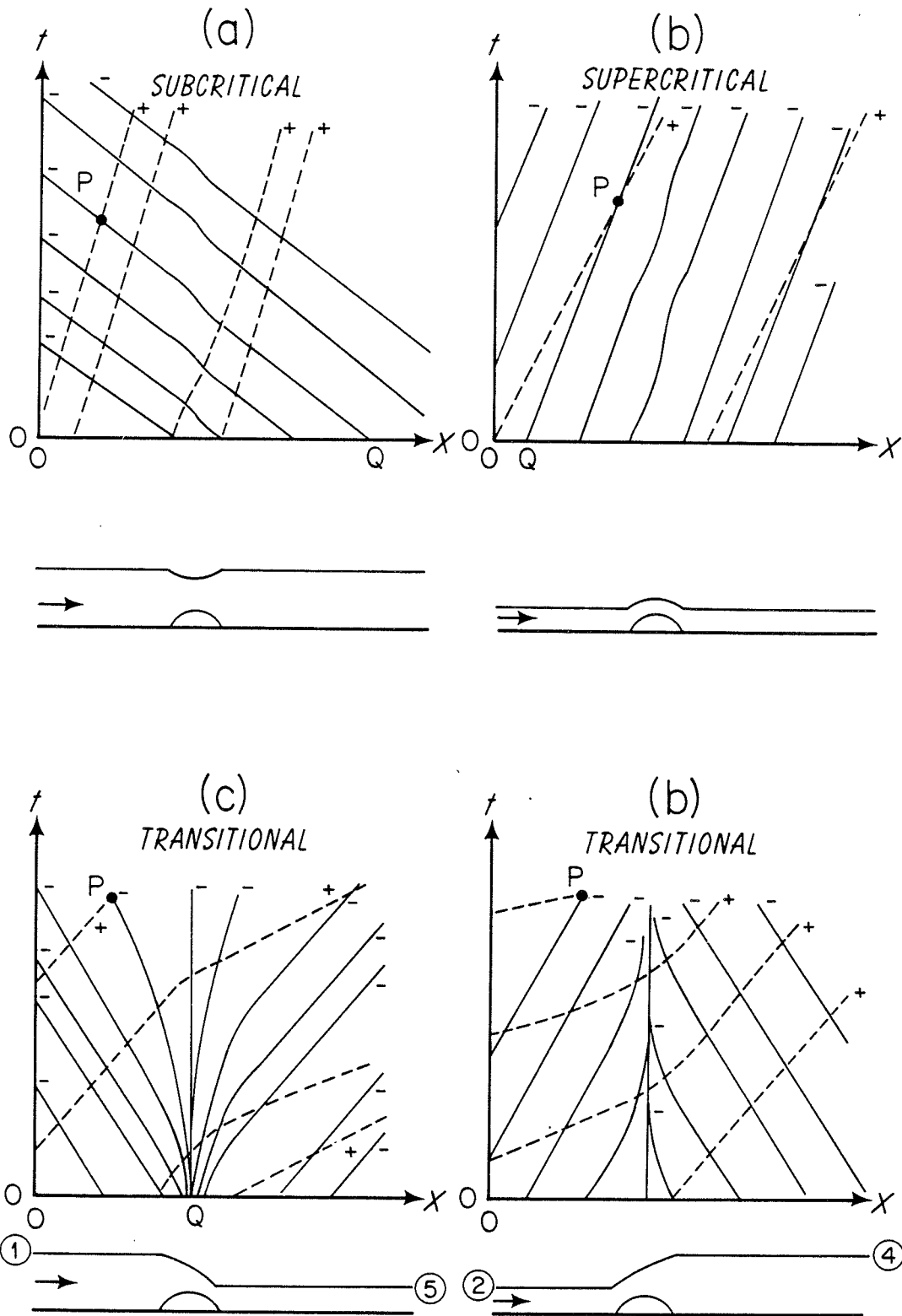


Figure 2.3

Characteristic curves for each of the four types of steady flows.

Now consider the general pattern of characteristics for each of the four types of steady solution. These have been drawn in Figure 2.3. For subcritical flow the x_- characteristics tilt upstream and the x_+ characteristics downstream, while for supercritical flow both sets of characteristics tilt downstream. In either case a small disturbance generated over the sill will propagate away from the obstacle as two separate packets.

For transitional flow (Figures 2.4 c,b) the slope of the x_- characteristics depends upon position relative to the obstacle. At the sill the flow is critical, so that the x_- characteristic is vertical there. In the (1) - (5) case (Figure 2.3c) the neighboring x_- characteristics diverge as the sill acts as a source of characteristics for the far field. The x_- packet synthesized by raising the sill a small amount therefore spreads out, eventually covering the entire channel. In the (2) - (4) solution, however, the characteristics converge over the obstacle and x_- waves tend to become focused about the sill. Apparently, this branch is unstable.

We see that there is a fundamental difference between the way that transitional and nontransitional solutions adjust, and that this difference is related to the existence of a critical point. We now attempt to quantify this idea in terms of the upstream influence that the disturbance has. Consider the flow at a point P upstream of the obstacle long after the disturbance has been generated and a new steady state established (see Figure 2.3a). Let the Riemann functions be partitioned into undisturbed values \bar{R}_\pm plus time-dependent deviations r_\pm

associated with the disturbance. The values of \bar{R}_{\pm} are determined by the initial ($t = 0$) data and r_{\pm} are zero at $t = 0$. The upstream influence of the obstacle is then measured in terms of $r_{p\pm}$: the changes in the Riemann invariants at the point P after a new steady state is reached. The new values of the Riemann invariants can be translated into new heights and velocities using (2.3.6) and (2.3.7).

The values of $r_{p\pm}$ can be obtained by replacing R_{\pm} by $\bar{R}_{\pm} + r_{\pm}$ in (2.3.4) and (2.3.5) and integrating along appropriate characteristics $Q'P$ and $O'P$ (see Figure 2.4 a,b). Using the fact that $r_{0'+} = r_{Q'+} = 0$, we obtain

$$r_{p-} = (\bar{R}_{Q'} - \bar{R}_P) - \int_{Q'}^P \frac{db'}{dx} dt' \quad (2.3.8)$$

$$r_{p+} = (\bar{R}_{O'} - \bar{R}_P) - \int_{O'}^P \frac{db'}{dx} dt' \quad (2.3.9)$$

where $\frac{db'}{dx}$ is the slope of the new topography. The integration paths should be distinguished from the characteristics PQ and PO that would be appropriate in the absence of a disturbance. Since the channel bottom is flat between O' and P, $\bar{R}_{O'} = \bar{R}_P$ and $\int_{O'}^P \frac{db'}{dx} dt' = 0$. Thus $r_{p+} = 0$ and the upstream influence is entirely due to r_{p-} .

Let us examine (2.3.8) first for the subcritical and supercritical cases (Figures 2.4 a,b). Since the initial flow is steady, the depth and velocity on either side of the obstacle is identical. Therefore $\bar{R}_P = \bar{R}_Q = \bar{R}_{Q'}$, and (2.3.8) reduces to

$$r_{p-} = - \int_{Q'}^P \frac{db'}{dx} dt'$$

in either case. If the flow is supercritical then the characteristic PQ' lies entirely over flat bottom and this integral vanishes. If the flow is subcritical, then (2.1.5) implies that the new steady solution that is established is a single-valued function of b' alone and

$$r_{p-} = - \int_{Q'}^P \frac{db'}{dx} dt' = - \int_{Q'}^P \frac{db'}{dx/dt'} = - \int_0^0 \frac{db'}{\lambda_-(b')} = 0.$$

Thus, the upstream influence is zero in either case.

The first transitional case (Figure 2.2c) is somewhat more subtle. First consider (2.3.8) when no disturbance is present (i.e. $b' = b$, $r_{\pm} = 0$, $Q' = Q$, and Q lies close to the sill). Since $r_{p-} = 0$ we have

$$\bar{R}_P - \bar{R}_Q = - \int_Q^P \frac{db}{dx} dt,$$

both sides being finite.

Now suppose that the flow is disturbed (Figure 2.4c). The x_- characteristic passing through P will still originate from near the sill; that is, $Q > Q'$ as the point P is moved toward $t = \infty$ while x is kept fixed, and $R_P - R_Q$ will remain unchanged. We can therefore rewrite (2.3.8) as

$$r_{p-} = \int_Q^P \frac{db}{dx} dt - \int_{Q'}^P \frac{db'}{dx} dt', \quad (2.3.9a)$$

where dt is taken along the undisturbed characteristic between Q and P , and dt' is taken along the new characteristic (that also spans Q and P). For $b \neq b'$ the above expression will be nonzero in general and upstream influence will be present.

With slight modification, the above arguments can be made for P taken downstream of the obstacle. We therefore eschew the traditional term

Figure 2.4

Perturbed and unperturbed X_+ characteristics.

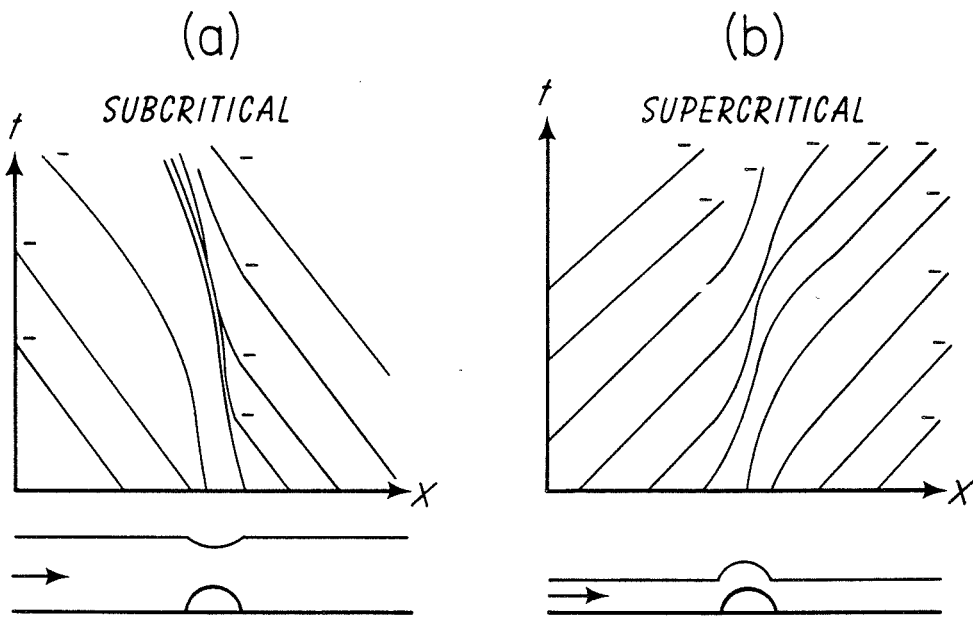
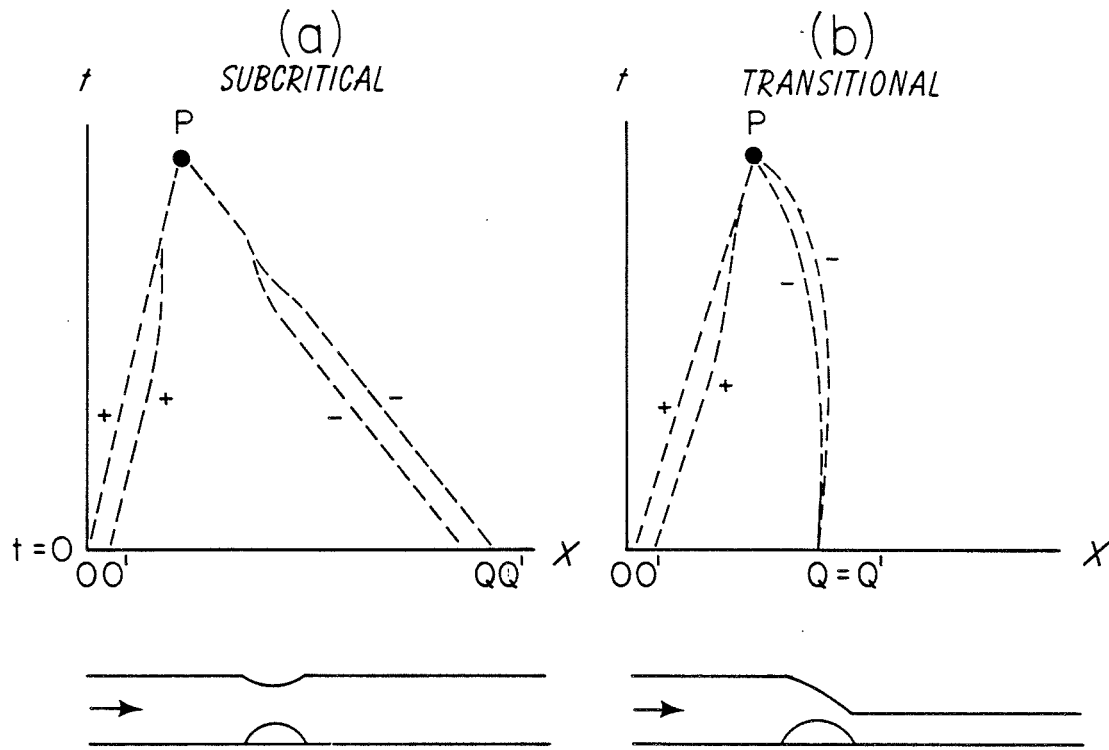


Figure 2.5

X_+ characteristic curves for nearly critical flows.

'upstream influence' in favor of the term 'far-field' influence so that the upstream and downstream fields are both considered. Thus far, the 'far field' includes any point away from the obstacle. That is, the response as $t \rightarrow \infty$ at a point near the obstacle is identical to the response far from the obstacle. It remains to be seen whether further complications will cause responses which vary with the distance from the obstacle.

The above analysis assumes that the general pattern of characteristics remains unaltered by the change in topography. This does not apply to the second transitional flow (Figure 2.3d) which has been postulated to be unstable. A small change in the sill height here might lead to large distortions in the field of characteristics. Upon closer inspection of Figures 2.3a and 2.3b, we see that circumstances may arise which render subcritical and supercritical flows unstable as well. Suppose that the flow is initially supercritical or subcritical but that conditions over the sill are nearly critical. The corresponding characteristics are sketched in figure 2.5. In the subcritical case the x_- modes synthesized downstream of the sill will tend to become focused about the sill. The same happens in the supercritical case to x_- modes generated upstream. Both of these flows appear to become less stable as conditions near the sill approach criticality.

It should also be noted that no such behavior is possible for the first transitional flow (Figure 2.3c). This configuration appears to be the most stable of the four.

2.4 'Far-Field Influence' in Quasi-linear Hyperbolic Systems.

In the previous section we drew a connection between criticality and the idea of far-field influence. This was made possible by the characteristic formulation in which solutions to initial-value problems are obtained through integration along wave paths. A generalization should then be possible for two-dimensional hyperbolic systems since, by definition, initial value problems are solved in the same way.

Consider the quasi-linear system of equations

$$\frac{\partial}{\partial t} u_i(x,t) + a_{ij}(u_i, x, t) \frac{\partial u_j}{\partial x}(x,t) = b_i(u_i, x, t) \quad \begin{array}{l} i = 1, n \\ j = 1, n \end{array} \quad (2.4.1)$$

where a_{ij} and b_i are single valued and continuous. Following Whitham (1974), Chapter 5, we wish to investigate the conditions under which (2.4.1) can be expressed in the same form as (2.3.1) or (2.3.2); that is, the form

$$l_i \frac{d^{(n)} u_i}{dt} = l_i b_i \quad (2.4.2)$$

where $\frac{d^{(n)}}{dt} = \left(\frac{\partial}{\partial t} + \lambda_{(n)}(u_i, x, t) \frac{\partial}{\partial x} \right)$ is a derivative along some curve with real slope $\frac{dx}{dt} = \lambda_{(n)}$.

It is clear that such a form exists if a vector l_i can be found such that

$$l_i a_{ij} = \lambda_{(n)} l_j \quad (2.4.3)$$

for (2.4.1) can then be multiplied by l_i to yield (2.4.2):

$$\begin{aligned} l_i \frac{\partial}{\partial t} u_i(x,t) + l_i a_{ij} \frac{\partial u_j}{\partial x} &= l_i \frac{\partial}{\partial t} u_i(x,t) + l_i \lambda_{(n)} \frac{\partial u_i}{\partial x} \\ &= l_i \frac{d^{(n)} u_i}{dt} = l_i b_i \end{aligned}$$

If l_i is a function of u_i alone, a Riemann function R which satisfies

$$\frac{\partial R}{\partial u_i} = l_i \quad (2.4.4)$$

may be found. In this case (2.4.2) can be written in the simplified form

$$\frac{d_{(n)}R}{dt} = l_i b_i .$$

The Riemann function is invariant along characteristics if the 'forcing' $l_i b_i$ is zero.

In order for (2.4.3) to be satisfied the eigenvalue, $\lambda_{(n)}$, must satisfy

$$a_{ij} - \lambda_{(n)} \delta_{ij} = 0 . \quad (2.4.5)$$

We note that if a_{ij} is constant and $b_i = 0$ then solutions to (2.4.1) of the form

$$u_i = A_i e^{ik(x - \lambda_{(n)}t)}$$

exist, provided that (2.4.5) is satisfied. The $\lambda_{(n)}$ are therefore called characteristic speeds.

If n real values of λ can be found to satisfy (2.4.5) then n linearly independent equations of the form (2.4.2) can be written and the initial-value problem solved in the way suggested above. Under these conditions, the system (2.4.1) is hyperbolic and steady solutions containing critical points ($\lambda_n = 0$) may display far field influence. This will occur if the characteristics diverge from the critical point, thereby connecting the far field to a single point.

In the steady solutions of Figure 2.2c the flow at the bifurcation is critical. Is this a general property of bifurcations of steady flows? Using (2.4.1) the derivatives of the dependent flow variables can be expressed using Kramer's Rule in terms of u_i and x as

$$\frac{\partial u_i}{\partial x} = \frac{|a_{ij}|_i}{|a_{ij}|}, \quad (2.4.6)$$

where $|a_{ij}|_i$ is the determinant obtained from a_{ij} by replacing the i^{th} column with b_i . If the solution bifurcates at some point x_c , either $\partial u_i / \partial x$ or one of its higher derivatives becomes multivalued.

Suppose first that $\partial u_i / \partial x$ becomes multivalued, so that the right side of (2.4.6) must be also. Yet each element of a_{ij} and b_i , and therefore each determinant, is single valued. The only possibility for multivaluedness is for

$$|a_{jk}| = 0 \quad (2.4.7)$$

and

$$|a_{jk}|_i = 0. \quad (2.4.8)$$

The first result together with (2.4.5) implies that one characteristic speed must be zero. The second gives a connection between the bifurcation point and the inhomogeneous term b_i .

It is also possible that a higher derivative of u_i , and not $\partial u_i / \partial x$, is multivalued. In this case differentiation of (2.4.6) yields the condition that $\partial^n u_i / \partial x^n$ is multivalued if and only if $\partial^{n-1} u_i / \partial x^{n-1}$ is. Thus (2.2.1) and (2.2.2) are applicable in all cases.

As an example, let us apply the general theory to the shallow flow under consideration. Here,

$$u_i = (u \ h) \quad a_{ij} = \begin{pmatrix} u & -1 \\ h & u \end{pmatrix} \quad b_i = \left(\frac{db}{dx} \quad 0 \right) .$$

The characteristic speeds are obtained through the use of (2.4.5):

$$\lambda_+ = u + h^{1/2} ,$$

and

$$\lambda_- = u - h^{1/2} .$$

Equation (2.4.3) then gives the eigenvectors l_+ and l_- within a multiplicative constant. One choice is

$$l_+ = (1, h^{-1/2}) ,$$

$$l_- = (1, -h^{-1/2}) .$$

Multiplying equations (2.1.1) and (2.1.2) by these gives the characteristic equations:

$$\frac{d_+ u}{dt} + h^{-1/2} \frac{d_+ h}{dt} = \frac{-db}{dx} ,$$

$$\frac{d_- u}{dt} - h^{-1/2} \frac{d_- h}{dt} = \frac{-db}{dx} .$$

Finally, (2.4.7) requires that bifurcations of steady solutions must occur when $c_- = 0$, while (2.4.8) further demands that any such point must occur where

$$\begin{vmatrix} b' & -1 \\ 0 & u \end{vmatrix} = \begin{vmatrix} u & b' \\ h & 0 \end{vmatrix} = 0 ,$$

that is, when $b' = 0$.

The steady solutions of this example are subject to far field influence only if a critical condition exists. We should hasten to add that this is not a general property of hyperbolic systems. For example,

in a channel flow with quadratic bottom friction (i.e., $b_f = [-db/dx - (c_f u^2/h + 0)]$),[†] the Riemann functions are nowhere conserved. The arguments of the previous section indicate that far field influence will be present for any steady configuration. Physically speaking, any change in an obstacle's height causes a change in the net frictional force exerted by the obstacle against the upstream flow.

2.5 Establishment of Steady Solutions

The adjustment of a stable steady flow to a small change in topography is convenient to analyze because the basic pattern of characteristics remains fixed. What adjustment occurs when the initial flow is unstable, or when the change in topography is large?

To answer this we consider an initial value problem which is similar in concept to the laboratory experiments of Long (1954).^{††} The initial state, shown in Figure 2.6a, consists of a uniform flow with depth h_0 and velocity u_0 . At $t = 0$, an obstacle of height b_0 is quickly grown in the channel and the fluid is forced to adjust. The subsequent motion has been computed numerically using a Lax-Wendroff (1960) scheme which allows shocks to form and be maintained, insuring that mass and momentum flux are conserved across discontinuities. The numerical method is described in Appendix A.

We wish to make comparisons between the numerical solutions and the steady solutions of Figure 2.2. In the steady solutions, flow over the

[†] Chow (1959).

^{††} Houghton and Kasahara (1968) have done a similar problem.

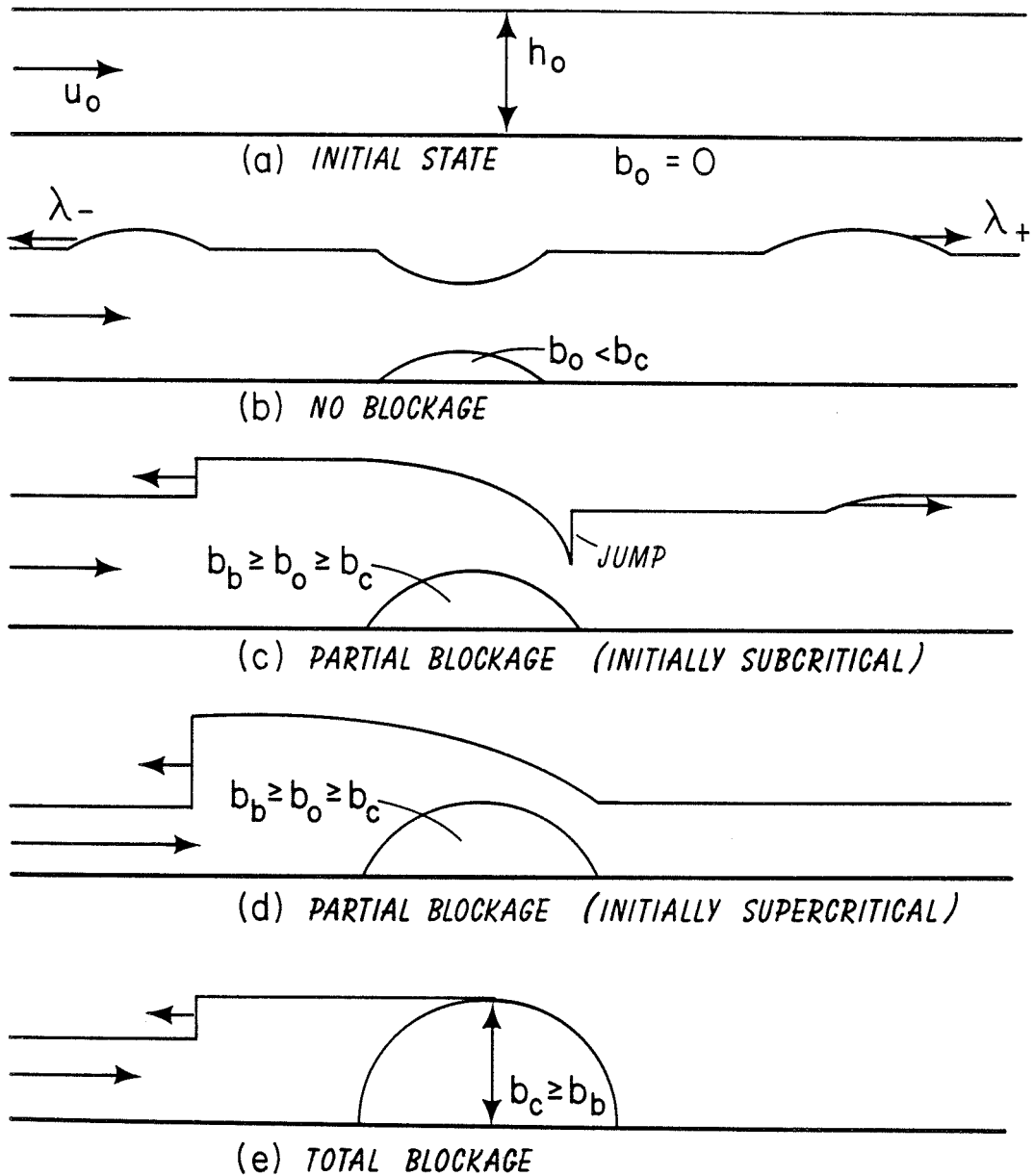


Figure 2.6

Nonrotating adjustment to an obstacle.

obstacle is possible only for $B > 2.5$. More generally, a steady solution is possible only if the flow energy is greater than some minimum value determined by the critical condition. When the flow is critical, then (2.1.5) and (2.1.8) give

$$B = b_c + \frac{Q^2}{2h^2} + h = b_c + \frac{3}{2} Q^{2/3},$$

where b_c is the sill height. Alternatively, given Q and B we can say that steady solutions are possible for obstacles having less than the critical height given by

$$b_c = B - \frac{3}{2} Q^{2/3}.$$

The adjustment depends crucially upon how high the obstacle is grown in relation to b_c . In particular, if $b_0 < b_c$ the obstacle growth results in two long gravity wave packets which move away from the obstacle, one propagating upstream and the other downstream relative to the flow (Figure 2.6b). These gravity waves leave the steady state unchanged except for a deformation in the interface over the topography. Thus, the upstream flow 'feels' the obstacle only temporarily and the asymptotic state resembles one of the supercritical or subcritical curves of Figure 2.2.

If $b_0 \geq b_c$ the adjustment is quite different. After the obstacle appears, a front is formed which moves upstream and begins to steepen (Figure 2.6c). The front eventually breaks and forms a bore which leaves behind a new steady state resembling branch ① - ⑤ of Figure 2.2. This branch is realized regardless of whether the initial flow is subcritical or supercritical; in no case is branch ② - ④ realized. The downstream state depends upon whether the initial flow is subcritical or supercritical.

In the latter case a bore and rarefaction wave form which move downstream leaving behind another supercritical state. If the flow is initially subcritical, the bore and rarefaction wave leave behind a subcritical flow with a hydraulic jump on the lee side of the obstacle (Figure 2.6c). A computer drawing showing the evolution of the bores and hydraulic jump appears in Figure 2.7.

Once the controlled configuration is realized a further increase in b_0 will cause a new bore to be generated which moves upstream and leaves behind a new controlled state. Eventually a height, b_b , will be reached at which the upstream flow is completely blocked[†] (Figure 2.6e). In this case, the Rankine-Hugoniot conditions (Equations 2.2.1 and 2.2.2), when applied to the bore, give

$$c(b_b - h_0) = -u_0 h_0$$

and

$$c(u_0 h_0) = \frac{-b_b^2}{2} + u_0^2 h_0 + \frac{h_0^2}{2}.$$

These can be combined into an equation for the blocking height in terms of the initial conditions alone:

$$\left(\frac{b_b}{h_0}\right)^3 - \left(\frac{b_b}{h_0}\right)^2 - 2(F_0^2 + \frac{1}{2}) \frac{b_b}{h_0} + 1 = 0,$$

where $F_0 = u_0/h_0^{1/2}$.

Once the controlled state is established (i.e., $b_b > b_0 > b_c$) it is interesting to observe the effect of lowering the obstacle to a new

[†] It is not possible to model complete blockage numerically as the numerical scheme will not handle zero depth.

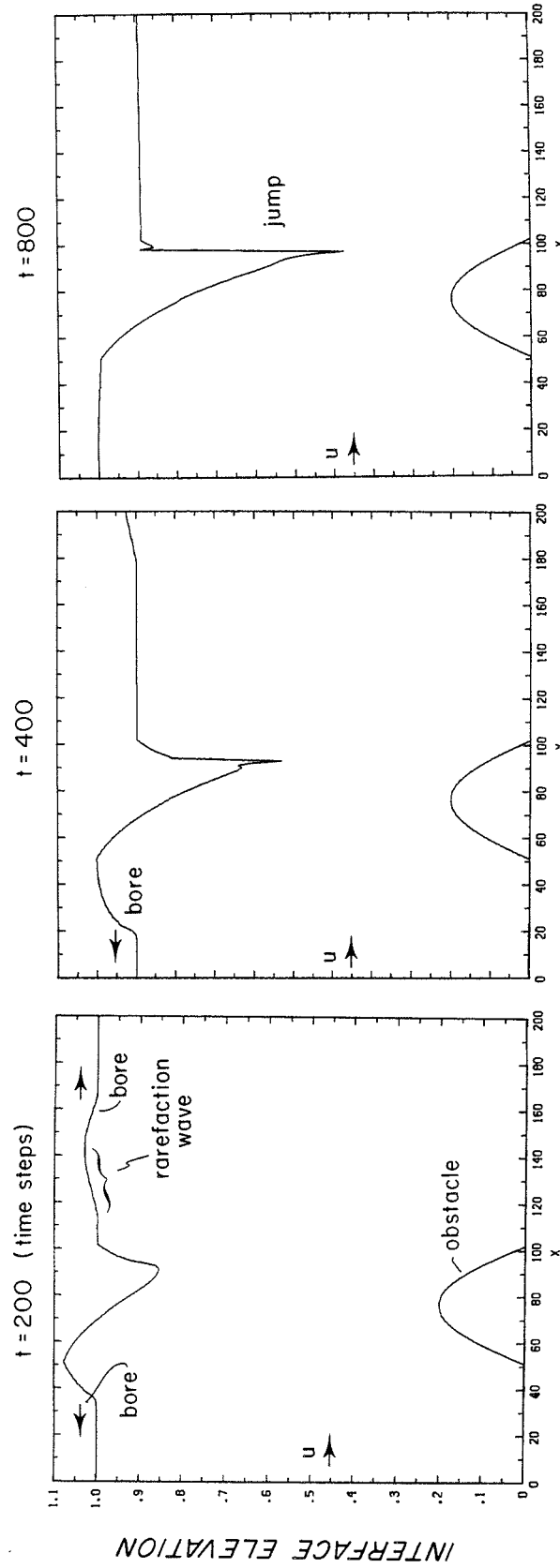


Figure 2.7

Nonrotating adjustment for $b_c < b_0 < b_b$ showing development of bores and hydraulic

jump. $Q_0 = .7$, $B_0 = 1.25$.

height, b_{00} . If the initial state was subcritical, so that a jump forms in the lee of the sill after control is established, then the flow returns to a subcritical state if $b_{00} < b_c$. In this case the jump moves upstream over the sill and 'washes' out the critical flow. However, if the initial flow was supercritical (no downstream jump exists), then the obstacle must be lowered to a new height, $b_{cc} < b_c$, for the supercritical flow to become re-established. In this case, a hysteresis occurs which tends to keep the fluid in its controlled state. The supercritical flow is re-established when the upstream propagating bore reverses its direction and moves back downstream over the obstacle. A computer drawing of these events is shown in Figure 2.8.

The height b_{cc} is the value necessary to maintain a stationary bore upstream of the obstacle and is calculated from equations (2.2.1), (2.2.2) and (2.5.1) with $c = 0$. In particular (2.5.1) gives

$$b_{cc} = B_1 - \frac{3}{2} Q_0^{2/3}$$

where $B_1 = \frac{u_1^2}{2} + h_1$ is computed from

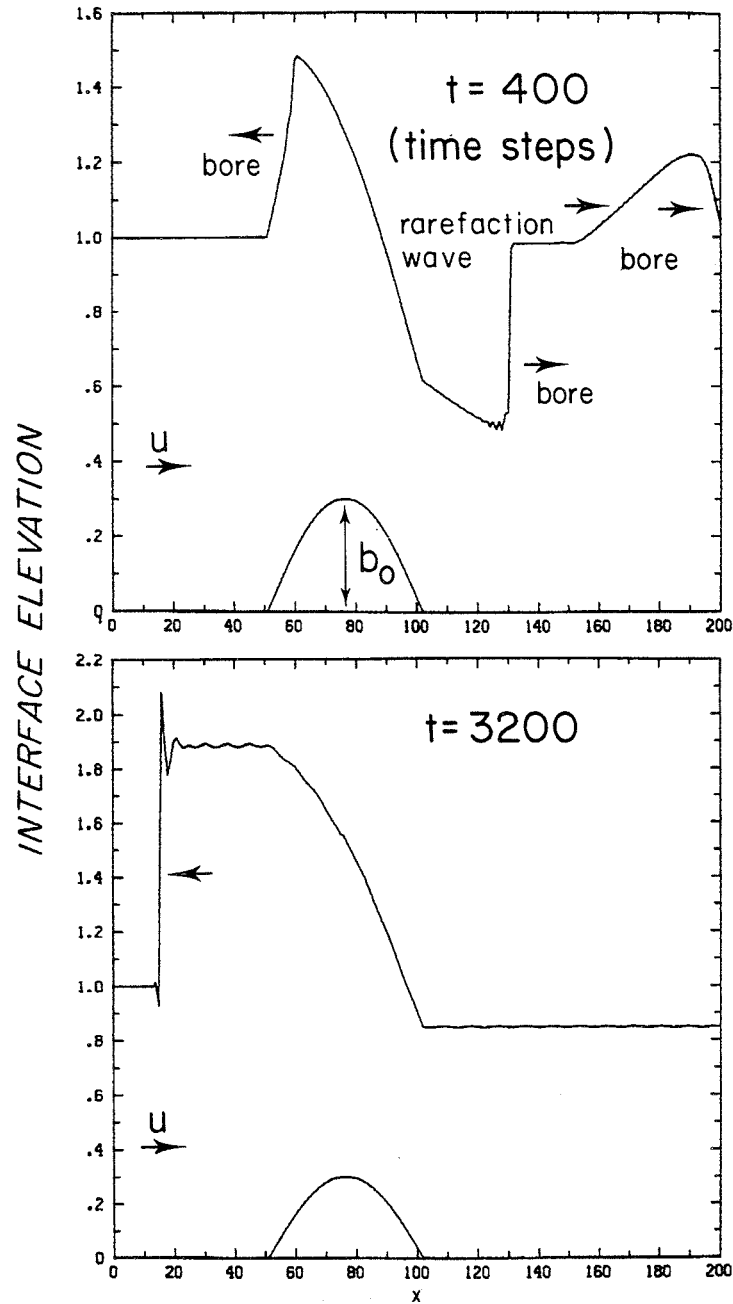
$$u_0 h_0 = u_1 h_1,$$

and

$$u_0^2 h_0 + \frac{h_0^2}{2} = u_1^2 h_1 + \frac{h_1^2}{2}.$$

These can again be combined into an expression for b_{cc} involving only the initial conditions:

$$\frac{b_{cc}}{h_0} = \frac{F_0^2 + \frac{1}{2}}{[(1 + 8F_0^2)^{1/2} - 1]} - \frac{3}{2} F_0^{2/3} + \frac{3}{8} [(1 + 8F_0^2)^{1/2} - 1]$$

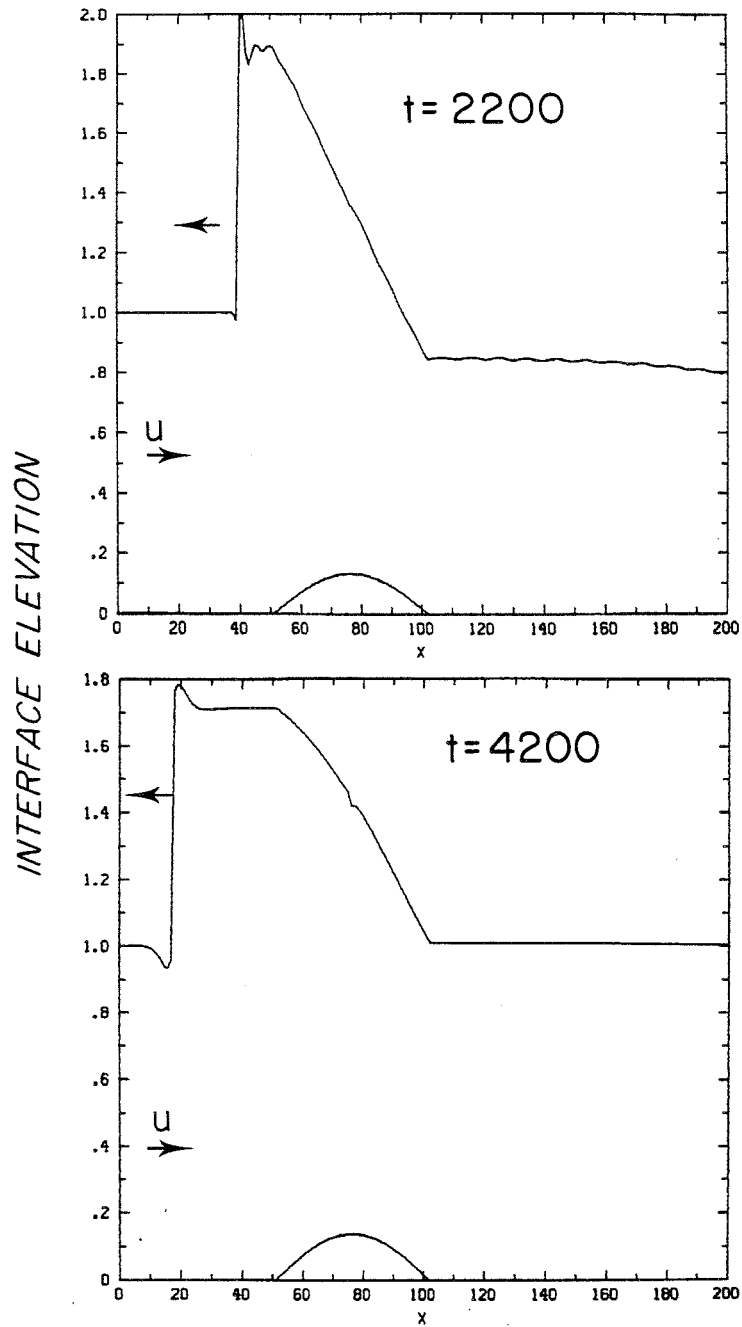


(a)
Initial
adjustment
for $b_0 >$
 b_c

(b)
 $b_0 > b_c$:
Bore moves
upstream,
establishing
controlled
flow.

Figure 2.8

Hysteresis of surface for initially supercritical flow $b_c = .160$,
 $b_{cc} = .112$.

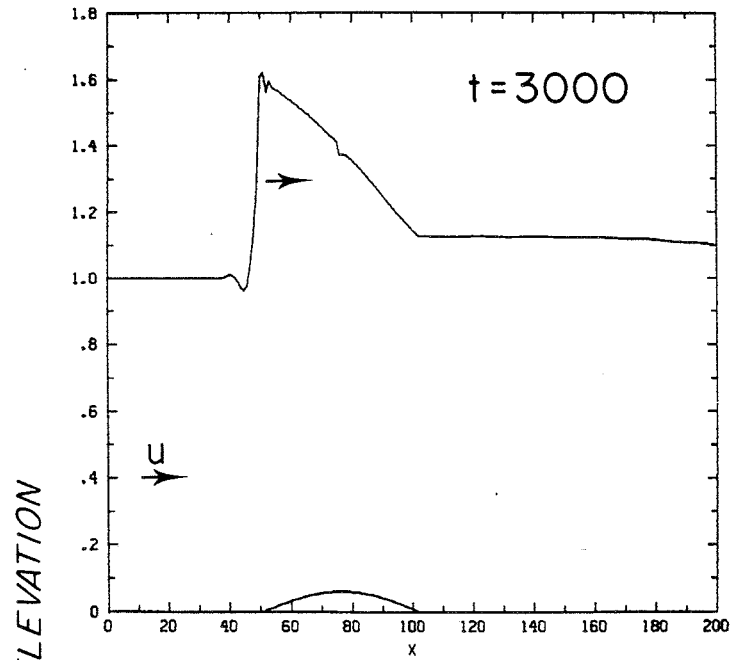


(c)

At $t = 2200$ time steps, b_0 is suddenly decreased to .135 (i.e., $b_c > b_0 > b_{cc}$).

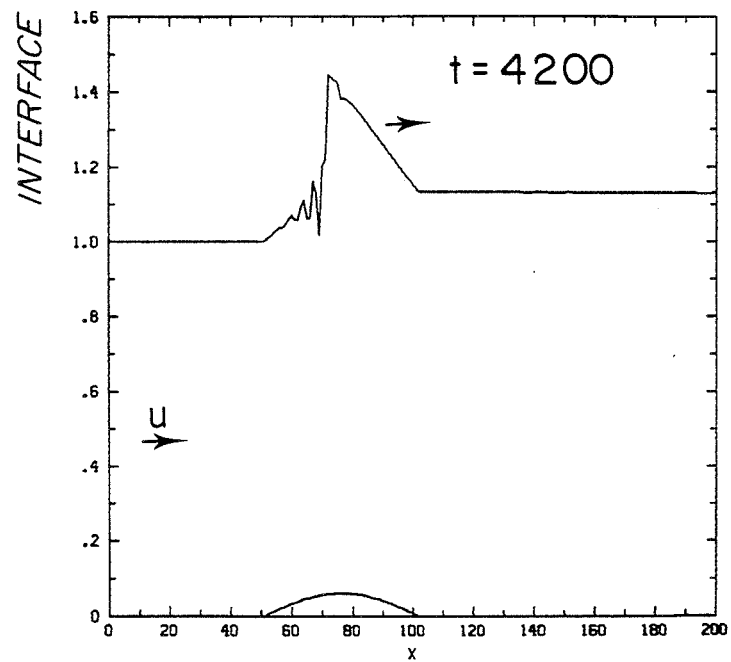
(d)

Despite the lowering of the obstacle in part (c), the bore continues to move upstream, establishing a controlled flow.



(e)

The obstacle is launched so that $b_c > b_{cc} > b_0 = .75$, causing the bore to reverse.



(f)

The bore moves backward over the obstacle, re-establishing the initial supercritical flow.

The hysteresis effect has been predicted by Baines and Davies (1980) but has not, until this point, been verified numerically or experimentally.

Figure 2.9 shows how the final steady state depends on the initial conditions of the experiment. Values of b_c , b_b and b_{cc} are plotted for various initial energies[†] with a fixed flow rate. Given Q_0 and B_0 there are two possible values of b_b , one for subcritical and the other for supercritical initial flow.

For large B_0 , the asymptotic behavior of the solutions is as follows:

$$\lim_{B_0 \rightarrow \infty} b_c = B_0 - \frac{3}{2} Q_0^{2/3}$$

$$\lim_{B_0 \rightarrow \infty} b_b = B_0 \quad (\text{initially subcritical})$$

$$\lim_{B_0 \rightarrow \infty} b_b = 2^{3/4} B_0^{1/4} Q_0^{1/2} \quad (\text{initially supercritical})$$

$$\lim_{B_0 \rightarrow \infty} b_{cc} = 2^{3/4} B_0^{1/4} Q_0^{1/2} - \frac{3}{2} Q_0^{2/3}$$

Since b_b for initially supercritical flow is only $O(B_0^{1/4})$, this curve will intersect the curve $b_c(B_0)$ at some point. Past this point the flow is completely blocked before control occurs.

[†] It is traditional to display this type of information using the initial Froude number, F_0 , rather than B_0 . However this will prove difficult later in experiments with rotating flows. We therefore use the initial parameters B_0 and Q_0 which prove to be convenient in later results.

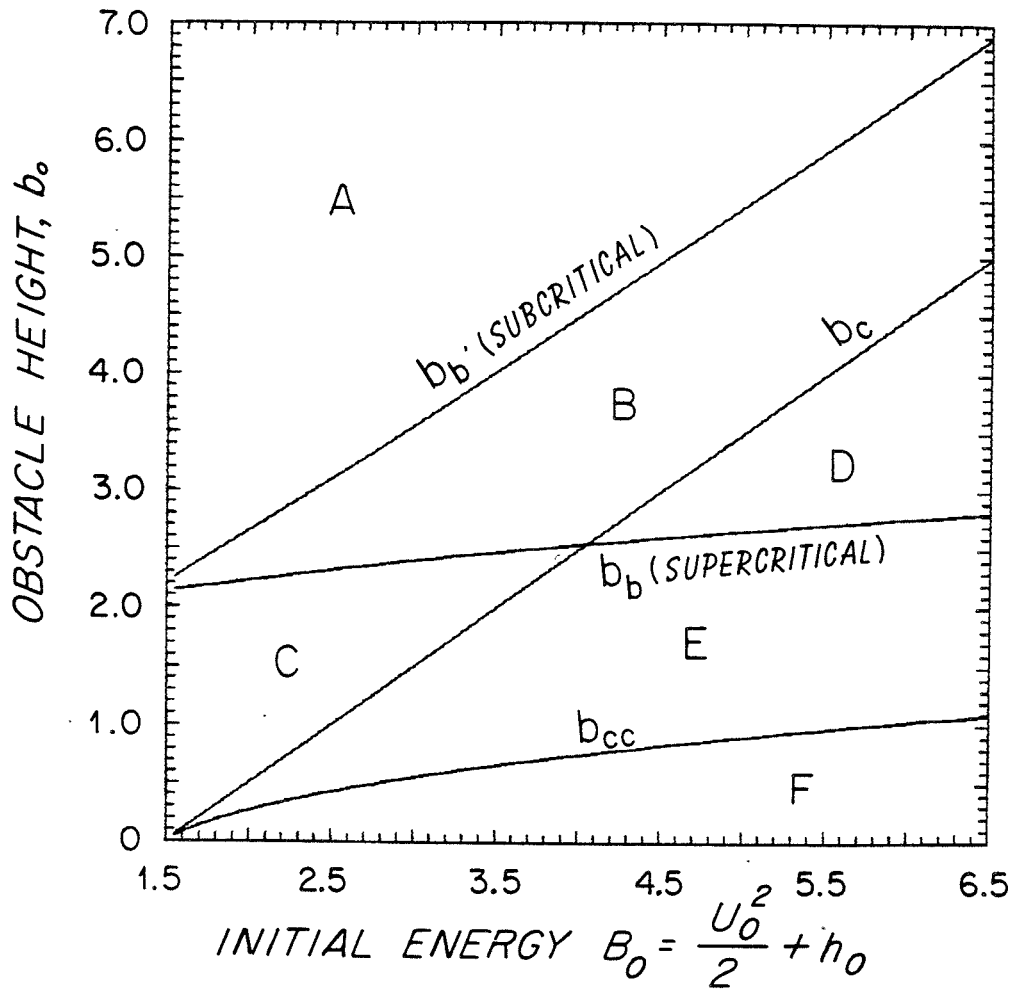


Figure 2.9
Asymptotic states for various initial energies with $Q_0 = 1$.

Key

A - all flows blocked
 B - initially supercritical flow is blocked
 C - all flows controlled

P - initially supercritical flow is blocked, initially subcritical remains subcritical
 E - initially supercritical flow is subject to hysteresis, initially subcritical remains subcritical
 F - initial flow is unchanged

2.6 Unsteady Flow

The discussion of steady flow has centered around the role of the obstacle height in the establishment of upstream influence. Now consider an unsteady stream which passes over an obstacle and oscillates with time but does not reverse the flow (i.e. u is always > 0). This is typically the case in many deep oceanic straits (see Figure 1.2, for example). How important is the height of the obstacle in determining the far field flow? Since analytic solutions for nonlinear unsteady flow over topography are generally unavailable it becomes difficult to make interpretations using bifurcations and branches. The characteristic formulation used earlier, however, still provides an intuitive tool in evaluating the role of the obstacle height.

Consider the wave-like flow shown in Figure 2.11. The flow is set up (numerically) by oscillating the depth of an initially steady, controlled flow periodically at a point upstream of the obstacle. The oscillatory forcing results in a train of waves which propagate downstream and are partially transmitted across the obstacle. The waves can be considered 'large' in the sense that their amplitude and length are of the same scale as the obstacle. After the passage of several waves the flow field over the obstacle became nearly periodic and the characteristics (Figure 2.10) take on a wavy appearance while retaining the same general geometry as the ones in Figure 2.3a. Conditions at the sill alternate from a subcritical ($\lambda_- < 0$) to supercritical ($\lambda_+ < 0$) in a periodic fashion. Upstream of the obstacle the unsteady flow is subcritical at all times, while a region in which the flow is always supercritical exists between the sill and hydraulic jump.

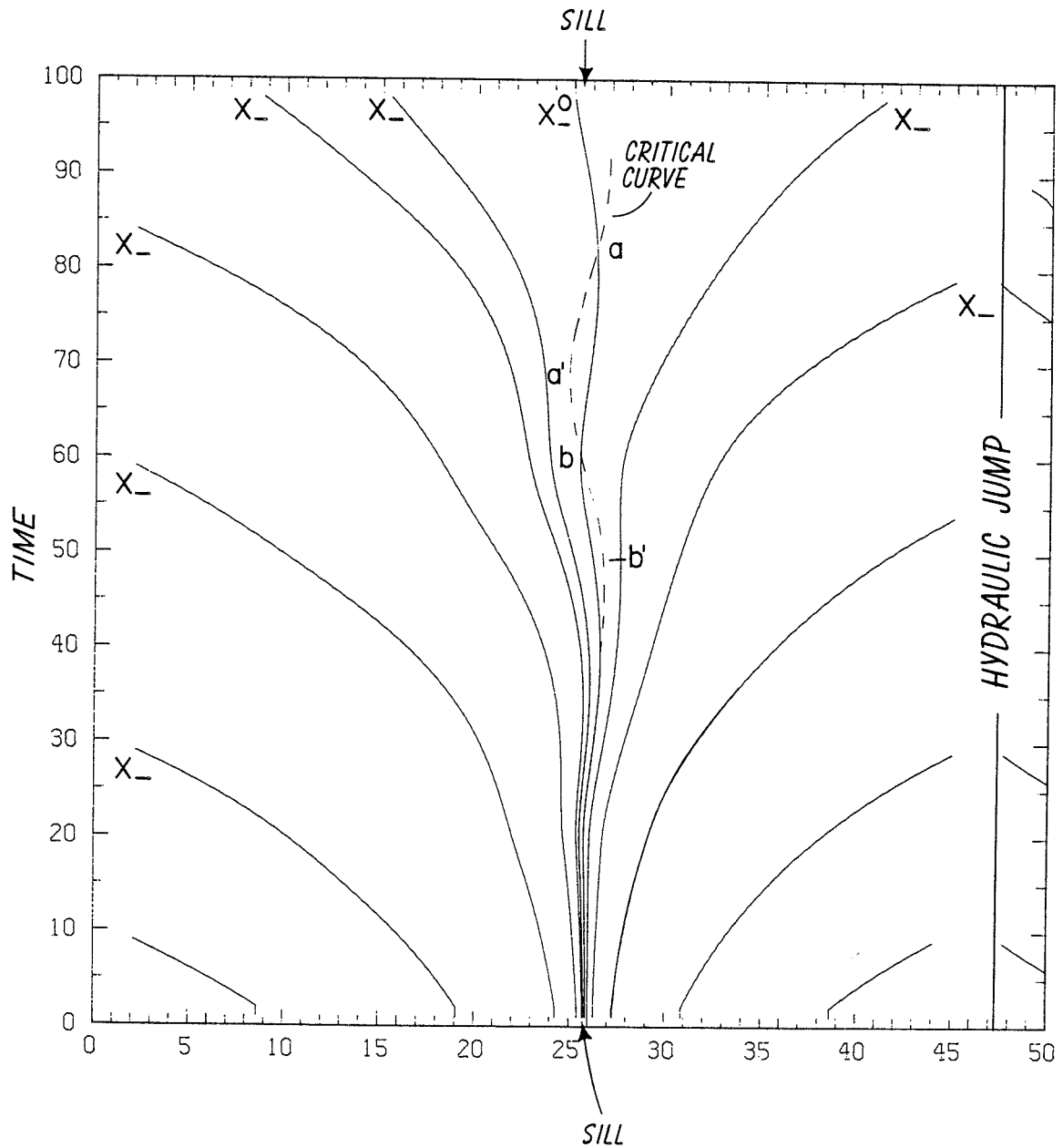


Figure 2.10

X_- characteristic curves for unsteady flow over an obstacle. The dotted line traces the path of critical flow. The sill lies at $x = 25.5$.

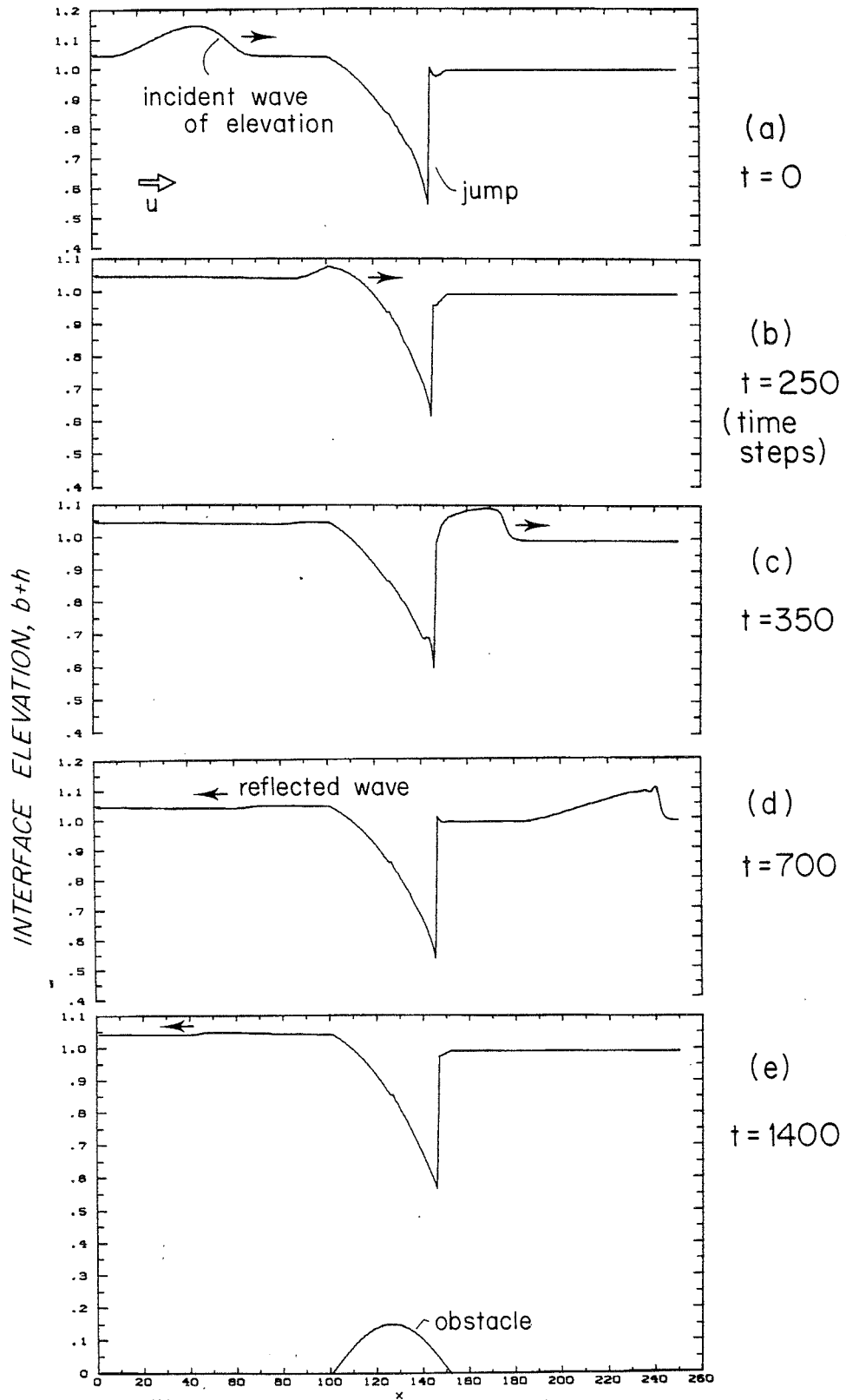
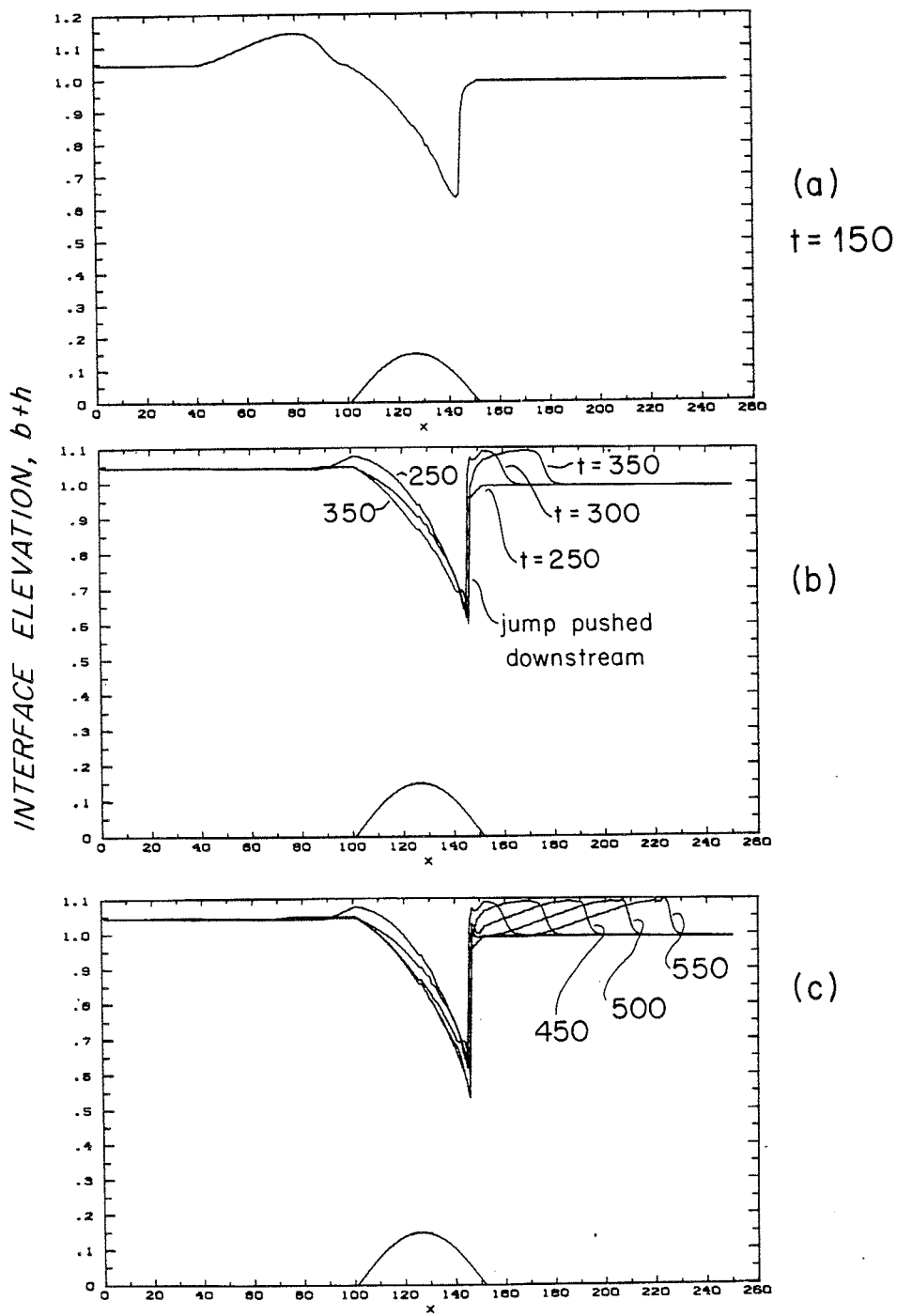


Figure 2.11

Establishment of oscillatory flow by periodic upstream forcing.



Superposition of surface profiles showing wave passing obstacle.

In the steady, controlled flow of Figure 2.3c, far field conditions can be traced back to the sill through integration of (2.3.5) along x_- characteristics. In Figure 2.10 the x_- characteristics diverge from a dividing characteristic (marked x_-^0) rather than from the sill. Such a characteristic must exist by virtue of the fact that the sill is bordered upstream by a region of subcritical flow and downstream by a region of supercritical flow.

Suppose that the obstacle height is suddenly increased by a small amount. What is the far field effect? We first note that if \bar{R}_\pm are taken to represent the unperturbed unsteady fields and $\bar{R}_\pm + r_\pm$ the perturbed unsteady fields, then $r_{p\pm}$ measures the response at point P to the change in height, as in Section 2.3. In particular, if P lies away from the obstacle then the arguments leading to (2.3.9a) continue to hold and

$$r_{p-} = \int_Q^P \frac{db}{dx} dt - \int_Q^P \frac{db'}{dx} dt' . \quad (2.6.1)$$

The integration path is now a characteristic which extends from P to a point Q lying on x_-^0 at the initial instant. The value of r_{p-} depends in a complicated way on the new topography, $b'(x)$, as well as the integration paths.

Equation (2.6.1) links the far field to the dividing characteristic. How is the dividing characteristic related to the geometry of the obstacle? Suppose that the flow is periodic with longest period τ , so that $R_\pm(x,t) = R_\pm(x,t + \tau)$. Integration of (2.3.5) along the dividing characteristic over one period then yields

$$R_-(x, t + \tau) - R_-(x, t) = - \int_t^{t+\tau} \frac{db}{dx} dt = 0$$

Thus, the dividing characteristic must spend an equal time on either side of the sill as weighed by the bottom slope; if the slope is steeper on one side the curve must hug the sill more closely on that side or spend less time there.

How far from the sill can the dividing characteristic stray? In Figure 2.10 the downstream and upstream extremities of the dividing characteristic are labeled a and b respectively. Since the flow is critical at a and b (x_0^0 is vertical there) the dividing characteristic must occur within the envelope of the curve along which the flow is critical (shown as a dotted line in Figure 2.10). Although the critical curve is of less dynamical significance in the unsteady case, its geometry gives information concerning the confines of the dividing curve. At a', where the upstream excursion of the critical curve is maximum, $c^- = \partial c^- / \partial t = 0$ so that

$$\frac{-d_- R_-}{dt} = \frac{-\partial R_-}{\partial t} = \frac{\partial h^{1/2}}{\partial t} - \frac{\partial c_-}{\partial t} = \frac{\partial h^{1/2}}{\partial t} = \frac{db}{dx} > 0 \quad (2.6.2)$$

Thus the depth increases with time at a' (and decreases at b'). Equation (2.6.2) also indicates that obstacles with sharp crests will tend to confine the critical point more so than obstacles with rounded crests. Furthermore, as the height of the forced wave grows larger the excursion of the critical point only increases as the square root of this height, assuming that changes in the shape of the wave can be neglected.

If the flow is initially subcritical, the periodic state set up has wavy characteristics which are similar in appearance to those of

Figure 2.3a. Despite this, upstream influence can be exerted by the topography, as a reexamination of Equation (2.3.8) will show. Again we consider the influence r'_- at a point P upstream of the obstacle long after the adjustment has occurred and a new unsteady state established. The response depends on the initial conditions as well as an integration along an x_- characteristic from P to a point Q' downstream of the obstacle. Unlike the steady case, however, it is no longer true that $R_Q = R_{Q'}$. Nor is λ_- a function of db/dx alone, and the symmetry property that caused the steady integral to vanish no longer holds. Therefore, upstream influence may be present in the unsteady subcritical case for obstacles of any height because of the wave response to topography.

At this point the meaning of the term 'hydraulic control', as applied to unsteady flows, should be clarified. Traditionally a flow is said to be controlled if far field influence is exercised by some discrete topographic point. This is a meaningful concept when applied in steady situations but becomes vague in the unsteady case due to the fact that influence is exerted by a continuous distribution of points. We therefore reserve the use of the term 'control' for steady situations.

This is not to say that upstream conditions in the flow of Figure 2.7 are equally sensitive to changes in the sill elevation as to elevation changes elsewhere. We have seen that all x_- characteristics originate from a dividing characteristic that is tied to the sill through Equation (2.6.2). Figure 2.12 shows the result of a numerical experiment in which an obstacle is grown in a periodic flow over an initially flat bottom.

The time-average upstream height (measured after the adjustment occurs) is plotted for various obstacle heights. The result is compared to the result of doing the same experiment using an initially steady flow whose velocity and depth equal that of the time-average initial periodic flow. In both cases there is little or no upstream influence until the critical obstacle height for the steady flow, b_c , is reached. However, when $b_0 > b_c$ a dividing characteristic appears in the forced flow and this is followed by a change in the mean upstream height.

2.7 Disruption of Control

The characteristics of Figure 3.10, although wavelike, are similar to those of a steady controlled flow, with a dividing characteristic playing the same role that the critical characteristic does in Figure 2.3c. Suppose now that the oscillations become larger in relation to the mean fields. Will the dividing characteristic remain, or will some new characteristic regime be established? As long as subcritical flow is maintained upstream and supercritical flow downstream of the sill, a dividing characteristic will continue to exist. Therefore some change in these conditions is necessary in order that the dividing characteristic be swept away.

The dividing characteristic might be swept away if the incident waves contained regions of supercritical flow. However, such waves would rapidly break and the situation would probably not be typical of deep strait and sill dynamics. However, if a hydraulic jump exists in the lee of the obstacle, then the incident wave may be able to cause the jump to

move upstream across the sill and establish subcritical flow everywhere. In this case the dividing characteristic would be swept away.

Consider the flow shown in Figure 2.13b. Over the obstacle the fields are steady and controlled and a hydraulic jump exists in the lee of the sill. Upstream, an isolated wave approaches. This wave collides with the obstacle and displaces the hydraulic jump. If the jump is displaced upstream past the sill, creating a flow that is everywhere subcritical, then we say that control has been disrupted. Numerical results which show the amplitude of the incident waves required to disrupt control will be discussed presently, but we first try to develop some intuition into the effects of waves on jumps.

Consider a jump which lies at position $\eta(t)$ in a flow over a flat bottom. The position is determined by the Rankine-Hugoniot conditions (2.2.1) and (2.2.2) with $c = \frac{d\eta}{dt}$:

$$\frac{d\eta}{dt} (h_1 - h_0) = (u_1 h_1 - u_0 h_0) \quad (2.7.1)$$

and

$$\frac{d\eta}{dt} (u_1 h_1 - u_0 h_0) = u_1^2 h_1 + \frac{h_1^2}{2} - u_0^2 h_0 - \frac{h_0^2}{2}, \quad (2.7.2)$$

where h_0 and h_1 are the depths immediately upstream and downstream.

If the jump is stationary then

$$u_1 h_1 = u_0 h_0 \quad (2.7.3)$$

and

$$u_1^2 h_1 + \frac{h_1^2}{2} = u_0^2 h_0 + \frac{h_0^2}{2}. \quad (2.7.4)$$

It can be shown from these that

$$h_1/h_0 = \frac{1}{2} [(1 + 8F_1^2)^{1/2} - 1] = (F_1^2 + \frac{1}{2}) / (F_2^2 + \frac{1}{2}).$$

Thus $h_1/h_0 > 1$ implies that the upstream flow is supercritical and downstream flow is subcritical.

Suppose that a train of small amplitude waves now passes through the jump. The linearized flow fields become

$$\left. \begin{aligned} u &= u_0 + \text{Re} [A_0 e^{ik_0(x - c_0 t)}] \\ h &= h_0 + \text{Re} \left[\frac{A_0}{h_0^{1/2}} e^{ik_0(x - c_0 t)} \right] \end{aligned} \right\} x \leq \eta$$

and

$$\left. \begin{aligned} u &= u_1 + \text{Re} [A_1 e^{ik_1(x - c_1 t)}] \\ h &= h_1 + \text{Re} \left[\frac{A_1}{h_1^{1/2}} e^{ik_1(x - c_1 t)} \right] \end{aligned} \right\} x \geq \eta$$

(No reflected waves are allowed by the supercritical upstream flow.)

We also expand the jump position in powers of the amplitude A_1 , say:

$$\eta = \eta^{(0)} + A_1 \eta^{(1)} + \dots \quad (2.7.4)$$

Equations (2.7.1) and (2.7.2) are now applied at $x = \eta$. Since the first order fields satisfy (2.7.2) and (2.7.3) $\eta^{(0)} = 0$. To next order, we find

$$\begin{aligned} k_1 c_1 &= c_0 k_0 = \omega, \\ A_0 \eta^{(1)} (h_0 - h_1) &= (c_0 A_0 - c_1 A_1) e^{-i\omega t}, \end{aligned} \quad (2.7.5)$$

and

$$\left[2u_0 h_0 \left(\frac{A_0}{h_0^{1/2}} - \frac{A_1}{h_1^{1/2}} \right) + (u_0^2 + h_0) A_0 - (u_1^2 + h_1) A_1 \right] e^{-i\omega t} = 0.$$

From the latter, we find

$$\begin{aligned} (u_0^2 + 2u_0h_0^{1/2} + h_0)A_0 &= (u_1^2 + 2u_0 \frac{h_0}{h_1^{1/2}} + h_1)A_1 \\ &= (u_1^2 + 2u_1h_1^{1/2} + h_1)A_1 \end{aligned}$$

in view of (2.7.3). Therefore,

$$\frac{A_1}{A_0} = \frac{c_0^2}{c_1^2} \quad (6.7.6)$$

Combining (2.7.4), (2.7.5) and (2.7.6) gives the jump position

$$\eta = \frac{A_0(1 - \frac{c_0}{c_1})}{k_0(h_0 - h_1)} \sin(\omega t) + O(A_1^2)$$

Recalling that the upstream depth near the jump is $h = h_0 + A_0 \cos \omega t$, we see that the wave crests tend to push the jump downstream while the troughs tend to pull it back upstream. It is also evident that the maximum excursion of the jump is proportional to the length of the incident wave. Based on these results we expect low frequency waves of depression ($h' < 0$) be more effective in disrupting control.

If the incident wave approaches from downstream then the same analysis can be carried out with

$$\left. \begin{aligned} u &= u_0 \\ h &= h_0 \end{aligned} \right\} \quad x < \eta$$

and

$$\left. \begin{aligned} u &= u_1 + \text{Re} [A_I e^{ik_I(x - c_I t)} + A_R e^{ik_R(x - c_R t)}] \\ h &= h_1 + \frac{\text{Re}}{h_1^{1/2}} [-A_I e^{ik_I(x - c_I t)} + A_R e^{ik_R(x - c_R t)}] \end{aligned} \right\} \quad x > \eta$$

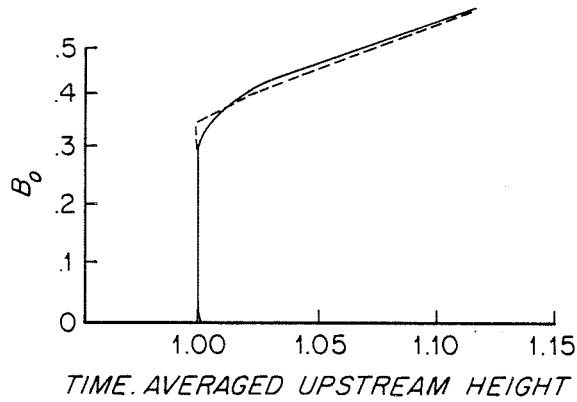
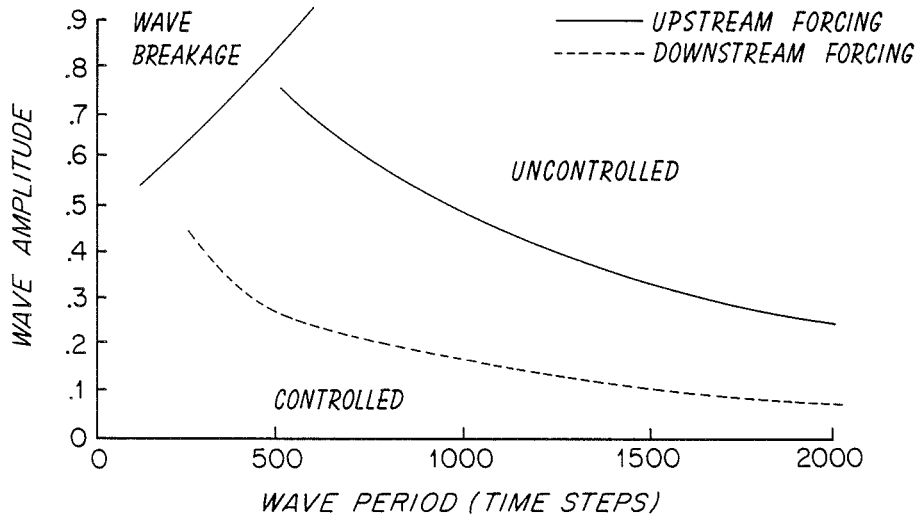


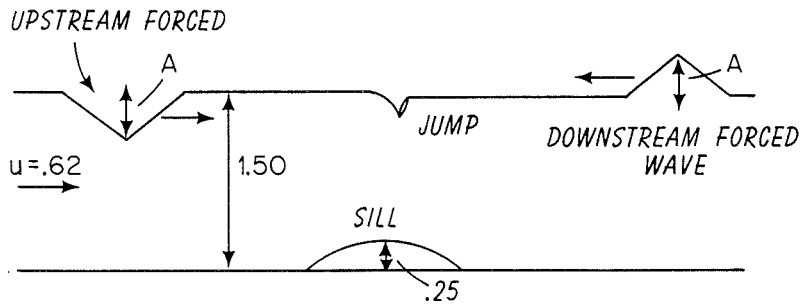
Figure 2.12

Upstream response to a slowly growing obstacle in periodic (—) and steady (---) flow. The forced wave amplitude/upstream depth for the periodic flow is .2.



(a)

Wave amplitude required to disrupt control.



(b)

Numerical experiment showing forced waves.

Figure 2.13

In this case we find

$$\omega = c_I k_I = c_R k_R ,$$

$$\frac{A_R}{A_I} = - \frac{c_I^2}{c_R^2} ,$$

and

$$\eta = \frac{A_I \left(1 - \frac{c_I}{c_R}\right)}{k_I (h_1 - h_0)} \sin(\omega t) + O(A_I^2)$$

Since $k_I < 0$ and $c_I < 0$ for the subcritical downstream flow, the amplitude of η is also negative. This implies that the crests of the waves push the jump upstream while the troughs pull it downstream.

The conclusion is that, for upstream forcing, a wave of depression ($h' < 0$) is needed to disrupt control. For downstream forcing, a wave of elevation ($h' > 0$) is required.

The results of the numerical experiment are summarized in Figure 2.9a in terms of the forced wave amplitude and period needed to disrupt control. Results are considered only for the cases in which the incident waves do not break. The figure bears out our earlier predictions that lower frequency forcing is the most effective in destroying control. We further note that the amplitudes required for disruption are the same order as the upstream depth, despite the fact that the basic flow was established using an obstacle with height only slightly greater than b_c .

2.8 Semi-Steady Flow

In connection with problems involving upstream forcing, questions also arise concerning the local behavior of the waves near the obstacle.

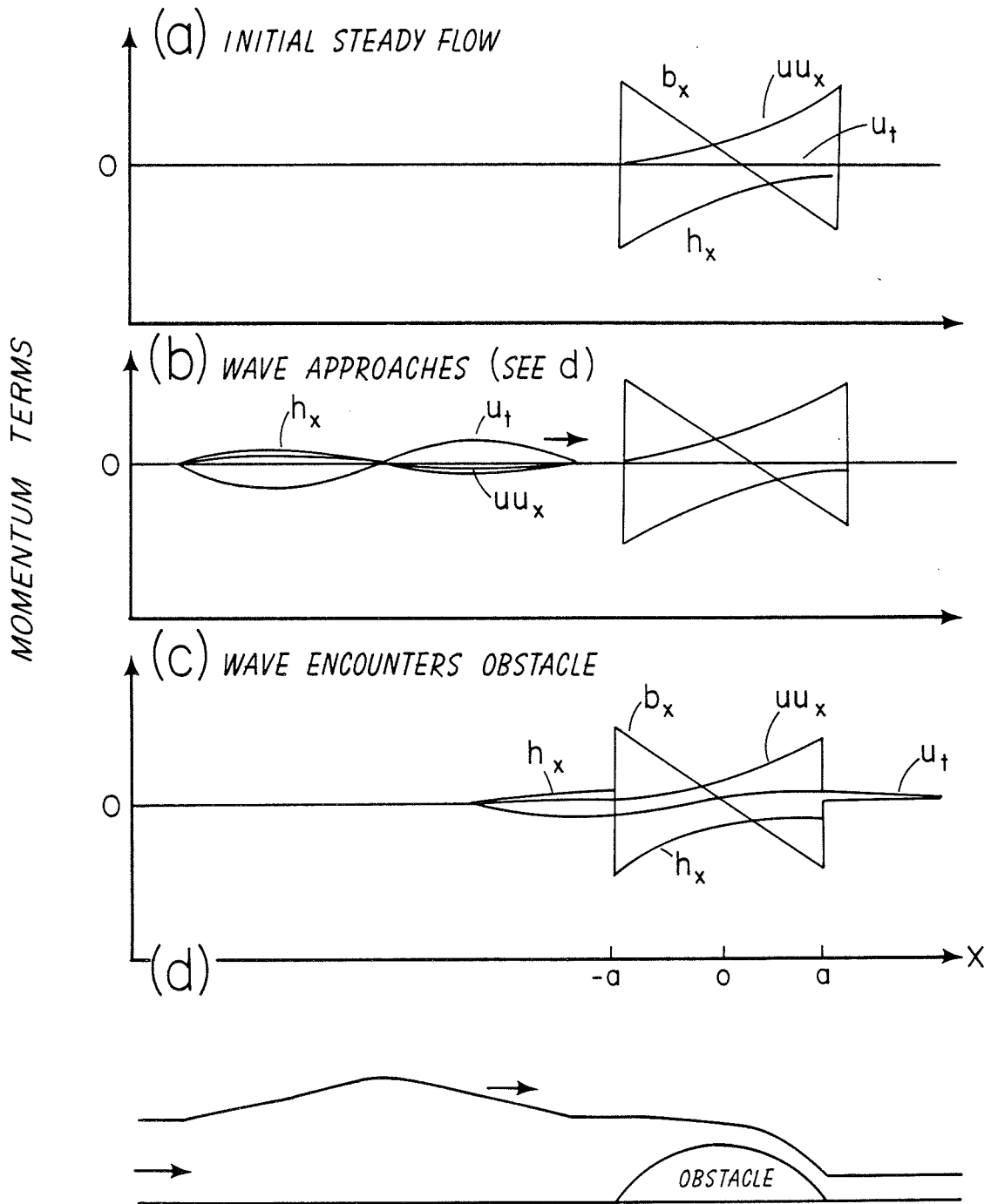


Figure 2.14

Dynamic balance for wave in mean flow passing obstacle.

For example, how much wave energy is reflected back upstream and how much is actually transmitted across the sill? Although it is difficult to describe the unsteady fields over the obstacle analytically, it is often possible to approximate the far field transient motion. This is made possible by the strong dynamic balance that is induced by the obstacle. Consider, for example, the momentum balance for the flow shown in Figure 2.14a. Away from the obstacle the balance is 'weak' in the sense that all momentum terms vanish identically. Over the obstacle, however, each term is finite.

Suppose now that a transient is generated upstream (Figure 2.14b). The dynamic balance within the wave is completely unsteady in the sense that $\partial/\partial t \approx \partial/\partial x$. Over the obstacle, however, the wave loses its identity as the unsteady terms are dwarfed by the advective and surface slope terms (Figure 2.14c).

The above remarks can be formalized by considering the two length scales of the problem. The first is the scale of the topography, $2a$, while the second is the scale of the wave,

$$L = T/C_+^0,$$

where C_+^0 is the characteristic speed scale of the upstream flow and T is the period of the upstream forcing. If we let $\epsilon = 2a/L$, then the fields can be written in the form

$$\begin{aligned} h &= h(\epsilon t, \epsilon x) & |x| > a & \quad (2.8.1) \\ h &= h(\epsilon t, x, \epsilon x) & |x| < a & \end{aligned}$$

If $\epsilon \ll 1$, the lowest order fields will be unsteady away from the obstacle but steady over the obstacle. At $x = a$ the fields must be matched according to equation (2.5.1):

$$B(\epsilon t) - \frac{3}{2} Q^{2/3}(\epsilon t) = b_c \quad (2.8.2)$$

where

$$B(\epsilon t) = \left(\frac{u^2(\epsilon t, \epsilon x)}{2} \right) + h(\epsilon t, \epsilon x) \quad |x| = a$$

$$Q(\epsilon t) = u(\epsilon t, \epsilon x) \quad h(\epsilon t, \epsilon x) \quad |x| = a$$

One matter which can be investigated conveniently using the semi-steady approximation concerns the affect of the obstacle on waves. Suppose a train of small amplitude waves of length $2\pi/k_I \gg L$ and frequency ω_I is generated upstream of the obstacle. A reflected wave of length $2\pi/k_R$ and frequency ω_R is produced as the incident waves encounter the topography. The linearized upstream fields are then

$$u = U + u' = U + A_I e^{ik_I(x - c_I t)} + A_R e^{ik_R(x - c_R t)}$$

$$h = H + h' = H + H^{1/2} [A_I e^{ik_I(x - c_I t)} - A_R e^{ik_R(x - c_R t)}]$$

where U and H are the unperturbed upstream fields while

$$c_I = U + H^{1/2},$$

$$\text{and } c_R = U - H^{1/2}.$$

Substituting U and H into (2.8.2) gives, to lowest order,

$$\frac{U^2}{2} + H - \frac{3}{2} (UH)^{2/3} = b_c$$

or

$$\frac{F_d^2}{2} - \frac{3}{2} F_d^{2/3} + 1 = \frac{bc}{H}, \quad (2.8.3)$$

where $F_d = U/H^{1/2}$ is the Froude number of the upstream flow.

To second order we find

$$u'U + h' = (UH)^{-1/3} (u'H + h'U).$$

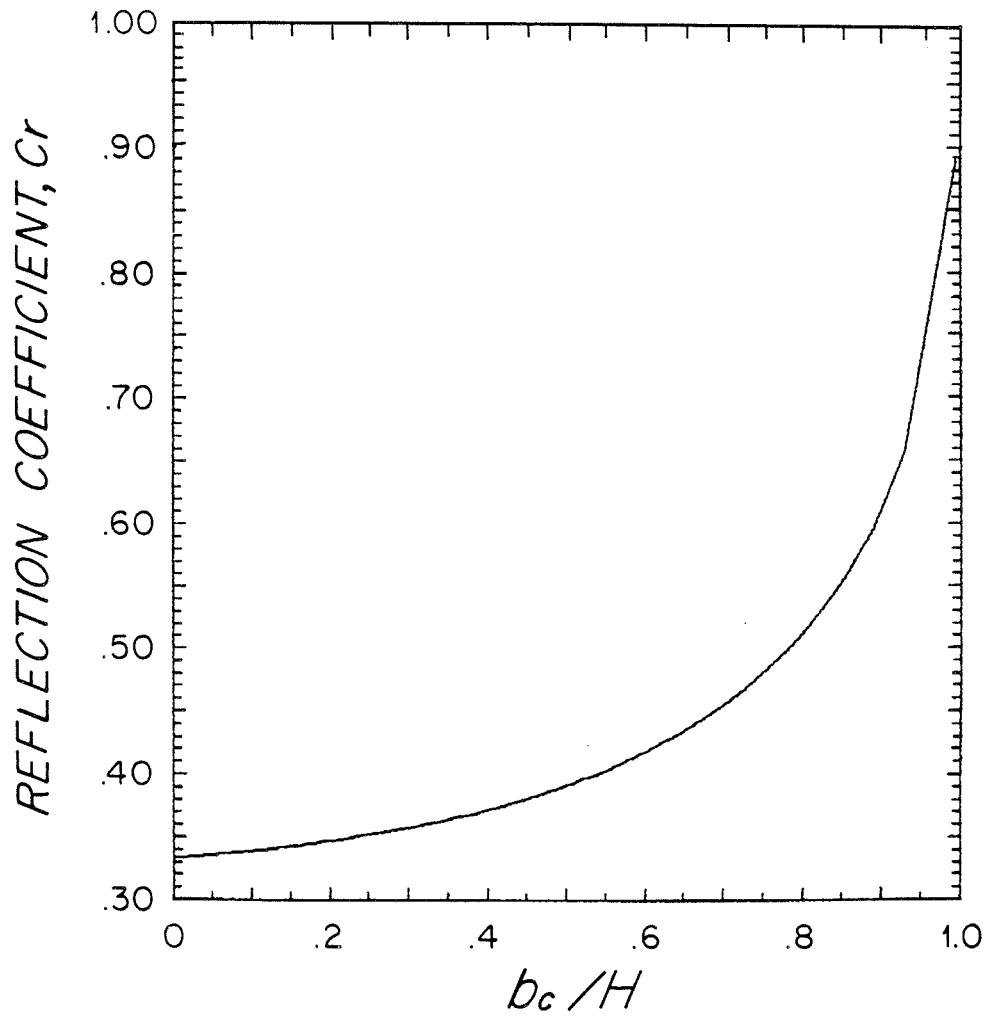


Figure 2.15

Reflection coefficient for semi-steady wave in nonrotating flow.

Substituting the expressions for u' and h' and evaluating at $x = -a$ gives

$$\frac{k_I}{k_R} = \frac{c_R}{c_I}$$

and

$$[(UH)^{1/3} U - H](A_I + A_R) = [U - (UH)^{1/3}] H^{1/2}(A_I - A_R) .$$

The reflection coefficient is then

$$C_R = \frac{A_R}{A_I} = \frac{F_d^{4/3} - 1 + F_d^{1/3} - F_d}{F_d^{4/3} - 1 - F_d^{1/3} + F_d} . \quad (2.8.4)$$

Figure 2.15 contains a plot of c_R vs. b_c/H based on Equations (2.8.3) and (2.8.4). For values of b_c/H close to unity the upstream Froude number is tiny and fluid barely trickles over the sill. In this case all wave energy is reflected. For small b_c/H , the flow is nearly critical and both the numerator and denominator in (2.8.4) vanish.

Applying L'Hopitals rule gives

$$\lim_{F \rightarrow 1} C_r = \frac{4/3 F_d^{1/3+} + 1/3 F^{-2/3-1}}{4/3 F_d^{1/3-} - 1/3 F_d^{-2/3+} 1} \doteq .333 \dots$$

Thus, a substantial amount of the incident wave energy is reflected even when the obstacle is vanishingly small.⁺

2.9 Summary

Before proceeding to rotating hydraulics, we pause to summarize some of the ideas that have emerged from the discussion of one-dimensional,

⁺ However (2.8.1) becomes invalid for $0(b_c/2a) \leq \epsilon$.

time-dependent adjustment. The characteristic description of this process paints an intuitive and unifying picture of hydraulic control, and provides a tool for understanding the hydraulics of more complicated systems.

One idea central to the adjustment process is the notion of upstream influence. In a stable, steady flow, upstream influence and criticality are intimately related by the fact that all upstream points communicate directly with the critical point through connecting characteristics. It has further been shown that criticality is possible only for obstacles with a minimum height determined through energy considerations.

The unsteady case is somewhat different, as upstream influence is possible for obstacles of all heights. However, this influence is more pronounced if a dividing characteristic exists over the topography since the far field again communicates directly with the dividing characteristic. Although this curve no longer lies at the sill, it must oscillate about the sill. Thus the upstream fields are tied to the sill in a time average sense. The critical point is no longer dynamically important but does give information concerning the geometry of the dividing curve.

The final idea that deserves mention is the relative stability of the steady controlled state to time-dependent disturbances. This property is implied by the diverging pattern of x_* characteristics (Figure 2.3c) along which disturbances are spread (rather than focused). It is also present in the hysteresis effect (section 2.5) which tends to maintain the controlled state. Finally, the stability is enhanced by the sheltering effect of the obstacle as manifested in the strong dynamic balance and the ability to reflect appreciable ($c_r \geq .33$) amounts of energy upstream.

Chapter 3 Semigeostrophic Flow

In this and the following chapter we explore some extensions of the ideas developed in Chapter 2 to rotating channel flows. It will be natural to divide the discussion into two parts; the first dealing with a nondispersive system in which only Kelvin waves are present, the second with a system containing both Kelvin and Poincaré waves. The nondispersive case is treated here while the dispersive problem is left for Chapter 4.

3.1 The Model

As described earlier, the geometry to be considered is that of a strait or channel with rectangular cross section (Figure 3.1). The bottom elevation b and width w are functions of x , the downstream direction. We will be interested in a single layer of fluid which flows beneath a deep inactive upper layer.

As described in Section 2.1, the dimensionless shallow-water equations governing the lower layer are

$$u_t + uu_x + vu_y - Fv = -h_x - \frac{db}{dx} \quad (3.1.1)$$

$$\delta^2 (v_t + uv_x + vv_y) + Fu = -h_y \quad (3.1.2)$$

$$h_t + (uh)_x + (vh)_y = 0 \quad (3.1.3)$$

where

$$\delta = W/L \quad (\text{horizontal aspect ratio})$$

$$F = Wf/(gD)^{1/2} \quad (\text{width scale/Rossby radius of deformation})$$

Here U and V are velocity scales and L , W , D length scales for the lower layer. We will assume that the channel width scale is equal to

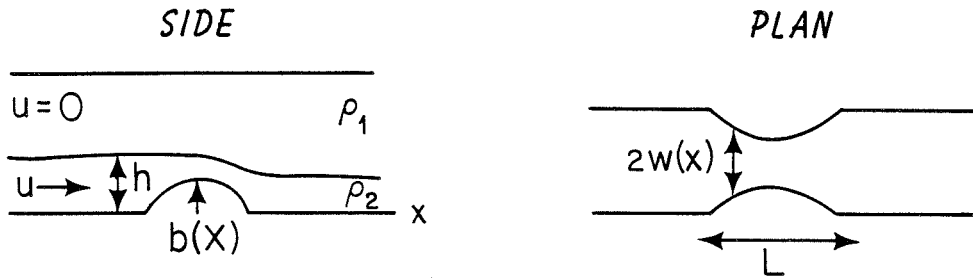


Figure 3.1
Definition sketch showing channel.

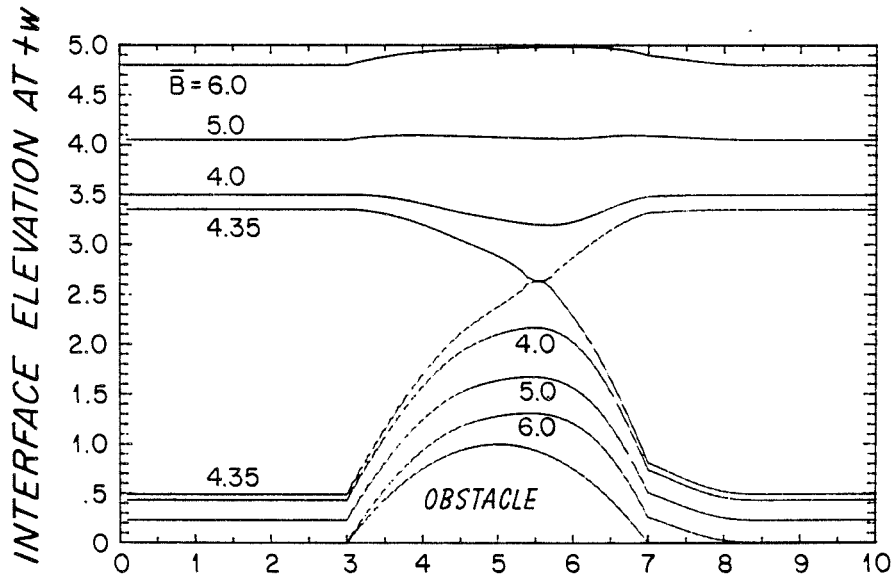


Figure 3.2

Steady semigeostrophic solutions for channel with obstacle followed by side contraction. $Q = 1, \phi = 1, b_0 = 1.$

the deformation radius so that $F = 1$. The scaling $U = (gD)^{1/2}$, which has already been introduced (see Section 2.1), together with the assumption $F = 1$ implies that the Rossby number $R_0 = U/fW$ of the flow is $O(1)$. Based on observations (e.g., Worthington (1969); Stalcup, et al. (1975)) of deep oceanic overflows, we estimate that $R_0 = O(1)$ is indeed typical. Since nonlinearity was essential to control of the more classical flow discussed earlier one might anticipate that the scaling $R_0 = O(1)$ is essential in obtaining controlled solutions to the present problem.

3.2 The Semigeostrophic Limit

Many of the deep passages in the ocean are characterized by small aspect ratios, $\delta \ll 1$, one example being the Ecuador Trench. In this case equations (3.1.1-3) become 'semigeostrophic':

$$u_t + uu_x + vu_y - v = -h_x - \frac{db}{dx}, \quad (3.2.1)$$

$$u = -h_y + O(\delta^2), \quad (3.2.2)$$

$$h_t + (uh)_x + (vh)_y = 0. \quad (3.2.3)$$

As will be seen shortly, the cross-channel geostrophic balance in (3.2.2) plays a role similar to that of the hydrostatic balance in preventing dispersive waves. This will allow semigeostrophic hydraulics to be discussed using the characteristic tools developed earlier.

From (3.2.1)-(3.2.3) follows the conservation law for potential vorticity:

$$\left(\frac{\partial}{\partial t} + u \frac{\partial}{\partial x} + v \frac{\partial}{\partial y} \right) \left(\frac{1-u}{h} \right)_y = 0. \quad (3.2.4)$$

Although general solutions to the semigeostrophic equations and their stability properties are unknown, we can find a special set of solutions to work with by assuming that the potential vorticity of the flow at some upstream section is constant. Equation (3.2.4) then implies that the potential vorticity is constant everywhere:

$$\frac{1-u_y}{h} = \phi, \quad (3.2.5)$$

say. This expression can be combined with (3.2.2) to form an equation for the cross-stream structure of h :

$$h_{yy} - \phi h = -1. \quad (3.2.6)$$

Thus, for $\phi > 0$:

$$h = \frac{1}{\phi} + A(x,t) \frac{\sinh(\phi^{1/2}y)}{\sinh(\phi^{1/2}w(x))} + B(x,t) \frac{\cosh(\phi^{1/2}y)}{\cosh(\phi^{1/2}w(x))} \quad (3.2.7)$$

and

$$u = -\phi^{1/2} \left[A(x,t) \frac{\cosh(\phi^{1/2}y)}{\sinh(\phi^{1/2}w(x))} + B(x,t) \frac{\sinh(\phi^{1/2}y)}{\cosh(\phi^{1/2}w(x))} \right] \quad (3.2.8)$$

In analyzing the x and t -dependence, it will be convenient to introduce the following dependent variables (Gill, 1977).

$$\bar{h} = \frac{h(x,w,t) + h(x,-w,t)}{2} = \phi^{-1} + B(x,t) \quad (3.2.9a)$$

$$\delta h = \frac{h(x,w,t) - h(x,-w,t)}{2} = A(x,t) \quad (3.2.9b)$$

$$\bar{u} = \frac{u(x,w,t) + u(x,-w,t)}{2} = -\phi^{1/2} T^{-1}(x) A(x,t) \quad (3.2.9c)$$

$$\delta u = \frac{u(x,w,t) - u(x,-w,t)}{2} = -\phi^{1/2} T(x) B(x,t), \quad (3.2.9d)$$

From (3.2.9) it follows that

$$\bar{u} = -\phi^{1/2} T^{-1} \delta h \quad (3.2.10)$$

$$\delta u = \phi^{1/2} T (\phi^{-1} - \bar{h}) \quad (3.2.11)$$

To find the x and t -dependence in the problem we evaluate Equation (3.2.1) on either side wall and apply the boundary condition

$$v_{\pm} = \pm \frac{1}{2} u_{\pm} \frac{dw}{dx} . \quad (3.2.12)$$

Taking the sum of the results and using (3.2.12) gives

$$2\bar{u}_t + (\bar{u}^2 + \delta u^2 + 2\bar{h})_x = -2 \frac{db}{dx} + \phi(u_+ h_+ - u_- h_-) \frac{dw}{dx} , \quad (3.2.13)$$

while the difference yields

$$2\delta u_t + 2(\bar{u}\delta u + \delta h)_x = \phi(u_+ h_+ + u_- h_-) \frac{dw}{dx} . \quad (3.2.14)$$

Equations (3.2.10) and (3.2.11) can now be used to eliminate δu and \bar{u} in favor of δh and \bar{h} :

$$\begin{aligned} \delta h_t - (\phi^{1/2} T^{-1} \delta h) \delta h_x + [\phi^{1/2} T^3 (\phi^{-1} - \bar{h}) - T \phi^{-1/2}] \bar{h}_x \\ = T \phi^{-1/2} \left[\frac{db}{dx} - \frac{\phi}{2} (u_+ h_+ - u_- h_-) \frac{dw}{dx} \right] \end{aligned} \quad (3.2.15)$$

$$\bar{h}_t - (\phi^{1/2} T^{-1} \bar{h}) \delta h_x - (\phi^{1/2} T^{-1} \delta h) \bar{h}_x = -\frac{1}{2} \phi^{1/2} T^{-1} (u_+ h_+ + u_- h_-) \frac{dw}{dx} \quad (3.2.16)$$

We now have two time-dependent equations for the two unknowns δh and \bar{h} . These equations take the quasilinear form (2.4.1) and may therefore be analyzed using the methods of section 2.4. We note that Gill's (1977) approach was somewhat different, as the emphasis was on steady solutions. Gill applied a steady Bernoulli equation (rather than a momentum equation) on each wall in order to obtain an algebraic expression for δh and \bar{h} .

3.3 Characteristic Equations and Riemann Functions

For the purposes of eigenvalue analysis it will be convenient to express (3.2.15) and (3.2.16) in the form

$$\frac{\partial u_i}{\partial t} + a_{ij} \frac{\partial u_j}{\partial x} = b_i \quad (3.3.1)$$

where

$$u_i = \begin{pmatrix} \delta h \\ \bar{h} \end{pmatrix} \quad (3.3.2)$$

$$a_{ij} = \begin{pmatrix} -\phi^{1/2} T^{-1} \delta h & \phi^{1/2} T^3 (\phi^{-1} \bar{h}) - T \phi^{-1/2} \\ -\phi^{1/2} T^{-1} \bar{h} & -\phi^{1/2} T^{-1} \delta h \end{pmatrix} \quad (3.3.2)$$

$$b_j = \begin{pmatrix} T \phi^{-1/2} \left[\frac{db}{dx} - \frac{\phi}{2} (u_+ h_+ - u_- h_-) \frac{dw}{dx} \right] \\ -\frac{1}{2} \phi^{1/2} T^{-1} (u_+ h_+ + u_- h_-) \frac{dw}{dx} \end{pmatrix} \quad (3.3.3)$$

The characteristic speeds are the eigenvalues of A_{ij} , namely:

$$\lambda_{\pm} = -\phi^{1/2} T^{-1} \delta h \pm \bar{h}^{1/2} [1 - T^2 (1 - \phi \bar{h})]^{1/2} \quad (3.3.4)$$

$$= \bar{u} \pm \bar{h}^{1/2} [1 - T^2 (1 - \phi \bar{h})]^{1/2}$$

Here λ_{\pm} can be interpreted as the speed of a Kelvin wave being advected at rate \bar{u} and propagating at rate $\pm \bar{h}^{1/2} [1 - T^2 (1 - \phi \bar{h})]^{1/2}$ relative to the current. Since $T < 1$ and $\phi > 0$, the latter term is always real and (3.1.17) therefore hyperbolic.

To obtain the characteristic forms of (3.3.1) we proceed as in section 2.4 and look for eigenvectors l_j such that

$$l_i a_{ij} = l_j \lambda_{\pm} .$$

By inspection of a_{ij} we see that one choice is

$$l_i = (-\phi^{1/2} T^{-1} \bar{h} \quad \phi^{1/2} T^{-1} \delta h + \lambda_{\pm}) . \quad (3.3.5)$$

The characteristic equations are determined from

$$l_i \left[\frac{\partial u_i}{\partial t} + a_{ij} \frac{\partial u_j}{\partial x} \right] = l_i b_i$$

which, after substitution of (3.3.2), (3.3.3), and (3.3.5) and some rearrangement, can be written as

$$\begin{aligned} -\phi^{1/2} T^{-1} \bar{h} \frac{D_{\pm}}{Dt} sh + (\phi^{1/2} T^{-1} sh + \lambda_{\pm}) \frac{D_{\pm} \bar{h}}{Dt} = -\bar{h} \frac{db}{dx} + [\bar{h} \frac{\phi}{2} (u_+ h_+ - u_- h_-) \\ - (\phi^{1/2} T^{-1} sh + \lambda_{\pm}) (\frac{1}{2} \phi^{1/2} T^{-1}) (u_+ h_+ + u_- h_-)] \frac{dw}{dx} \end{aligned}$$

where $\frac{D_{\pm}}{Dt} = \frac{\partial}{\partial t} + \lambda_{\pm} \frac{\partial}{\partial x}$.

To obtain the Riemann form, the above equation is divided by h and the term containing $D_{\pm} h/Dt$ integrated by parts with the aid of (3.3.5). This yields

$$\begin{aligned} \frac{D_{\pm}}{Dt} \{-\phi^{1/2} T^{-1} sh \pm \int \bar{h}^{-1/2} [1 - T^2(1 - \phi \bar{h})]^{1/2} d\bar{h}\} = -\frac{db}{dx} + \frac{1}{2} [\phi(u_+ h_+ - u_- h_-) \\ - \phi^{1/2} T^{-1} \bar{h}^{-1} (\phi^{1/2} T^{-1} sh + \lambda_{\pm}) (u_+ h_+ + u_- h_-)] \frac{dw}{dx}. \quad (3.3.6) \end{aligned}$$

The integral on the left hand side can be evaluated in closed form, the result being

$$\begin{aligned} \int \bar{h}^{-1/2} [1 - T^2(1 - \phi \bar{h})]^{1/2} d\bar{h} = [\bar{h}(1 - T^2) + T^2 \phi \bar{h}^2]^{1/2} \\ + \frac{1}{2} T^{-1} \phi^{-1/2} (1 - T^2) \ln \{ 2T\phi^{1/2} [\bar{h}(1 - T^2) + T^2 \phi \bar{h}^2]^{1/2} + 2T^2 \phi \bar{h} + (1 - T^2) \}. \end{aligned}$$

The Riemann functions are thus

$$\begin{aligned} R_{\pm} = -\phi^{-1} T^{1/2} sh \pm [(\bar{h}(1 - T^2) + T^2 \phi \bar{h}^2)^{1/2} + \frac{1}{2} T^{-1} \phi^{-1/2} (1 - T^2) \\ \ln \{ 2T \phi^{1/2} [\bar{h}(1 - T^2) + T^2 \phi \bar{h}^2]^{1/2} + 2T^2 \phi \bar{h} + (1 - T^2) \}]. \end{aligned}$$

It is further possible to simplify the bracketed term on the right-hand side of (3.3.6). This requires a considerable amount of algebra which is relegated to Appendix B. However the result allows (3.3.6) to be simplified to

$$\frac{D_{\pm}}{Dt} R_{\pm} = - \frac{db}{dx} - \frac{\phi^{1/2}}{2} [\phi^{-1}(\tau^{-1} - \tau^3)\bar{h} + \phi^{-2}(\tau^3 - \tau)] \frac{dw}{dx} \quad (3.3.7)$$

If both db/dx and dw/dx are zero then the Riemann functions are conserved along characteristics.

3.4 Steady Solutions

The steady solutions to (3.2.15) and (3.2.16) have been discussed by Whitehead, et al. (1974) for $\phi = 0$ and later by Gill (1977) for finite ϕ . We now review this theory using a slightly different derivation and make some additional comments concerning its application.

If the flow is steady, then a streamfunction exists for the mass transport:

$$\psi_x = vh \quad (3.4.1)$$

$$\psi_y = -uh \quad (3.4.2)$$

It can further be shown that the Bernoulli function $B = \frac{u^2}{2} + h + b$ and the potential vorticity are conserved along streamlines. From (3.2.1) it follows that

$$\frac{\partial B}{\partial x} = \frac{\partial \psi}{\partial x} \phi \quad (3.4.3)$$

so that

$$\phi = \frac{dB}{d\psi} \quad (3.4.4)$$

With the aid of (3.4.4) and (3.2.10,11) the momentum equations, (3.2.15) and (3.2.16), can now be written as exact differentials:

$$\begin{aligned}
 (\bar{u}^2 + \delta u^2 + 2\bar{h})_x &= (\Gamma^2 \phi \delta h^2 + \phi^2 \Gamma^2 (\phi^{-1} - \bar{h})^2 + 2\bar{h})_x \\
 &= -2 \frac{db}{dx} + \phi (u_+ h_+ - u_- h_-) \frac{dw}{dx} \\
 &= -2 \frac{db}{dx} + \phi \frac{\partial(\psi_+ + \psi_-)}{\partial x} \\
 &= (-2b + B_+ + B_-)_x
 \end{aligned}$$

and

$$(\bar{h} \delta u + \delta h)_x = \phi (\delta h \bar{h})_x = \phi (\psi_+ - \psi_-)_x$$

Integration with respect to x yields

$$\Gamma^2 \phi \delta h^2 + \phi^2 \Gamma^2 (\phi^{-1} - \bar{h})^2 + 2\bar{h} = -2b + B_+ + B_- \quad (3.4.5)$$

and

$$\delta h \bar{h} = (\psi_+ - \psi_-) = -Q \quad (3.4.6)$$

We can combine (3.4.5) and (3.4.6) into a single equation for h in terms of the averaged Bernoulli function $\bar{B} = (B_+ + B_-)/2$ and the mass flux Q :

$$\phi^2 \Gamma^2 (\phi^{-1} - \bar{h})^2 \bar{h}^2 + 2\bar{h}^3 + 2(b - \bar{B})\bar{h}^2 + \phi \Gamma^2 Q^{-2} = 0 \quad (3.4.7)$$

Some sample solutions for the interface elevation along the channel wall at x_w are sketched in Figure 3.2. The channel contains an obstacle followed downstream by a side contraction, and solutions are drawn for various values of \bar{B} .

The similarities with the non-rotating solutions (Figure 2.2) are clear. For $B > 4.35$ the interfaces maintain the upstream and

downstream elevations. At $\bar{B} = 4.35$ the solutions again coalesce, although the bifurcation now lies slightly downstream of the sill. Finally, the solutions lose continuity for $\bar{B} < 4.35$.

By (2.4.7) the flow at the bifurcation is critical:

$$\lambda_- = \bar{h}_c^{-1} T^{-1} Q \phi^{1/2} - \bar{h}_c^{1/2} [1 - T^2(1 - \phi \bar{h}_c)]^{1/2} = 0 \quad (3.4.8)$$

Again the upper curves are subcritical and the lower ones supercritical with respect to the Kelvin wave.

Gill (1977) further explores the properties of the solutions to (3.4.7), including the conditions for stagnation, flow reversal, and separation from the channel wall. Let it suffice to say here that, despite these interesting features, the solutions seem to possess the same hydraulics properties that are present in more classical solutions. It remains to see how the adjustment to a controlled state occurs and how restrictive the assumption of constant potential vorticity is. Before these questions are taken up, we mention some further results not discussed by Gill pertaining to the steady flow near the critical point.

3.5 The location of the Critical Point and Multiple Bifurcations

One feature of controlled flow over a dam or wier which is of great practical benefit is the critical condition, which gives a relation between the mass flux and the depth (e.g., Equation 2.1.8). Such wier formulas allow for measurement of the flow rate in an open channel without need for a current meter. The same sort of relation is obtained by setting $\lambda_- = 0$ in Equation (3.4.8):

$$Q = \phi^{-1/2} T \bar{h}_c^{3/2} [1 - T^2(1 - \phi \bar{h}_c)]^{1/2} \quad (3.5.1)$$

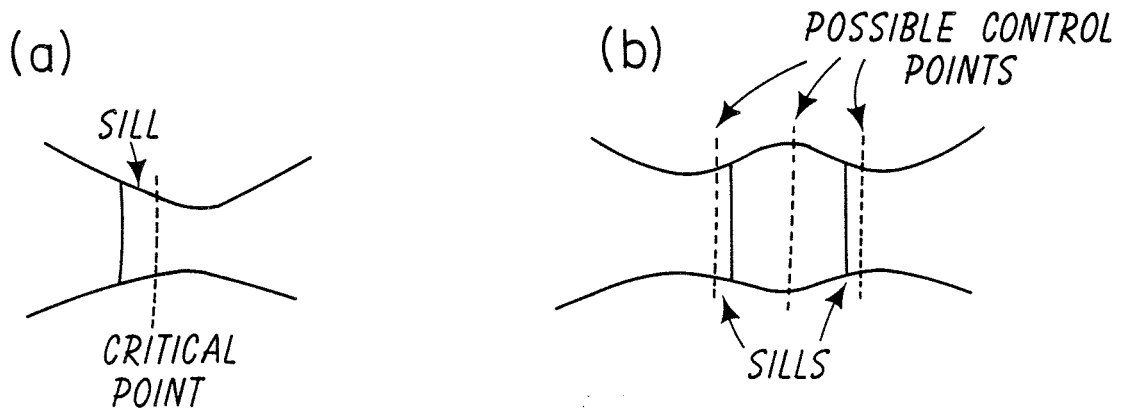


Figure 3.3

Critical point locations in straits with complicated geometry.

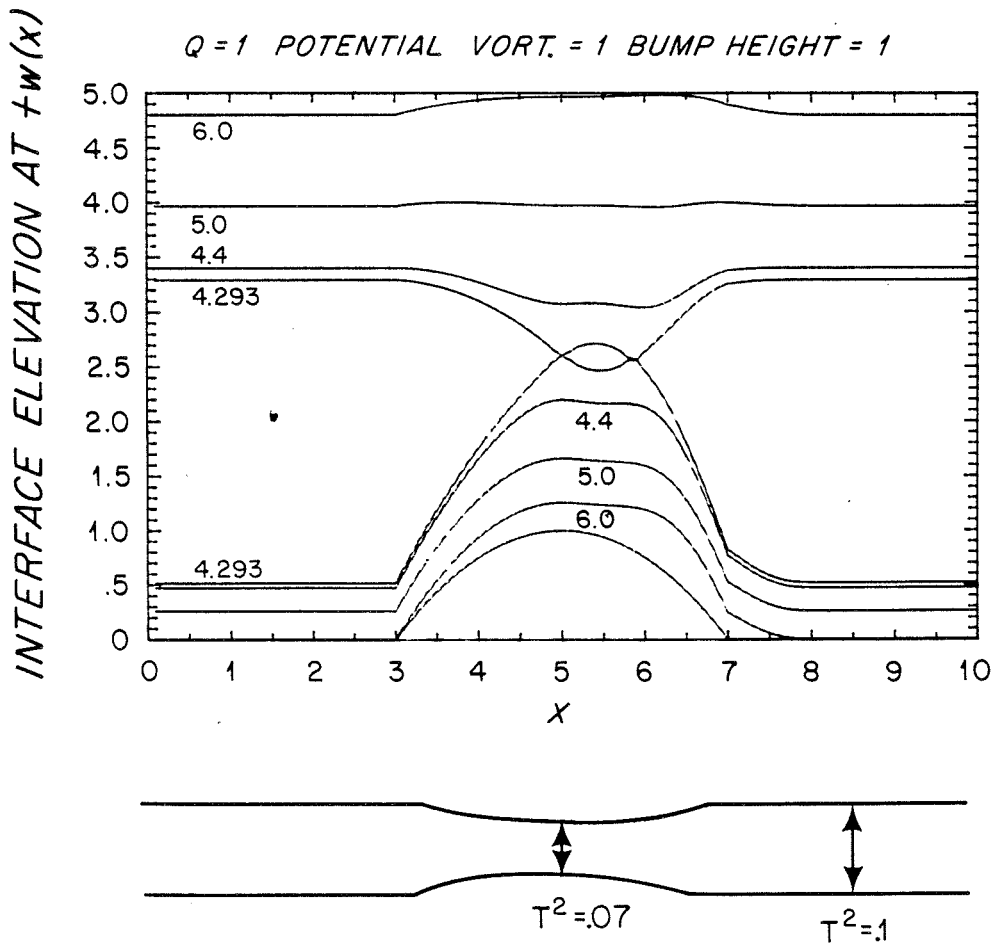


Figure 3.4

Solution with double bifurcation .

It has been suggested by other authors that 'wier formulas' such as (3.5.1) might be used to measure some of the deep ocean's overflows.

To apply (3.5.1) one must know the location of the critical point. Setting $\lambda_c = 0$ in (3.3.2) (or applying Equation 2.4.8) gives

$$\frac{db_c}{dx} = -\frac{1}{2} \phi^{1/2} [\phi^{-1} (T_c^{-1} - T_c^3) \bar{h}_c + \phi^{-2} (T_c^3 - T_c)] \frac{dw_c}{dx} \quad (3.5.2)$$

If the channel contains no side contractions ($dw/dx \equiv 0$), then the critical point occurs at the sill, where $db/dx = 0$, as in flow over a dam. Similarly, if the channel bottom is flat the critical point occurs at minimum width. If, however, both side contractions and bottom topography are present, as is generally the case in deep oceanic straits, the critical location will depend upon both the geometry and the bracketed term in (3.5.2). Since this term contains dependent flow variables the critical point may no longer be associated with a particular geometric feature, such as the sill. It can further be shown[†] that the bracketed term is greater than zero provided that no separation from the walls occurs. Given a channel with a single width contraction and single obstacle, as in Figure 3.3a, critical flow must therefore occur between the sill and the minimum width. Given more complicated geometries (Figure 3.3b), it is possible to find a number of candidates for critical flow.

If (3.5.2) contains multiple roots it is possible that several critical points exist. In Figure 3.4, for example, steady solutions with the same parameters as in Figure 3.2 have been computed for slightly different channel geometry. The transitional curves now contain two bifurcations: one near the sill and the other between the sill and the

[†] See Appendix B.

minimum width. The problem of branch selection is now more complicated and will be taken up in a later section.

The situation is even more complex if the fields vary slowly with time. In this case (3.5.2) continues to hold with \bar{h} a parametric function of time. If both bottom topography and side contractions exist then the critical point is free to move about between the sill and the minimum width.

The conclusion is that isolation of the critical point may be difficult in deep straits, where complicated geometry is the rule. Caution is therefore advised to those who would apply wier formulas to deep overflows.

3.6 Establishment of Steady Solutions

The fact that the semigeostrophic equations (3.2.1-3) are hyperbolic for constant potential vorticity allows us to discuss adjustment to small disturbances in the same manner as Chapter 2. In particular, the Riemann form (3.3.7) can be used to show that our ideas about stability and upstream influence under steady and unsteady conditions remain unchanged.

The problem of adjustment to large changes in channel geometry is more subtle, however, as will be seen presently. We attempt to study this problem as before; through numerical solutions for the flow that results from obtrusion of an obstacle. The initial state consists of a geostrophically balanced stream with velocity $u_0(y)$ and depth $h_0(y)$ over a flat bottom. At $t = 0$ an obstacle is quickly grown to a height b_0 and the adjustment to a steady state is observed. The solution is computed using a modified version of the Lax-Wendroff scheme (Appendix A)

which integrates the full set of two-dimensional equations. The horizontal aspect ratio, w/L , of the channel is $1/5$.

The first set of experiments carried out were done using an initial state with constant potential vorticity. In this case the critical obstacle height, b_c , is given in terms of the initial parameters ϕ_0 , Q_0 , and \bar{B}_0 by (3.4.6), (3.4.7) and (3.4.8). Combining the latter two gives an equation for the critical value of \bar{h} in a flow with upstream parameters ϕ_0 , Q_0 , \bar{B}_0 , and the obstacle height b_c .

$$\phi_0 T_c^2 (\phi_0^{-1} - \bar{h}_c) (\phi_0^{-1} - 2\bar{h}_c) + 3\bar{h}_c = 2(\bar{B}_0 - b_c) \quad (3.6.1)$$

A relationship between Q_0 , ϕ_0 and \bar{h}_c can also be derived by combining (3.4.6) and (3.4.8):

$$\bar{h}_c^4 + \bar{h}_c^3 \phi_0^{-1} (T_c^{-2} - 1) - T_c^{-4} Q_0^2 = 0. \quad (3.6.2)$$

Equations (3.6.1) and (3.6.2) give the maximum obstacle height, b_c , over which a steady flow with upstream parameters Q_0 , ϕ_0 and \bar{B} is able to flow. In the numerical experiments the adjustment again depends crucially on how high the obstacle is grown in relation to b_c . If $b_0 < b_c$ the adjustment is similar to that shown in Figure 3.5. After 20 time steps, the obstacle has caused a bulge in the interface. After 60 time steps, the bulge has split into two Kelvin waves moving upstream and downstream relative to the flow. Finally, after 100 time steps, the Kelvin waves have moved completely away from the obstacle leaving a subcritical dip in the interface.

If $b_0 \geq b_c$ the adjustment is quite different, as shown in Figure 3.6. Instead of isolated Kelvin waves, the bulge has now developed into two fronts. After 80 time steps, these fronts have moved completely away from

the obstacle leaving behind a transitional steady flow with a hydraulic jump in the lee of the sill. The upstream front steepens and eventually forms a breaking bore.

Unfortunately the stability properties of the numerical method are much worse than those of the one-dimensional scheme used in the previous chapter (see Appendix A). In Figure 3.6, some numerical instabilities appearing as small parasitic waves can be seen on the crest of the hydraulic jump. Long after the adjustment is complete (400 or 500 time steps) these instabilities grow large enough to invalidate the computation. Because of this, some of the experiments done in Chapter 2, such as the hysteresis problem and the experiments with periodic flows, were impossible.

Numerical solutions were also obtained for initial states having nonconstant potential vorticity.[†] Because of the lack of an analytic theory for such flows, the dependence of the asymptotic state on a critical obstacle height is more difficult to formulate. However, the results display the same qualitative behavior as those discussed above. For b_0 less than some (unknown) critical height b_c , the adjustment is similar to that of Figure 3.5; the asymptotic state is symmetric about the sill and no upstream influence is present. If $b_0 > b_c$ the situation is similar to that of Figure 3.6. Apparently, classical hydraulic properties apply to semigeostrophic flows in general, at least over the time scales modelled numerically. It is possible that another process, such as barotropic instability, might affect the flow on longer time scales.

[†] In the initial flow, the potential vorticity typically increased monotonically by a factor of two from $y = -w$ to $y = +w$.

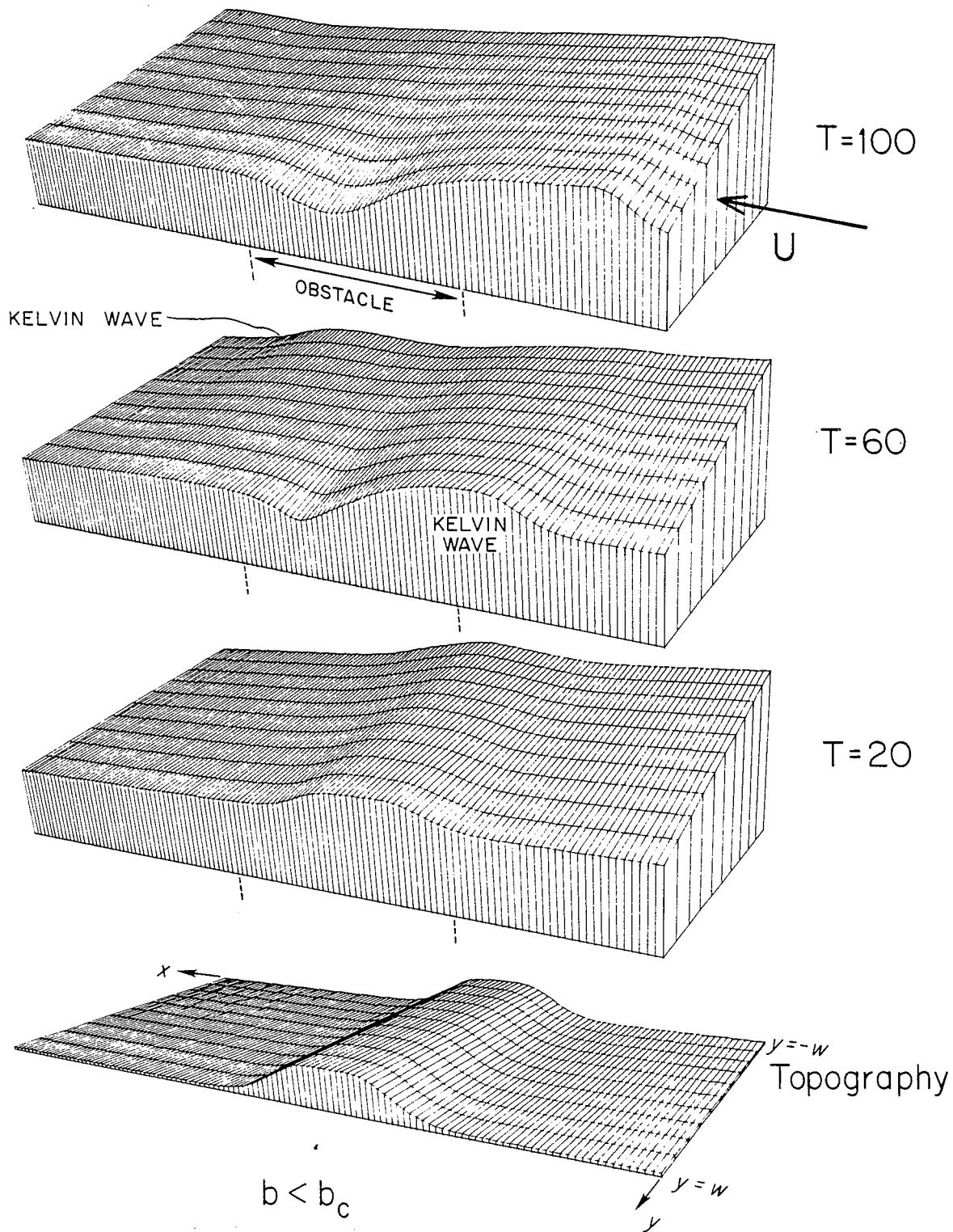


Figure 3.6
Semigeostrophic adjustment to obstacle.

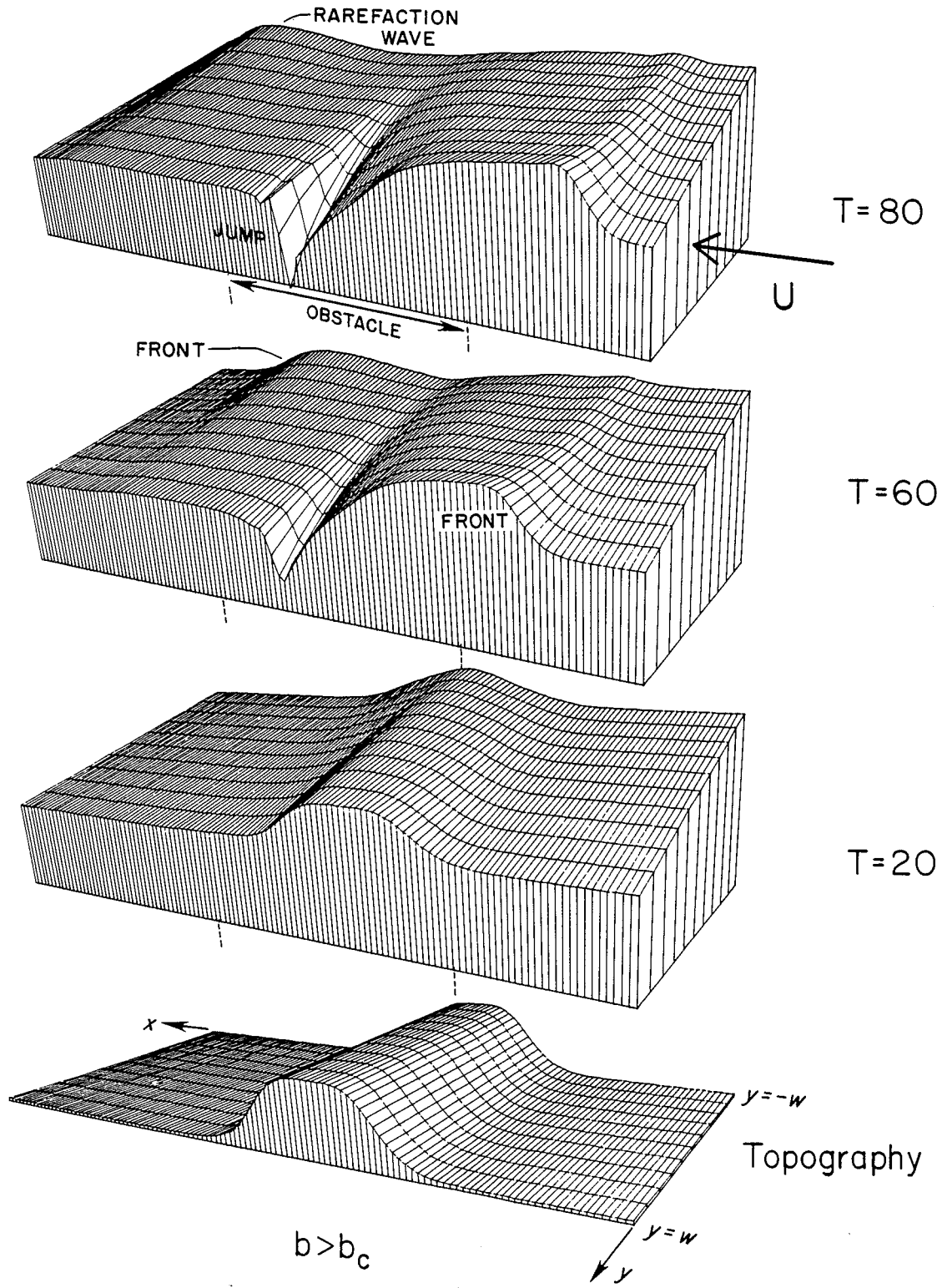


Figure 3.5
Semigeostrophic adjustment to obstacle.

3.7 Free-surface shocks

It is not surprising that breaking waves play an important role in semigeostrophic adjustment to a controlled state and in the asymptotic state itself. We now make a closer examination of these free-surface shocks and try to determine how the upstream and downstream states are connected.

Let us first relax the narrow channel approximation and consider a shock which exists in a channel flow of arbitrary width. Although the interior of the shock is a complicated region in which the shallow-water approximation breaks down, we again may attempt to connect the upstream and downstream states through mass and momentum continuity. The conservation laws for momentum flux are obtained by multiplication of (3.1.1) and (3.1.2) (with $\delta = R_0 = 1$) by h and integration by parts. The results are

$$(uh)_t + (u^2h + h^2/2)_x + (uvh)_y = -h \frac{db}{dx} + hv \quad (3.7.1)$$

$$(vh)_t + (uvh)_x + (v^2h + h^2/2)_y = -uh \quad (3.7.2)$$

The continuity equation,

$$h_t + (uh)_x + (vh)_y = 0, \quad (3.7.3)$$

is already in conservation law form.

Without any loss in generality, we can align the y -axis perpendicular to and the x -axis normal to the shock at some point P . Upon integration across the shock and shrinkage of the interval of integration to zero, only contributions from the x and t -derivatives will remain finite. For example, integration of the continuity equation (3.7.3) from $A < x(P)$ to $B > x(P)$ gives

$$\int_B^A \{h_t + (uh)_x + (vh)_y\} dx = \int_A^\eta h_t dx + \int_\eta^B h_t dx + u_B h_B - u_A h_A + \int_A^B (vh)_y dx,$$

where η is the x-position of the shock.

Applying Leibnitz's rule to the first two terms on the right hand side of the above equation and letting $A \rightarrow \eta_-$, and $B \rightarrow \eta_+$, we find

$$(h_A - h_B) \frac{d\eta}{dt} + u_B h_B - u_A h_A = 0.$$

or

$$c \left[\frac{h}{B} \right] - \left[\frac{u^{(n)} h}{A} \right] = 0 \quad (3.7.4)$$

where $c = \frac{d\eta}{dt}$ is the velocity of the shock normal to itself and $u^{(n)}$ is the velocity normal to the shock.[†] Integrating (3.7.1) and (3.7.2) and applying the same notation yields:

$$c \left[\frac{u^{(n)} h}{A} \right] - \left[\frac{u^{(n)2} h + h^2/2}{B} \right] = 0 \quad (3.7.5)$$

$$c \left[\frac{u^{(s)} h}{B} \right] - \left[\frac{u^{(n)} u^{(s)} h}{A} \right] = 0 \quad (3.7.6)$$

where $u^{(s)}$ is the velocity tangent to the shock.

Equations (3.7.4) and (3.7.5) are the familiar conditions on mass and momentum flux that apply to one-dimensional shocks. The third relation can be simplified to

$$\left[\frac{u^{(s)}}{A} \right] = 0 \quad (3.7.7)$$

upon combination with (3.7.4). Therefore the tangential velocity is continuous, implying that the potential vorticity, $(1 + \frac{\partial u^{(s)}}{\partial n} - \frac{\partial u^{(n)}}{\partial s})/h$,

[†] We equate u and v with $u^{(n)}$ and $u^{(s)}$ to avoid future confusion between rotated and nonrotated x, y coordinates.

of a fluid parcel crossing the shock must remain finite -- though not necessarily conserved.

If $u^{(s)} \neq 0$, then (3.7.7) further implies that the velocity vector must change direction upon passing the shock. This demands that the shock become perpendicular to any solid boundary at the point of that contact, otherwise the shock would induce a flow normal to the boundary. More generally, the shock must become aligned perpendicular to x as $v/u \rightarrow 0$.

In general, given $u_A^{(n)}$, $u_A^{(s)}$, and h_A one can compute the downstream fields $u_B^{(n)}$, $u_B^{(s)}$, and h_B using (3.7.4), (3.7.5), and (3.7.7), provided that c is known. The narrow channel case is apparently simpler since $v/u \rightarrow 0$ and the entire shock should be described by a single velocity, c . Under these conditions, it is tempting to describe the shock as a weak solution to the semigeostrophic equations (3.2.1)- (3.2.3). In such a description, the flow would be semigeostrophic at all points not on the shock. Such temptation should be resisted, however, since Equations (3.7.4, 5, and 7) make no allowance for geostrophy. That is, given a geostrophically balanced upstream state, there is no guarantee that the state immediately downstream of the shock (as computed using (3.7.4, 5, and 7)) will be geostrophic.[†] The shock must be bordered by a dispersive region in which the terms $\delta^2(v_t + uv_x + vv_y)$ becomes as large as u and h_y . The width of this dispersive region is $O(\delta)$ (the deformation radius) and its role is to adjust the shock to the semigeostrophic flow on either side.

[†] Being proportional to velocity (and not its derivative) rotation must act over a finite distance. Thus, rotational terms do not appear in the Rankine-Hugoniot conditions (3.7.4-7).

Figure 3.7 shows how the y-momentum balance changes as a front steepens into a bore. The information is taken from the upstream moving front in Figure 3.6. Initially the flow is semigeostrophic (Figure 3.7a) but the geostrophic balance weakens as the front steepens. This is due to the Kelvin wave dynamics which are decreasing the slope of the interface. Meanwhile, the term $\delta^2 v_t$ is becoming significant over an $O(\delta)$ interval about the front (Figure 3.7b-d).

Is it possible to connect the flow upstream of the dispersive region to that downstream without resolving the complicated region in between? In general, the answer is no. However it is possible to derive approximate formulas for special cases. One such case is typified by the shocks observed in the numerical experiments. These shocks and their surrounding dispersive region translate with little change in form at a fixed speed, c_x , along the channel. The translation speed is related to the normal speed, c , through

$$c = c_x \cos \theta$$

where θ is the inclination of the shock with respect to the y-axis (see Figure 3.8). We would like to investigate the conditions under which the momentum flux gained in the translating dispersive region is negligibly small.

First consider the momentum flux at the bore itself. From (3.7.5) and (3.7.6) we can write

$$\left[\underset{A}{(c - u^{(n)})} \underset{B}{u^{(n)} h} - \underset{B}{h^2/2} \right] \cos \theta + \left[\underset{A}{(c - u^{(n)})} \underset{B}{u^{(s)} h} \right] \sin \theta = 0 ,$$

as both terms are identically zero. From this it follows that

$$\left[\underset{A}{(c - u^{(n)})} \underset{B}{h} (u^{(n)} \cos \theta + u^{(s)} \sin \theta) - \underset{B}{h^2/2} \cos \theta \right] = 0$$

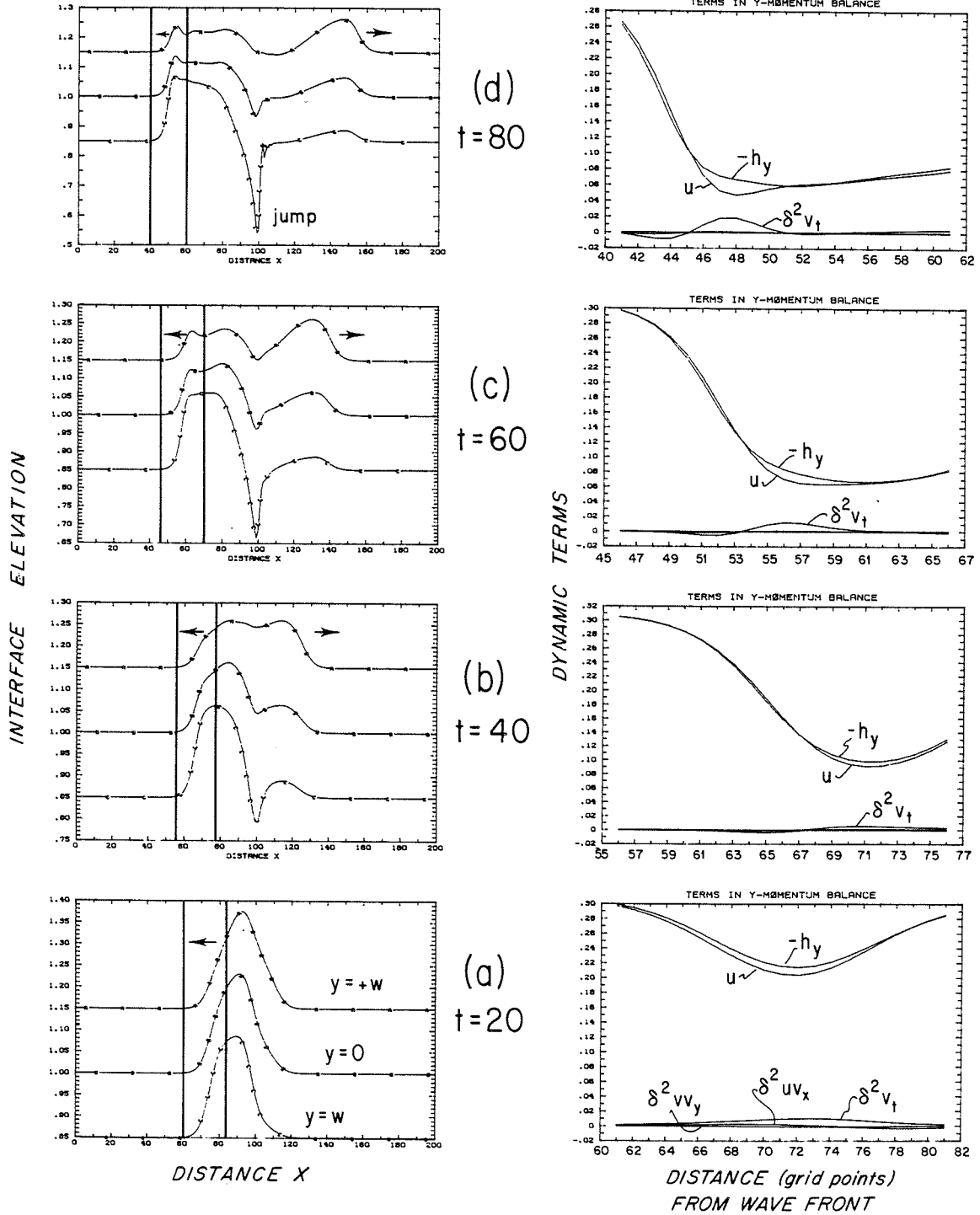


Figure 3.7
Evolution of front (located between solid lines) and corresponding momentum terms.

or

$$\left[(c - u^{(n)})uh - \frac{h^2}{2} \cos\theta \right]_A^B = 0 \quad (3.7.8)$$

We next write the x-momentum flux Equation (3.7.1) in a frame translating with the bore. The result is

$$-c_x(uh)_x + (u^2h + h^2/2)_x + (uvh)_y = -h\left(\frac{db}{dx} - v\right)$$

or

$$\nabla \cdot \left\{ (u - c_x)uh + \frac{h^2}{2}, uvh \right\} = -h\left(\frac{db}{dx} - v\right)$$

Integrating over the upstream dispersive region (labeled R_A in Figure 3.8) and applying the divergence theorem gives

$$\int_{\partial R_A} \left\{ (u - c_x)uh + \frac{h^2}{2}, uvh \right\} \cdot \hat{n} = - \iiint_{R_A} h\left(\frac{db}{dx} - v\right) d\sigma$$

where \hat{n} is the unit normal to ∂R_A . Along each wall, where $n = j$ and $v = 0$, the contour integral vanishes. Along the upstream border of R_A , where $x = A'$, we have $n = i$. Therefore

$$\begin{aligned} & \int_{\partial R_A} \left\{ (u - c_x)uh + \frac{h^2}{2}, uvh \right\} \cdot \hat{n} \\ &= \int_{-w}^w \left\{ (u - c_x)uh + \frac{h^2}{2} \right\}_{A'} dy - \int_{s(-w)}^{s(w)} \left\{ \left((u - c_x)uh + \frac{h^2}{2} \right) \cos\theta + uvh \sin\theta \right\}_A ds \\ &= \int_{-w}^w \left\{ (u - c_x)uh + \frac{h^2}{2} \right\}_{A'} dy - \int_{s(-w)}^{s(w)} \left\{ (u^{(n)} - c)uh + \frac{h^2}{2} \right\}_A ds = - \iiint_{R_A} h\left(\frac{db}{dx} - v\right) d\sigma \end{aligned} \quad (3.7.9)$$

with s measured along the bore.

Following the same procedure in R_B , it can be shown that

$$\int_{-w}^w \left\{ (u - c_x)uh + \frac{h^2}{2} \right\}_{B'} dy - \int_{s(-w)}^{s(w)} \left\{ (u^{(n)} - c)uh + \frac{h^2}{2} \right\}_B ds = \iiint_{R_B} h\left(\frac{db}{dx} - v\right) d\sigma$$

Subtracting this from (3.7.9) and applying (3.7.8) finally gives

$$\left[\int_{A'}^{B'} \int_{-w}^w \left\{ (u - c_x)uh + \frac{h^2}{2} \right\} dy \right]_{B'} = - \iint_{R_A + R_B} h \left(\frac{db}{dx} - v \right) d\sigma \quad (3.7.10)$$

Since the area of $R_1 + R_2$ is $O(\delta^2)$, the right-hand side of (3.7.10) is $O(\delta)$ less than the left-hand side. Thus, for narrow channels we have

$$\left[\int_{A'}^{B'} \int_{-w}^w \left\{ (u - c_x)uh + \frac{h^2}{2} \right\} dy \right]_{B'} = O(\delta^2) .^\dagger \quad (3.7.11)$$

This is simply a statement that a translating narrow-channel bore can be treated to $O(\delta)$ error as if it were a weak solution. The same procedure can be used to formulate the mass balance between A' and B' . In this case, the connection formula is

$$\left[\int_{A'}^{B'} \int_{-w}^w (u - c_x)h dy \right]_{B'} = 0 \quad (3.7.12)$$

Suppose $u_{A'}(y)$, $h_{A'}(y)$ (and thus $\phi_{A'}(y)$) and c_x are given. Are $u_{B'}(y)$ and $h_{B'}(y)$ then uniquely determined by (3.7.11) and (3.7.12)? Since the flow at A' and B' is semigeostrophic, Equations (3.2.2) and (3.2.5) can be combined into a single equation for $h_{B'}$:

$$\frac{\partial^2}{\partial y^2} h_{B'} - \phi_{B'} h_{B'} = -1 \quad (3.7.13)$$

[†] An alternate form of (3.7.11) which is accurate to the same order can be derived through integration along the side walls, rather than over R_1 and R_2 . Taking advantage of the fact that $v = \theta = 0$ at the wall, we find

$$\left[(u_{\pm} - c_x)u_{\pm}h_{\pm} + h_{\pm}^2/2 \right]_{B'} = O(\delta) \quad (3.7.11a)$$

For suitably well behaved $\phi_{B'}(y)$, solutions will exist and contain two arbitrary constants. Equations (3.7.11) and (3.7.12) provide two equations for their downstream values, provided that (3.7.13) can be solved. However, the solution depends on the potential vorticity at B' , which is yet unknown. If $\phi(y)$ does not change from A' to B' by more than an $O(\delta)$ amount, it is self consistent to set $\phi_{A'}(y) = \phi_{B'}(y)$. Recall that Equations (3.7.4)-(3.7.7) say nothing about continuity of ϕ at the shock, but only that it remains finite. We therefore return to the equations of motion and the numerical model in an attempt to gain insight into the behavior of ϕ near a discontinuity.

3.8 The change in potential vorticity across a shock

Again consider a shock and dispersive region which translate along the channel with speed c_x . In a reference frame moving with the shock the vector momentum equation for the flow becomes

$$-c_x \frac{\partial \hat{u}}{\partial x} + (\hat{u} \cdot \nabla) \hat{u} - kx \hat{u} + \nabla(h + b) = 0. \quad (3.8.1)$$

As before, we rotate the translating coordinates (x,y) into new coordinates (n,s) such that s is tangent to the shock at a point P .

Thus

$$\frac{\partial}{\partial x} = \cos\theta \frac{\partial}{\partial n} - \sin\theta \frac{\partial}{\partial s}, \quad (3.8.2)$$

where θ is measured between the shock and the y -axis.

The change in potential vorticity across the shock is[†]

$$[\phi] = \left[\frac{1}{h} \right] - \left[\frac{\partial u^{(n)}}{h \partial s} \right] + \left[\frac{\partial u^{(s)}}{h \partial n} \right]. \quad (3.8.3)$$

[†] It is understood that $[]$ denotes $\left[\begin{matrix} A \\ B \end{matrix} \right]$, where A and B lie immediately on either side of the shock.

Suppose conditions upstream of the shock are given. Since s -derivatives are allowed, the first two terms on the right of (3.8.3) can be evaluated directly using Equations (3.7.4) and (3.7.5). It remains to find an expression for $\partial u(s)/\partial n$ in terms of s -derivatives alone. Such an expression is provided by the tangential component of (3.8.1):

$$-c_x \cos \theta \frac{\partial u(s)}{\partial n} + c_x \sin \theta \frac{\partial u(s)}{\partial s} + u^{(n)} \frac{\partial u(s)}{\partial n} + u(s) \frac{\partial u(s)}{\partial s} + u^{(n)} \frac{\partial h}{\partial s} + \frac{\partial b}{\partial s} = 0$$

This equation can be rearranged to form

$$\frac{\partial u(s)/\partial n}{h} = \frac{1}{h(c - u^{(n)})} (c_x \sin \theta \frac{\partial u(s)}{\partial s} + u(s) \frac{\partial u(s)}{\partial s} + u^{(n)} + \frac{\partial h}{\partial s} + \frac{\partial b}{\partial s})$$

where $c = c_x \cos \theta$ is the velocity of the shock normal to itself. The term $h(c - u^{(n)})$ is conserved in view of (3.7.4). Taking jumps and using (3.7.7) to eliminate the first two terms on the right hand side, we find

$$\left[\frac{\partial u(s)/\partial n}{h} \right] = \frac{1}{h(c - u^{(n)})} ([u^{(n)}] + \frac{\partial}{\partial s} [h])$$

It follows that from (3.8.3) that

$$\begin{aligned} [\phi] &= \left[\frac{1 + \frac{\partial u(s)}{\partial h} - \frac{\partial u^{(n)}}{\partial s}}{h} \right] = \left[\frac{[u^{(n)} + \frac{\partial h}{\partial s}]}{h(c - u^{(n)})} \right] + \left[\frac{1 - \frac{\partial h^{(n)}}{\partial s}}{h} \right] \\ &= \frac{-[u^{(n)} + \frac{\partial h}{\partial s} + (c - u^{(n)})(1 - \frac{\partial h^{(n)}}{\partial s})]}{h(u^{(n)} - c)} \\ &= \frac{-[(u^{(n)} - c) \frac{\partial u^{(n)}}{\partial s} + \frac{\partial h}{\partial s}]}{h(u^{(n)} - c)} \end{aligned} \quad (3.8.4)$$

There are several special cases in which (3.8.4) can further be simplified. If the shock forms a straight line ($c = \text{constant}$), then

$$\begin{aligned}
 [\phi] &= \frac{-[(u^{(n)} - c) \frac{\partial}{\partial s} (u^{(n)} - c) + \frac{\partial h}{\partial s}]}{h(u^{(n)} - c)} \\
 &= \frac{-\frac{\partial}{\partial s} [\frac{1}{2} (u^{(n)} - c)^2 + \frac{1}{2} u^{(s)2} + h]}{h(u^{(n)} - c)} \\
 &= \frac{-\frac{\partial}{\partial s} [B]}{Vh} \tag{3.8.5}
 \end{aligned}$$

where $V = u^{(n)} - c$ is the normal fluid velocity seen in the moving frame, and $B = \frac{1}{2}(V^2 + u^{(s)2}) + h$ is the Bernoulli function based on this velocity. Vh is thus a conserved quantity.

The change in potential vorticity is thus related to the rate of energy dissipation within the shock. It is possible to express this change in terms of the jump in height alone. We first note that

$$Vh[u] = -[h^2/2] \tag{3.8.6}$$

in view of (3.7.5). Therefore

$$\begin{aligned}
 [B] &= [\frac{1}{2} (V^2 + u^{(s)2}) + h] = [\frac{1}{2} V^2 + h] \\
 &= \frac{1}{2} (V_B - V_A)(V_B + V_A) + h_B - h_A \\
 &= \frac{1}{2} (u_B - u_A)(V_B + V_A) + h_B - h_A
 \end{aligned}$$

From (3.8.6) it follows that

Figure 3.8

Translating shock and dispersive region.

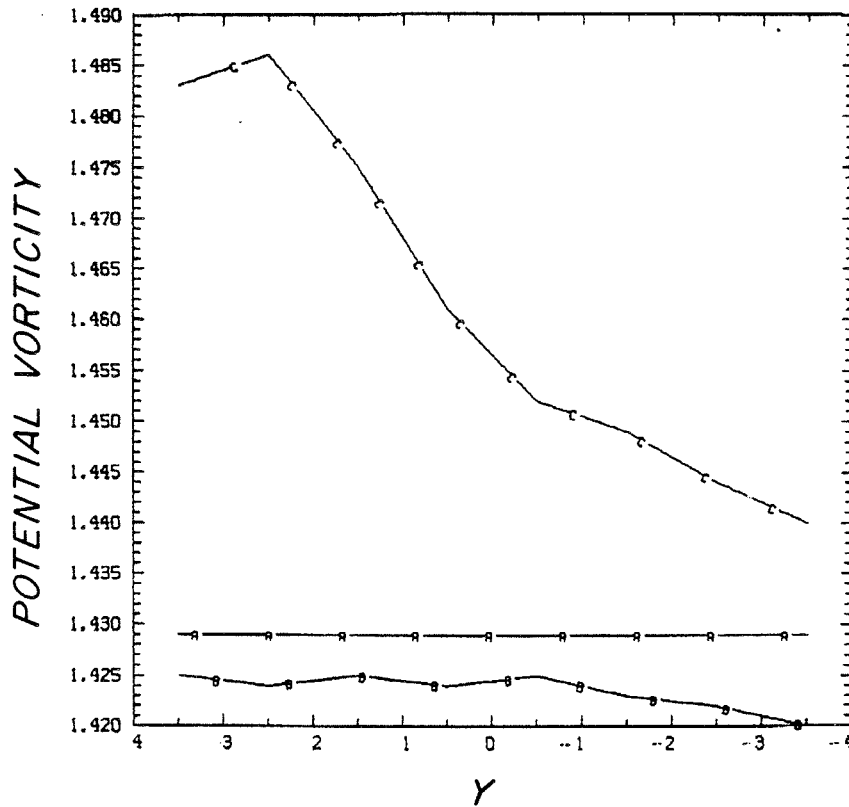
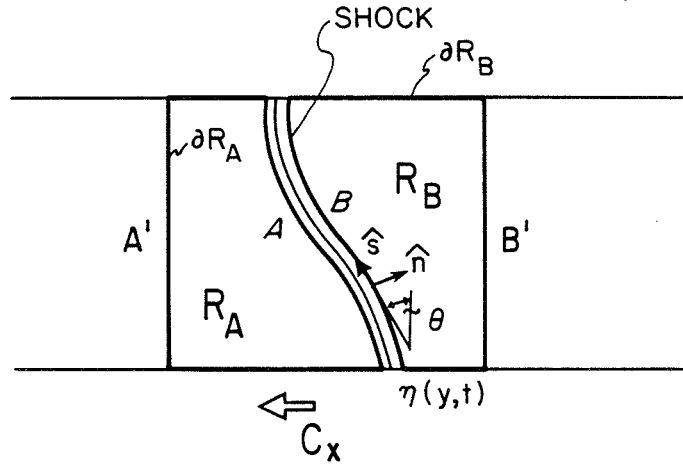


Figure 3.9

Cross-sections of potential vorticity taken from the flow shown in Figure 3.6. Section A is taken upstream of the bore, section B between the bore and the jump, and section C downstream of the jump.

$$\begin{aligned}
[B] &= \frac{1}{4} (h_A^2 - h_B^2) \left(\frac{1}{h_B} + \frac{1}{h_A} \right) + h_B - h_A \\
&= \frac{1}{4h_B h_A} [(h_A^2 - h_B^2)(h_A + h_B) + 4h_B^2 h_A - 4h_A^2 h_B] \\
&= \frac{1}{4h_B h_A} (h_A - h_B)^3
\end{aligned}$$

Substitution into (3.8.5) finally gives

$$[\phi] = \frac{1}{4Vh} \frac{\partial}{\partial s} \left\{ \frac{[h]^3}{h_B h_A} \right\} \quad (3.8.7)$$

It is interesting to observe the values of $[\phi]$ in the numerical solutions of Figure 3.6. This information is displayed in Figure 3.9, which contains potential vorticity profiles at three sections along the channel. The first (labeled 'A' in Figure 3.6) is taken upstream of the bore. Here $\phi = \text{constant}$, as this was imposed as the initial condition. The second section (labeled 'B') was taken between the bore and the jump. Here ϕ has decreased by a small amount which is probably within the limits of numerical error. The final section (labeled 'C') is taken downstream of the jump, and the potential vorticity here increases by a significant amount.

Are these results consistent with Equation (3.8.7)? First consider the hydraulic jump, for which $Vh = uh$. This jump is essentially a breaking Kelvin wave which is frozen in the supercritical flow downstream of the sill. The largest values of $[h]$ thus tend to occur on the left side of the channel, that is

$$\frac{\partial}{\partial s} \left\{ \frac{[h]^3}{h_B h_A} \right\} > 0$$

The change in potential vorticity is therefore positive, as verified by the numerical results. This change is most intense on the near side of the channel where the boundary layer contribution to $[h]^3$ is greatest.

Analysis of the bore is also possible since the angle θ was observed to remain approximately zero throughout the upstream propagation. Equation (3.8.6) is then allowed with $V = u_A - c = u_A - c_X$. Since $c < 0$, the term Vh will be larger in general than the corresponding value for the jump. Furthermore the upstream depths h_B and h_A are somewhat larger and the change in depth, $[h]$, somewhat smaller. Therefore, the magnitude of $[\phi]$ is less than above and this is again verified in Figure 3.9.

A more precise verification of the magnitude of $[\phi]$ is difficult owing to the difficulty in measuring $[h]$ from numerical data. (The numerical model smears the shocks over five or six grid points and it is difficult to judge which portion of the surface breaks and which simply has a steep slope.) However, using values of $[h]$ taken from the jump at $x = 100$ in Figure 3.7d we can estimate

$$\begin{aligned} [\phi] &= \frac{1}{4Vh} \frac{\partial}{\partial s} \left\{ \frac{[h]^3}{h_A h_B} \right\} \\ &\approx \frac{1}{4(.6)} \left\{ \frac{[h]_+^3}{h_{A+} h_{B+}} - \frac{[h]_-^3}{h_{A-} h_{B-}} \right\} \\ &\approx \frac{1}{4(.6)} \left\{ \frac{(.3)^3}{(.5)(.8)} - 0 \right\} = .03 . \end{aligned}$$

which agrees with the order of magnitude of change shown in Figure 3.9.

The changes in ϕ plotted in Figure 3.10 are small compared with ϕ itself. Hence, the connection formulas (3.7.11) and (3.7.12) can accurately be applied in conjunction with (3.7.13) by assuming that $[\phi] = 0$. It is not known whether larger jumps produce larger changes in ϕ , since the numerical experiments in which they arise tend to be numerically unstable. This is a question which may have to be settled experimentally.

It is also natural to ask how the changes in ϕ affect the stability of the flow. Semigeostrophic instability is a problem which has only begun to be explored (see Orlandi (1968) and Griffiths et al. (1982)). However, we envision the flow downstream of the obstacle emptying into a large basin and the dynamics becoming quasigeostrophic there. The barotropic stability of the flow will then depend on the Fjortoft (1952) criterion that $d\phi/d\psi$ must vanish for instability to occur. However, $\phi(\psi)$ is set at the hydraulic jump.

By varying the initial potential vorticity distribution, it is possible to find flows numerically which satisfy the Fjortoft criterion upstream but not downstream of the jump and vice versa. Unfortunately, it is impractical to study the growth of possible instabilities because of the time limits imposed by the growth of numerical instabilities. Again, this is a problem more suitable for laboratory experimentation.

3.9 Total Blockage by the Obstacle

As in the nonrotating case, we expect that a semigeostrophic channel flow will be completely blocked if the obstructing obstacle is high

enough. Although this situation is difficult to model numerically, we can piece together a scenario describing the blockage and predict the required obstacle height by extrapolating the numerical results for partial blockage. The following discussion assumes the change in potential vorticity across the blocking bore to be $O(\delta)$, as occurs in the numerical results. Although there is no guarantee that $[\phi]$ will continue to be small for large bores, it is hoped that the following analysis will provide a starting point in the theory of total blockage and spur experimental investigation into the problem. We will limit the discussion to initially subcritical flows.

As before, we assume that the blockage will be accomplished through formation of a bore which moves upstream from the obstacle, leaving behind a stagnant region (Figure 3.10). If the flow in the stagnant region (labeled B) is steady, then

$$\int_{-w}^{+w} u_B h_B dy = \frac{1}{2} (h_{B+}^2 - h_{B-}^2) = 0 ,$$

in view of (3.2.2).

The depth on either wall is therefore the same:

$$h_{B+} = h_{B-} . \quad (3.9.1)$$

Since no fluid passes the sill, the streamline at $+w$ connects with that at $-w$. Therefore, the Bernoulli law demands that

$$u_{B+}^2 = u_{B-}^2 \quad (3.9.2)$$

away from the obstacle. Furthermore, since $u = 0$ at the sill the obstacle must have height

$$b_b = \frac{u_{B+}^2}{2} + h_{B+} = \frac{u_{B-}^2}{2} + h_{B-} . \quad (3.9.3)$$

If the change in potential vorticity across the bore is $O(\delta)$ then Equations (3.2.7) and (3.2.8) continue to hold in the stagnant region.

In this case

$$\bar{u} = -\phi^{1/2} T^{-1} \delta h = 0$$

so that negative root of (3.9.2) is appropriate

$$u_{B-} = -u_{B+} . \quad (3.9.4)$$

Using (3.9.4) and (3.9.2) it can be shown that

$$h_B(x) = \phi^{-1+} (h_+(x) - \phi^{-1}) \frac{\cosh(\phi^{1/2} y)}{\cosh(\phi^{1/2} w)}$$

and

$$u_B(x) = \phi^{1/2} (\phi^{-1} - h_+(x)) \frac{\sinh(\phi^{1/2} y)}{\cosh(\phi^{1/2} w)} .$$

The circulation in the stagnant region therefore consists of a cyclonic eddy that is symmetric with respect to y . Away from the obstacle the flow is uniform with respect to x , implying that $v = 0$. The recirculation is fed over the topography, where approaching fluid is turned to the left and develops an $O(\delta)$ cross-channel velocity.

Under these assumptions, it is possible to predict the blocking height, b_b , given the initial flow rate, Q_0 , and energy B_0 . Applying (3.7.12) across the bore gives

$$c_x \int_{-w}^w (h_B - h_A) = - \int_{-w}^w u_A h_A = \frac{1}{2} (h_{A+}^2 - h_{A-}^2) ,$$

while (3.7.11a) gives

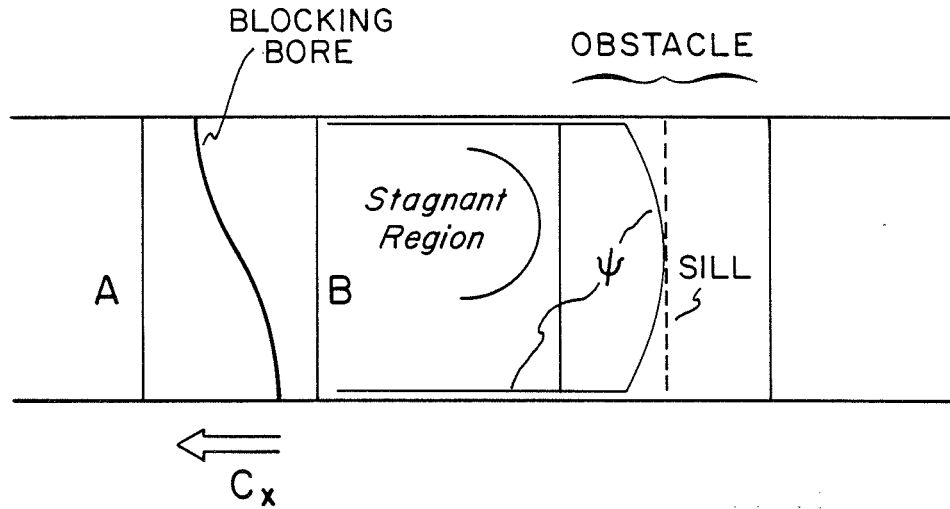


Figure 3.10

Plan view of blocked flow.

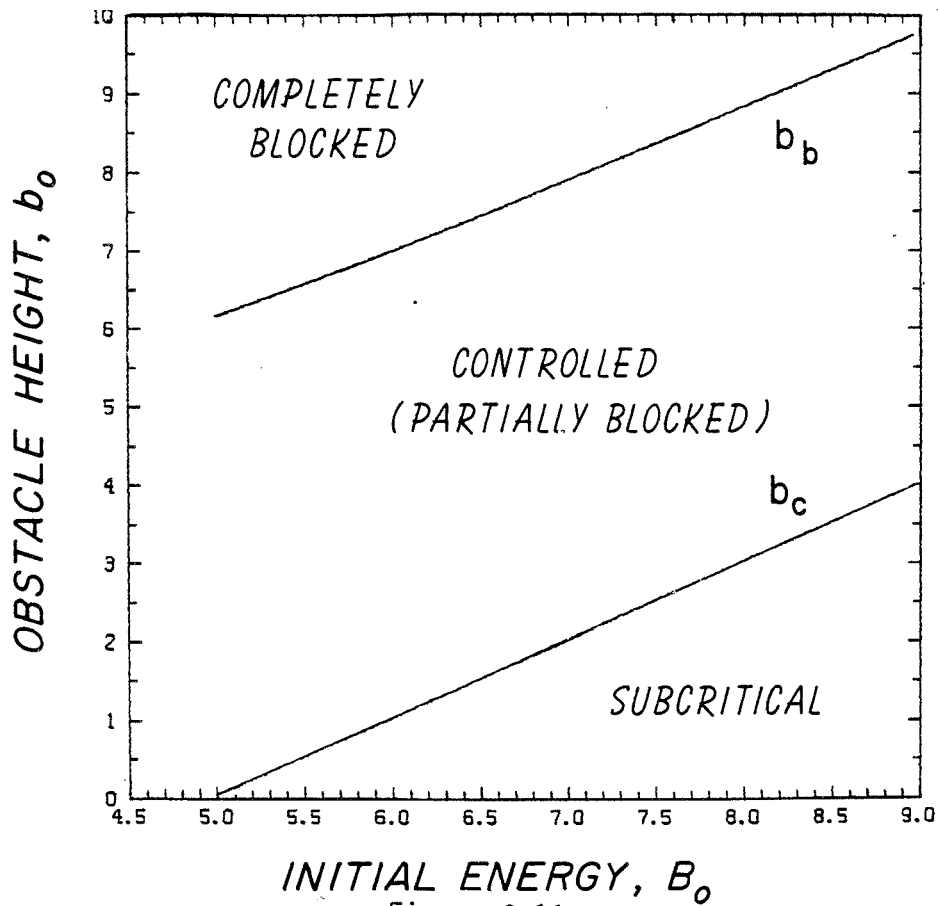


Figure 3.11

Asymptotic states for semigeostrophic adjustment with $Q_0 = 1.$,

$\pi = .2, T = .3.$

$$-c_x(u_{A+}h_{A+} + u_{A-}h_{A-}) = 2u_{B+}^2h_{B+} + h_{B+}^2 - (u_{A+}^2h_{A+} + \frac{h_{A+}^2}{2} + u_{A-}^2h_{A-} - \frac{h_{A-}^2}{2}) .$$

These can be combined to form an equation for h_{B+} in terms of the initial state:

$$h_{B+}^4 + [\phi^{-1}(\frac{1}{2}T^2 - 2) - \bar{h}_A]h_{B+}^3 + [\phi^{-2} - \phi^{-1}(\frac{1}{2}T^2 - 2)\bar{h}_A]h_{B+}^2 - [\frac{1}{2}\phi^{-1}T^2Q_2 - \bar{h}_A]h_{B+} + \frac{1}{2}\phi^{-1}T^2Q_2\bar{h}_A - \frac{1}{2}T^{-1}Q_0Q_1\phi^{1/2} = 0 \quad (3.9.5)$$

where

$$Q_1 = u_{A+}h_{A+} + u_{A-}h_{A-}$$

$$Q_2 = u_{A+}^2h_{A+} + \frac{h_{A+}^2}{2} - u_{A-}^2h_{A-} - \frac{h_{A-}^2}{2} .$$

Once h_{B+} is found from (3.9.5) then b_b is computed from (3.9.3) as

$$b_b = \frac{u_{B+}^2}{2} + h_{B+} = \frac{1}{2}\phi T^2(\phi^{-1} - h_{B+}^2)^2 + h_{B+} .$$

Again, the result will depend on whether the flow is subcritical or supercritical.

Once again, it is worthwhile mentioning the conditions under which this theory is accurate. First, the stagnant region must be in a steady state and no streamline must cross the sill. Second, the bore and its bordering dispersive boundary must have settled into an equilibrium state characterized by a single velocity c_x . Finally, the change in potential vorticity across the bore must be $< 0(\delta)$, as in the solutions of Figure 3.6.

Figure 3.11 shows the behavior of b_c as a function of the initial energy, B_0 . Also shown is a plot of the corresponding values of critical obstacle height, B_c . The qualitative appearance of the figure is the same as that of Figure (2.6) for nonrotating flow.

3.10 Kelvin Wave Reflection From the Obstacle

Numerical investigation into problems associated with time-dependent forcing of semigeostrophic flow prove difficult. This is primarily due to the growth of numerical instabilities over the long computation time that is required. However, one matter which can be dealt with analytically is the reflection of Kelvin waves by the obstacle. We again rely on the semi-steady approximation introduced in section 2.8.

The unsteady fields immediately upstream of the obstacle or contraction are matched to the parametrically unsteady flow over the obstacle or contraction by Equations (3.6.2) and (3.6.1):

$$h_c^4 + h_c^3 \phi^{-1} (T_c^{-2} - 1) = T_c^{-4} Q^2(\epsilon t) \quad (3.10.1)$$

$$\phi T_c^2 (\phi^{-1} - \bar{h}_c)(\phi^{-1} - 2\bar{h}_c) + 3\bar{h}_c = 2(\bar{B}(\epsilon t) - b_c) . \quad (3.10.2)$$

where

$$Q(\epsilon t) = - \bar{h} \delta h \quad (3.10.3)$$

$$2\bar{B}(\epsilon t) = B_+ + B_- = \phi T_c^{-2} \delta h^2 + \phi T_c^2 (\phi^{-1} - \bar{h})^2 + 2\bar{h} , \quad (3.10.4)$$

and the upstream representations of δh , h , and T are used.

Upstream of the obstacle, where the channel is uniform, the flow is partitioned into mean and a time-varying perturbations. The linearized fields are then

$$\bar{h} = H + \bar{h}' = H + A_I e^{ik_I(x - \lambda_I t)} + A_R e^{ik_R(x - \lambda_R t)} , \quad (3.10.5)$$

$$\delta h = \Delta H + \delta h' = \Delta H + B_I e^{ik_I(x - \lambda_I t)} + B_R e^{ik_R(x - \lambda_R t)} , \quad (3.10.6)$$

where I and R denote incident and reflected waves.

The matching conditions (3.10.1) and (3.10.2) are somewhat more complex than their nonrotating counterparts as the critical depth h_c appears explicitly. We therefore set

$$\bar{h}_c = H_c + h'_c(\varepsilon t) \quad (3.10.7)$$

to recognize that the depth at the critical point oscillates about a steady value H_c .

The waves speeds in (3.10.5) and (3.10.6) are given by (3.3.4):

$$\lambda_{I\ R} = -\phi^{1/2} T^{-1} \Delta H \pm H^{1/2} [1 - T^2(1 - \phi H)]^{1/2}, \quad (3.10.8)$$

The amplitudes $A_{I\ R}$ and $B_{I\ R}$ are related through (3.2.15) and (3.2.16) by

$$B_{I\ R} = \pm A_{I\ R} T \phi^{-1/2} H^{1/2} [1 - T^2(1 - \phi H)]^{1/2}. \quad (3.10.9)$$

Substitution of (3.10.5)-(3.10.6) into (3.10.1) then gives

$$H_c^4 + H_c^3 \phi^{-1} (T_c^{-2} - 1) = T_c^{-4} (\bar{H} \Delta H)^2 \quad (3.10.10)$$

to first order and

$$4H_c^3 h'_c + 3H_c^2 \phi^{-1} (T_c^{-2} - 1) h_c = 2T_c^{-4} H \delta H (\delta H \bar{h}' + H \delta h') \quad (3.10.11)$$

to $O(\bar{h}')$.

The same can be done with (3.10.2), the first order result being

$$\phi T_c^2 (\phi^{-1} - H_c) (\phi^{-1} - 2H_c) + 3H_c = \phi T_c^{-2} \delta H^2 + \phi T_c^2 (\pi^{-1} - H)^2 + 2\bar{H} - 2b_c \quad (3.10.12)$$

and, to next order,

$$\phi T_c^2 \bar{h}'_c [4H_c + 3\phi^{-1} (T_c^{-2} - 1)] = 2\phi T_c^2 \delta H \delta h' - 2\phi T_c^2 (\pi^{-1} - H) \bar{h}' + 2\bar{h}'. \quad (3.10.13)$$

Equations (3.10.10) and (3.10.12) relate the basic fields H and ΔH to the geometry at the control T_c and b_c . To evaluate the wave fields we eliminate \bar{h}'_c between (3.10.11) and (3.10.13):

$$\begin{aligned} 2\phi T_c^{-2} \bar{H} \Delta H \bar{H}_c^{-2} (\bar{h}' \delta H + \delta h' \bar{H}) &= 2\phi T^{-2} \delta H \delta h' - 2\phi T^2 (\phi^{-1} - \bar{H}) h' + 2h' \\ &= 2\phi T^{-2} \delta H \delta h' + 2[1 - T^2(1 - \phi \bar{H})]^{1/2} \dots \end{aligned}$$

Substituting for $\delta h'$ and \bar{h}' using (3.10.5), (3.10.6), and (3.10.9) gives

$$k_I \lambda_I = k_R \lambda_R \quad (3.10.14)$$

and

$$\begin{aligned} \phi \bar{H} \delta H T_c^{-2} \bar{H}_c^{-2} \left\{ \Delta H (A_I + A_R) + \bar{H}^{1/2} T \phi^{-1/2} [1 - T^2(1 - \phi \bar{H})]^{1/2} (-A_I + A_R) \right\} \\ = \phi^{1/2} T^{-1} \bar{H}^{-1/2} [1 - T^2(1 - \phi \bar{H})]^{1/2} \left\{ \delta H (-A_I + A_R) \right. \\ \left. + \phi^{-1/2} T \bar{H}^{1/2} [1 - T^2(1 - \phi \bar{H})]^{1/2} (A_I + A_R) \right\} \quad (3.10.15) \end{aligned}$$

This expression can be simplified if it is noted that (3.10.10) can be rewritten as

$$\phi \bar{H} \delta H T_c^{-2} \bar{H}_c^{-2} = \phi^{1/2} T_c^{-1} \bar{H}_c^{-1/2} [1 - T^2(1 - \phi \bar{H}_c)]^{1/2} .$$

Equation (3.10.15) then becomes

$$\begin{aligned} \left\{ \frac{\bar{H} T_c [1 - T_c^2 (1 - \phi \bar{H}_c)]}{\bar{H}_c T [1 - T^2 (1 - \phi \bar{H}_c)]} \right\} \frac{1}{2} \left\{ -\phi^{1/2} T^{-1} \bar{H}^{-1/2} \delta H [1 - T^2(1 - \phi \bar{H}_c)]^{-1/2} (A_I + A_R) + (A_I - A_R) \right\} \\ = \phi^{1/2} T^{-1} \bar{H}^{-1/2} \delta H [1 - T^2(1 - \phi \bar{H}_c)]^{-1/2} (-A_I + A_R) - (A_I + A_R) \quad (3.10.15) \end{aligned}$$

The notation can be further simplified by introducing the Froude number of the upstream flow

$$F = \frac{\bar{u}}{\lambda_I^{-1} \bar{u}} = \phi^{1/2} T^{-1} \bar{H}^{-1/2} \delta H [1 - T^2(1 - \phi \bar{H})]^{-1/2} \quad (3.10.16)$$

and the quantity

$$G = \left\{ \frac{RT_c [1 - T_c^2 (1 - \phi R_c)]}{R_c T [1 - T^2 (1 - \phi R_c)]} \right\}^{\frac{1}{2}}$$

Equation (3.10.15) can then be written as

$$C_r = \frac{A_R}{A_I} = \left(\frac{F + 1}{F - 1} \right) \left(\frac{1 - G}{1 + G} \right) \quad (3.10.17)$$

There are a number of ways of displaying the information contained in (3.10.17). To make comparison with the results for the nonrotating case (Figure 2.11) we first study C_r as a function of h/b_c using a channel with no width contractions. This information has been plotted in Figure 3.12 for various potential vorticities. The most striking change that rotation induces is that C_r can have arbitrarily low values, whereas the lowest value of C_r in Figure 2.11 is 1/3. This behavior is particularly evident for large values of ϕ . Apparently the obstacle is a less effective reflector of wave energy, and the sheltering effect spoken of in Chapter 2 is lessened as ϕ grows.

To understand this result we must first understand the differences between the basic flows upon which the waves propagate. In the nonrotating case the basic flow energy is partitioned between potential, $h + b$, and kinetic, $u^2/2$. Upstream of the obstacle, the greater part of this energy is potential. However, the constraints imposed by (2.1.5) demand that this potential energy be sacrificed in favor of kinetic energy as the fluid passes over the obstacle. It can do so only by decreasing its depth, and this constricting effect accounts in part for the wave reflection. If the Froude number of the upstream flow is very

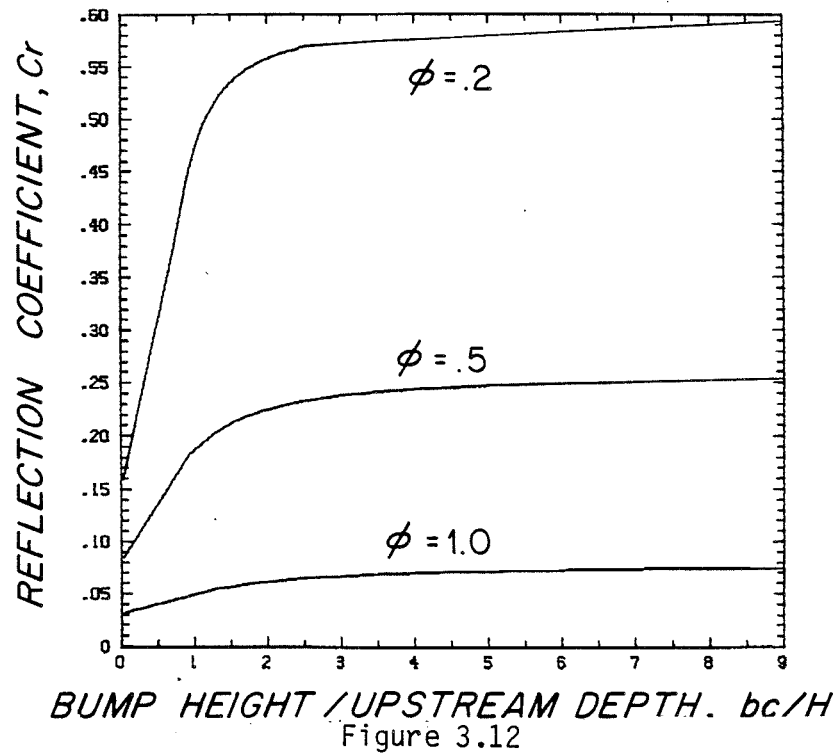


Figure 3.12

Reflection coefficients for channel with isolated obstacle and width, $w = 2.45$. The mean flow rate is $Q = 1$.

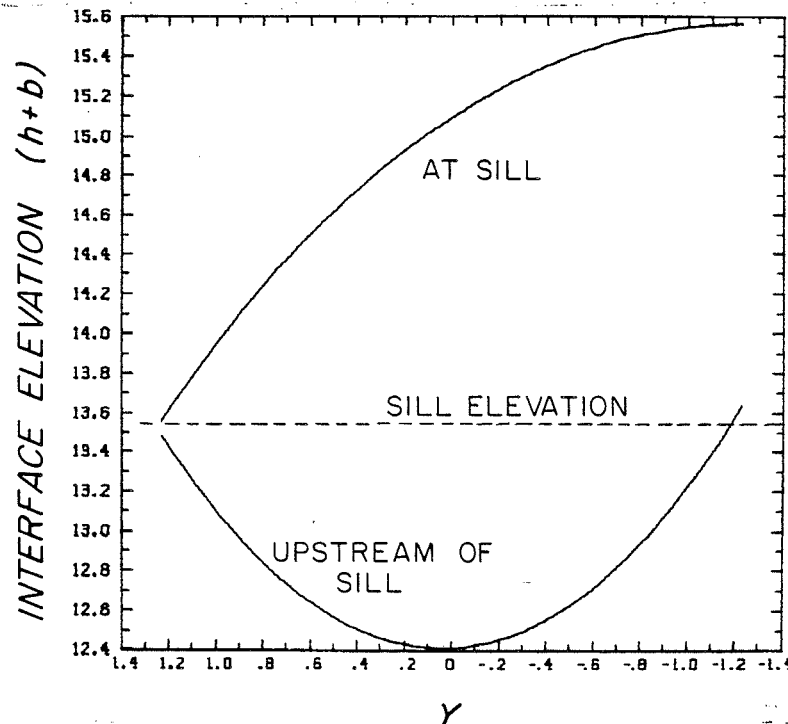


Figure 3.13

Cross-sectional interface profiles for controlled flow over obstacle with $b_c/H = 1$. The flow parameters are the same as those of the upper ($\phi = 0.2$) curve in Figure 3.12.

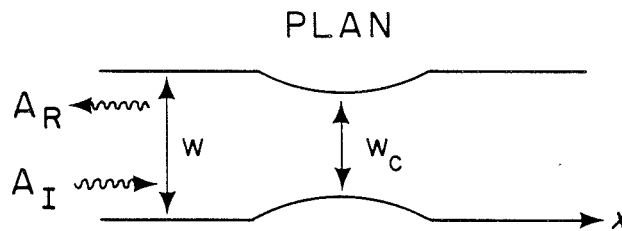
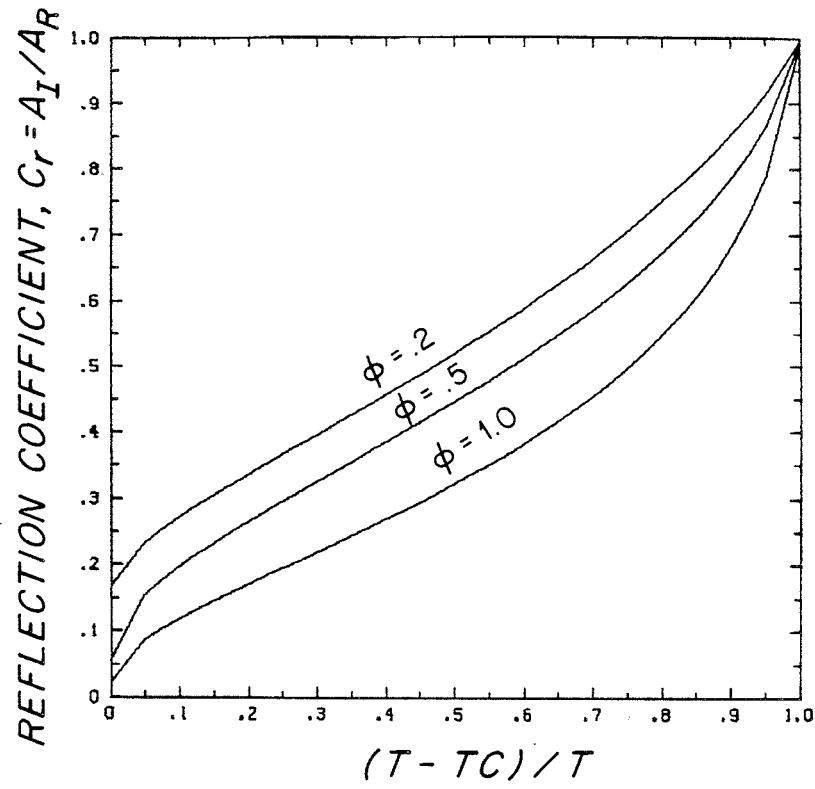


Figure 3.14

Reflection coefficient for channel containing width contraction.

$$T = \tanh(\phi^{1/2}w(x)), \quad Q = 1, \quad b = 0.$$

small, then a huge change in depth is necessary to generate the required kinetic energy to satisfy the critical condition, implying a high wave reflection coefficient.

The rotating case is quite different. It is no longer true that the upstream state is dominated by potential energy. This is implied by Equation (3.2.11):

$$\delta u = \phi^{1/2} T(\phi^{-1} - \bar{h})$$

which stipulates a balance between velocity and depth for upstream flows of any depth. The basis for this result is the boundary layer effect, which concentrates the mass flux in streams of width $\phi^{-1/2}$ along each wall.

Figure 3.13 shows cross sections of surface elevation at and upstream of the sill for a controlled flow with $Q = 1$ and $b_c = 13.56$. At the upstream section, the Froude number (based on 3.10.16) is tiny;

$$\frac{\bar{u}}{\lambda_I - \bar{u}} = .01 .$$

However, boundary layers are present on either wall and the local Froude number at $y = -w$ is much higher;

$$u_- / h_-^{1/2} = .89 .$$

The fluid along the right-hand boundary (where the incident Kelvin wave propagates) has high kinetic energy and can surmount the obstacle with a 'running start'. The result can be seen in the surface elevation at the sill, which is actually greater than that upstream. The constricting effect is therefore decreased, as is the reflection coefficient.

The results for a channel containing side contractions but no bottom topography is shown in Figure 3.14. The reflection coefficients are

plotted for various potential vorticities as functions of the relative contraction $(T - T_c)/T$. Again, the boundary layer influence causes less wave energy to be reflected for large potential vorticity. Unlike the previous case, however, the fluid is constrained on two sides, rather than one, and complete reflection is realized as the channel width goes to zero (i.e., as $(T - T_c)/T \rightarrow 1$).

3.11 Self-excited Oscillations

The oscillatory flow treated in the previous section was set up by periodic forcing away from the obstacle. There also exist situations in which the oscillations are produced in the vicinity of the obstacle as a result of a destabilization due to topography. Consider a steady solution containing a double bifurcation (e.g., Figure 3.4). Which choice of branches gives a stable solution? Intuitively, we might start upstream on the upper (subcritical) branch and proceed through the first bifurcation onto the supercritical branch. As the second bifurcation is approached, however, the flow becomes unstable according to the geometry of the characteristics. A quick inspection of other choices of branches reveals that they too are unstable.

Under these conditions we might expect a hydraulic jump to form between the two bifurcations. However the fluid downstream of the jump would not have sufficient energy to flow steadily through the second bifurcation. It appears that no stable, steady, controlled solution exists.

Further investigation through the use of the numerical model is difficult owing to numerical instabilities. However, it is possible to

model a similar nonrotating flow using the more stable one-dimensional Lax-Wendroff method (see Appendix A).

Consider the double-silled obstacle shown in Figure 3.15. Steady, transitional solutions for flow over the obstacle will display the same sort of dual bifurcation discussed above. What solution results from the sudden obstruction of such an obstacle into an initially uniform flow

Figure 3.15 shows the adjustment that results from the experiment suggested above. The obstacle is grown to a height b_0 such that $b_c < b_0 < b_b$. Part 'a' shows the initial adjustment that takes place including a bore which propagates upstream away from the obstacle. The surface configuration left behind contains a small jump in the lee of the downstream sill. This configuration is not a steady solution, however, and another upstream-propagating bore is formed along with a packet of waves with positive phase speed (Figure 3.15b). After these transients move away from the obstacle, a new, larger hydraulic jump is formed in the lee of the downstream sill (Figure 3.15c). However, this configuration is unstable as before and events repeat themselves on a time scale that is much longer (by a factor of 10 or 15) than the time scale of initial adjustment.

It should be mentioned that destabilizing geometries, such as the one shown in Figures 3.4 and 3.15, are the exception rather than the rule. The topography must be fine tuned to produce two bifurcations.

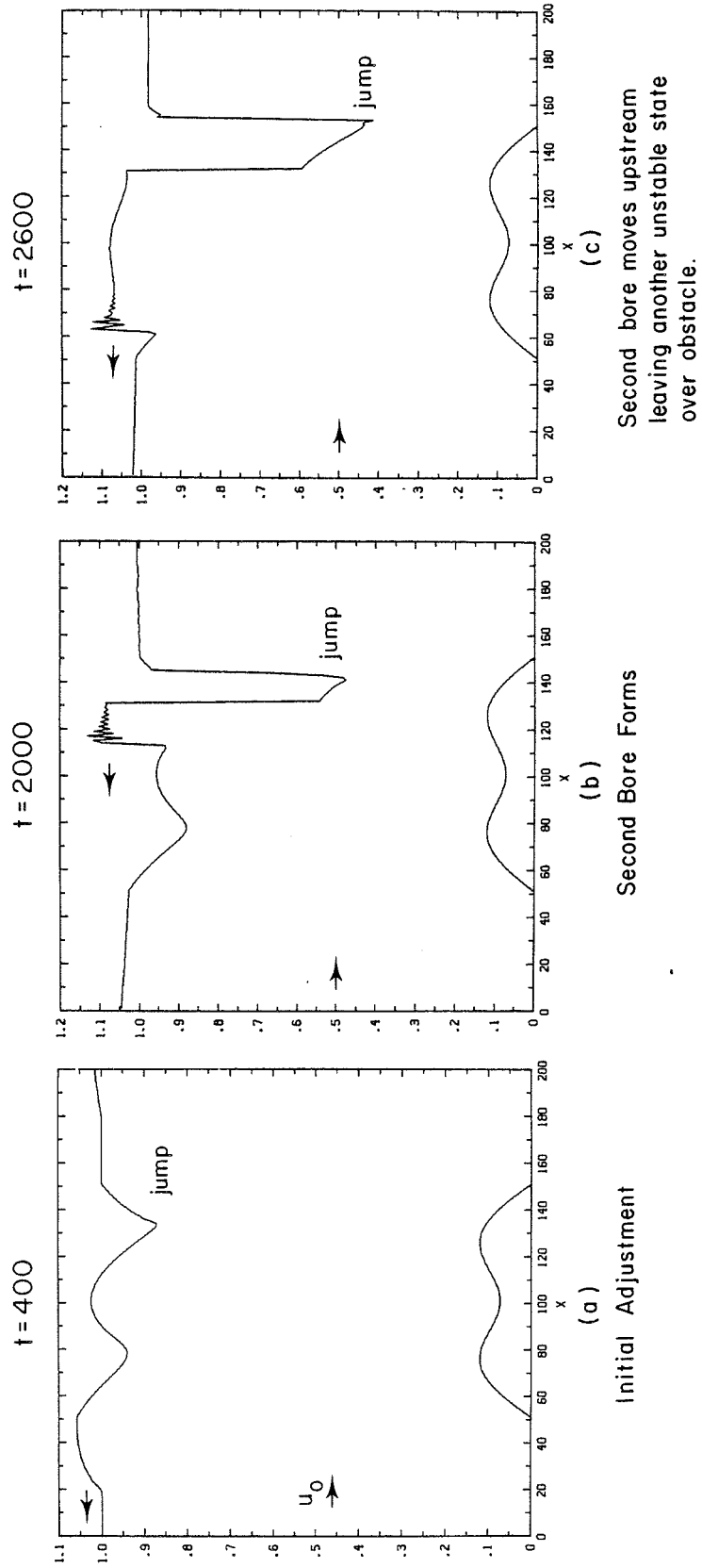


Figure 3.15

Nonrotating adjustment to obstacle with double sill. $b_0 = .13$, $Q_0 = .6$, $B_0 = 1.18$.

Chapter 4 Rotating Hydraulics and Dispersive Waves

4.1 Introduction

The semigeostrophic, constant potential vorticity solutions of the last chapter bear great similarity to the one-dimensional solutions discussed in Chapter 2. In particular, the adjustment that results from a sudden change in topography is in both cases accomplished by two non-dispersive waves, one moving upstream and the other downstream relative to the flow. If the topography has a certain minimum height, b_c , then a critical condition is created at the sill with respect to the upstream-propagating wave and the flow far away is permanently affected by the change in topography. The critical condition causes the sill to act as a source of information for the far field (see Figure 2.3c). If on the other hand the sill height is less than b_c , the only fields permanently affected are those immediately above the perturbed topography.

It was shown in section 3.3 that the semigeostrophic limit ($\delta \gg 0$) allows only nondispersive (Kelvin) modes. Suppose that the channel has an $O(1)$ horizontal aspect ratio and that the flow consists of a uniform stream with velocity U and depth H . In addition to the Kelvin mode the stream now supports linear Poincare waves with (dimensionless) frequency

$$\omega = Uk \pm \left[1 + \left(k^2 + \frac{n^2 \pi^2}{4 w^2} \right) H \right]^{1/2+} \quad (n = 1, 2, 3, \dots)$$

(using the notation of the previous chapter). What are the hydraulic properties of this dispersive flow? In particular, what role do the

⁺ c.f. Equation (4.2.18).

Poincare modes play in the adjustment that would result from the obstruction of an obstacle? Is it necessary to grow an obstacle to a certain minimum height before upstream influence occurs, or does an arbitrarily small obstacle cause an upstream response? Also, what is the nature of this response -- does it decay away from the obstacle or is it felt infinitely far away? Finally, is there any difference between the upstream influence and the downstream influence?

At this point we might seek a further clarification of the affects of dispersion using the characteristic tools developed earlier. However, the characteristic formulation of problems with two spatial dimensions is more complicated and considerably less useful than the one-dimensional formulation (see Whitham, 1974, section 5.9). Wave fronts now propagate along characteristic surfaces whose geometry depends on the initial orientation of the front. Since a continuum of fronts is generated by an initial disturbance, it is no longer practical to integrate along characteristics to obtain solutions. Thus, it becomes difficult to make statements about the upstream influence of obstructions. The numerical model is also of limited use in this problem because of the large expense involved in resolving two dimensions with $\delta = O(1)$ and, more importantly, because the stability problems associated with the Lax-Wendroff scheme seem to worsen as the channel width is increased.

Because of these difficulties, we attempt to clarify the dispersive adjustment process by seeking analytic solutions to a linearized version of the adjustment problem discussed in Chapters 1 and 2. In this problem we consider the obstruction of an obstacle into a channel flow characterized

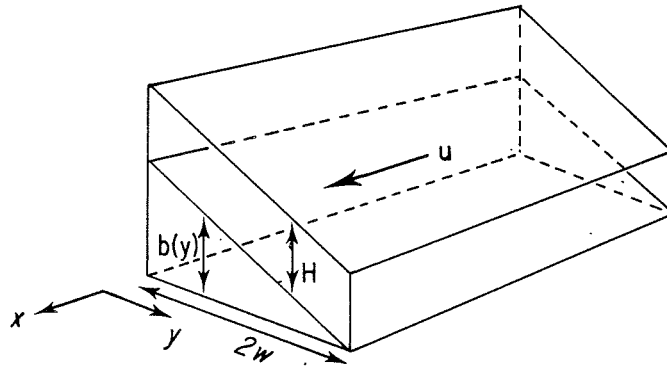
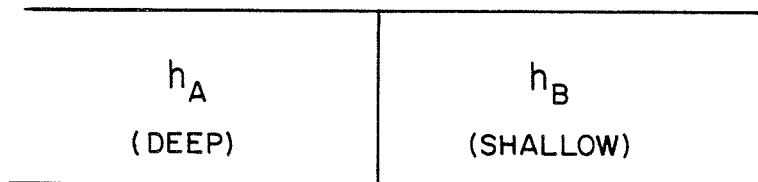


Figure 4.1

Definition sketch showing initial uniform flow over sloping bottom.

(a) Plan view of initial state



(b) Final steady state

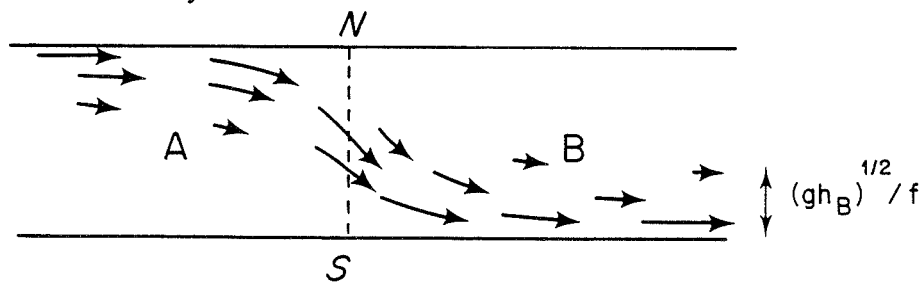


Figure 4.2

Simplified sketch of Gill's (1976) solution of a dam-break problem. The boundary layer flow crosses the channel at the original position of the discontinuity.

by $\delta = O(1)$. The solutions are obtained from time-dependent equations which have been linearized about the height of the obstacle. This approach runs contrary to our earlier observation that linear models are inherently unsatisfactory in describing hydraulic control. In the steady solutions of Figures 2.2 and 3.2 the controlled solution is associated with a bifurcation (point ③ in Figure 2.2). This bifurcation is a consequence of the nonlinearity of the governing polynomial. Away from the bifurcation, however, there is no reason that a linear model might reproduce the basic physics of the solutions. We therefore proceed in anticipation of studying steady solutions which correspond in some way with the subcritical or supercritical nondispersive solution studied earlier.

4.2 Adjustment in a wide rotating channel

Consider a channel with uniformly sloping bottom and width $2w$ (Figure 4.1). The channel contains a steady two-layer flow with interface slope identical to the bottom slope. The upper layer is again inactive and the (dimensional) velocity in the lower layer is

$$U = -\frac{g}{f} \frac{db}{dy} = \text{constant}$$

and

$$H = \text{constant}.$$

Now consider perturbations Uu' , Uv' , and $H\eta$ of this uniform state that result from the obstruction of an obstacle of height $b(y) + Hb'(x,y)$. The velocity and height fields are written as

$$u = U [1 + u' (x,y,t)]$$

$$v = U$$

$$n = H [1 + \eta (x,y,t)].$$

Substituting these expressions into the shallow-water equations and linearizing about u' and η we obtain

$$\frac{d_0}{dt'} u' - Fv' = - \frac{1}{F_d} (\eta_{x'} + b'_{x'}) \quad (4.2.1)$$

$$\frac{d_0}{dt'} v' + Fu' = - \frac{1}{F_d} (\eta_{y'} + b'_{y'}) \quad (4.2.2)$$

$$\frac{1}{F_d} \frac{d_0 \eta}{dt'} + u'_{x'} + v'_{y'} = 0 \quad (4.2.3)$$

where

$$F = wf/(gH)^{1/2} = w/(\text{Rossby Radius}) ,$$

$$\frac{d_0}{dt} = \frac{\partial}{\partial t'} + F_d \frac{\partial}{\partial x'} \quad [F_d = U/(gH)^{1/2} = \text{initial Froude number}],$$

$$t' = t (gH)^{1/2}/L ,$$

$$x' = x/w ,$$

and

$$y' = y/w .$$

The notation in (4.2.1) - (4.2.3) is now simplified by replacing η/F_0 and b'/F_d by η and b and dropping primes. The result is

$$\frac{d_0}{dt} u - Fv = - \eta_x - b_x \quad (4.2.4)$$

$$\frac{d_0}{dt} v + Fu = - \eta_y - b_y \quad (4.2.5)$$

$$\frac{d_0 \eta}{dt} + u_x + v_y = 0 \quad (4.2.6)$$

The linearized potential vorticity equation can be obtained by taking the curl of (4.2.4) and (4.2.5) and adding the result to (4.2.6). The result,

$$\frac{d_0}{dt} (u_y - v_x + F\eta) = 0 ,$$

implies that*

$$u_y - v_x + F\eta = \phi (x - F_d t) . \quad (4.2.7)$$

We assume that the obstacle is grown quickly but continuously, so that the fluid interface initially bulges with the same shape as the obstacle and no velocity perturbations are initially present. The initial conditions are therefore

$$\eta(x,y,0) = u(x,y,0) = v(x,y,0) = 0 ,$$

from which follows

$$\phi(x - F_d t) = 0 .$$

Before proceeding further, it is worthwhile recognizing the status of the problem under consideration in relation to the string of geostrophic adjustment problems that have been solved since the pioneering work of Rossby (1936). This subject has been reviewed by Blumen (1972). We note that the present problem differs from the archetypical geostrophic adjustment problem in two respects. First, the solution will not adjust

* Equation (4.2.7) implies that an initial disturbance in the potential vorticity is advected away from the obstacle and plays no role in determining the asymptotic state over the obstacle. However, we will have no occasion to use this fact as ϕ is zero everywhere for our initial conditions.

to a geostrophically balanced state unless $v = 0$, as indicated by Equations (4.2.4) and (4.2.5). (More typically, the advective terms are absent and a final steady state will be geostrophic.) Second, the domain of solution is bounded by solid, vertical walls. The only progress made on the latter complication has been by Gill (1976) who found linear solutions to a dam-break channel flow problem in which the initial state is stagnant but contains a discontinuity in the free surface.

A simplified drawing of Gill's solution is shown in Figure 4.2. The initial discontinuity in the free surface lies perpendicular to the axis of the uniform, infinite channel (Figure 4.2a) at $x = 0$. The initial potential vorticity is higher to the right of the discontinuity than to the left, owing to the greater depth on the left. Since Gill's linear solution conserves potential vorticity pointwise, the discontinuity in potential vorticity remains fixed at $x = 0$ throughout the adjustment, despite the fact that the depth and velocity fields become continuous there.

The initial distribution of potential vorticity is responsible for determining the character of the final steady state (shown in Figure 4.2b). After the 'dam break' there is a flow of fluid from left to right due to the pressure gradient associated with the discontinuity in depth. Thus, Region B experiences a general increase in depth while Region A experiences an decrease in depth. The fluid flows from Region A into B in boundary layers with Rossby deformation scale thickness. In Region A the relative vorticity must decrease to accommodate the decrease in depth, implying that the flow must lie along the north boundary (for northern hemisphere rotation). In Region B the depth increases and the boundary layer must lie along the south wall.

Because of the boundary layer locations imposed by the pointwise conservation of initial potential vorticity, there must exist a southward cross flow in the final steady state (Figure 4.2b). The position of this cross flow is the same as that of the initial discontinuity in depth. Fluid parcels in the cross flow change their potential vorticity upon passing the line $x = 0$. It is difficult to see whether or not the cross flow would exist if the fluid parcels conserved their potential vorticity. We note that this difficulty is avoided in our adjustment problem since the potential vorticity is everywhere uniform. We will be curious to see whether or not the obstacle can induce a cross stream flow similar to Gills.

An equation for v alone can be obtained by taking the x -derivative of (4.2.7) (with $\phi = 0$) and applying (4.2.4) and (4.2.6):

$$\begin{aligned} -v_{xx} &= -u_{xy} - F\eta_x \\ &= v_{yy} + \frac{d_0}{dt} \eta_y + F \left(\frac{d_0 u}{dt} - Fv + b_x \right) \end{aligned}$$

Equation (4.2.5) can now be used to substitute for the terms containing η and u , the result being

$$v_{xx} + v_{yy} = \frac{d_0^2 v}{dt^2} + \frac{d_0}{dt} b_y + F^2 v - F b_x,$$

or

$$\frac{d_0^2}{dt^2} v - \nabla^2 v + F^2 v = F b_x - F_0 b_{xy}. \quad (4.2.8)$$

A similar procedure can be used to obtain the following equation for η :

$$\frac{d_0^2}{dt^2} \eta - \nabla^2 \eta + F^2 \eta = \nabla^2 b \quad (4.2.9)$$

First consider steady solutions to (4.2.8) and (4.2.9). If the channel width is much smaller than the Rossby radius ($F \ll 1$) then the steady version of (4.2.9) simplifies to

$$(F_d^2 - 1) \eta_{xx} - \eta_{yy} = -\nabla^2 b. \quad (4.2.10)$$

If the obstacle is one-dimensional, so that no y -dependent modes are synthesized in the initial disturbance, then steady solutions will depend only on x . Integration of (4.2.10) then yields

$$\eta = \frac{1}{(F_d^2 - 1)} b \quad (4.2.10a)$$

This equation simply gives the linear version of the non-controlled solutions found in Chapter 2. The surface (or interface) elevation is

$$H + \eta + b = \frac{F_d^2}{(F_d^2 - 1)} b + H.$$

As before the surface rises/dips over the obstacle for supercritical/subcritical flow. As $F_d > 1$, this deformation grows without bound and the linear approximation becomes inadequate for finite b .

If the topography is two-dimensional, solutions to (4.2.10) again depend upon the value of F_d relative to unity. If $F_d^2 < 1$, then (4.2.10) is elliptic and a cross-channel mode will have exponential behavior in x . This suggests a decaying response away from the obstacle. If $F_d^2 > 1$ then (4.2.10) is hyperbolic and the solution can be obtained by integration along characteristics X_{\pm} , where

$$\frac{d X_{\pm}}{dy} = \pm (F_d^2 - 1)^{1/2}.$$

These characteristics reflect off of the channel walls in a periodic manner and it is readily verifiable that the solutions away from the obstacle are periodic in the y -direction. Finally, (4.2.10) becomes parabolic for $F_d = 1$. In this case integration of (4.2.10) across the channel gives

$$\frac{\partial \eta_-}{\partial y} - \frac{\partial \eta_+}{\partial y} = \int_{-w}^{+w} \nabla^2 b \, dy .$$

Since (by 4.2.5) $\partial \eta_{\pm} / \partial y = - \partial b_{\pm} / \partial y$, the above equation implies that

$$\frac{\partial^2}{\partial x^2} \int_{-w}^{+w} b \, dy = 0$$

which, for isolated topography leads to $b = 0$. No solution to the parabolic equation exists unless the obstacle causes no net change in bottom elevation.

If $F = 0(1)$, the classification of (4.2.8) or (4.2.9) with respect to F_d remains unchanged and solutions can be expected to maintain the general behavior outlined above. We now compute a specific solution with $F = 1$. Because of the anisotropy that rotation introduces, it is no longer necessary to use y -dependent topography to synthesize y -dependent modes. We therefore choose an obstacle with elevation

$$b = \begin{cases} 0 & (|x| > \pi) \\ 1 + \cos x & (|x| \leq \pi) \end{cases} \quad (4.2.11)$$

Because of the boundary conditions,

$$v(x, \pm 1, t) = v_{\pm} = 0$$

it is easiest to work with Equation (4.2.8). However, the Kelvin mode is characterized by $v = 0$ and will have to be added later. In view of the above boundary condition, we express the solution as a cosine series:

$$v = \sum_{n=0}^{\infty} \tilde{v}_n(x, t) \cos \left[\frac{(2n+1)}{2} \pi y \right] \quad (4.2.12)$$

Multiplication of Equation (4.2.8) (with $F = 1$ and $\partial b / \partial y = 0$) by $\cos \left[\frac{(2n+1)}{2} \pi y \right]$ and integration of the result across the channel yields

$$\frac{d_0^2}{dt^2} \tilde{v}_n - \frac{\partial^2 \tilde{v}_n}{\partial x^2} - \int_{-1}^1 dy \cos \left[\frac{(2n+1)}{2} \pi y \right] v_{yy} + \tilde{v} =$$

$$\frac{d_0^2}{dt^2} \tilde{v}_n - \frac{\partial^2 \tilde{v}_n}{\partial x^2} + \gamma_n^2 \tilde{v}_n = a_n \frac{db}{dx} \quad (4.2.13)$$

where

$$\gamma_n^2 = \left[\frac{(2n+1)}{2} \pi \right]^2 + 1$$

and

$$a_n = \frac{4 (-1)^n}{\pi (2n+1)}$$

is the coefficient in the Fourier Series

$$\sum_{n=0}^{\infty} a_n \cos \left[\frac{(2n+1)}{2} \pi y \right] = \begin{cases} 1 & (|y| > 1) \\ 0 & (|y| = 1) \end{cases} .$$

We will express the solution to (4.2.13) as the sum of particular and homogeneous parts:

$$\tilde{v}_n = H_n(x, t) + P_n(x) .$$

Since the nonhomogeneous term in (4.2.13) is an odd function of x , we write $P_n(x)$ as a Fourier sine integral:

$$P_n(x) = \int_0^{\infty} A_n(k) \sin(kx) dk . \quad (4.2.14)$$

It can readily be verified upon substitution that the Fourier coefficient is

$$A_n(k) = \frac{2a_n}{\pi [1_n^2 + k^2 \lambda^2]} \int_0^\infty \frac{db}{dx'} \sin(x'k) dx'$$

where $\lambda^2 = 1 - F_d^2$.

For the topography given by (4.2.11) this integral can be evaluated in closed form:

$$\begin{aligned} 2 \int_0^\infty \frac{db}{dx'} \sin(x't) dx' &= \frac{\sin[(1-k)\pi]}{1-k} - \frac{\sin[(1+k)\pi]}{1+k} \\ &= \frac{-\cos \pi \sin \pi k}{1-k} - \frac{\cos \pi \sin \pi k}{1+k} \\ &= \left(\frac{1}{1-k} + \frac{1}{1+k} \right) \sin \pi k = \frac{2 \sin \pi k}{(1-k^2)}, \end{aligned}$$

and the Fourier coefficient is therefore

$$A_n(k) = \frac{2a_n \sin \pi k}{\pi (1_n^2 + k^2 \lambda^2)(1-k^2)}. \quad (4.2.15)$$

The transient (homogeneous) solution $H_n(x,t)$ will be expressed as a Fourier integral of Poincaré waves. The initial condition $v(x,y,0) = \tilde{v}_n(x,0) = 0$, implies that

$$H_n(x,0) = -P_n(x). \quad (4.2.16)$$

In view of this condition and the form of the particular solution, we write

$$H_n(x,t) = \int_{-\infty}^{\infty} B_n(k) \sin[nx - \omega_{\pm}(k)t] dk \quad (4.2.17)$$

The frequency $\omega_{\pm}(k)$ is constrained by (4.2.13) to obey the dispersion relation

$$\omega_{\pm}(k) = F_d k \pm (k^2 + 1_n^2)^{1/2}, \quad (4.2.18)$$

which is just a renormalized version of (4.1.1).

The Poincaré waves will therefore occur in pairs, each member identified by the '+' or '-' sign in (4.2.18). Thus

$$\begin{aligned} H_n(x,t) &= \int_{-\infty}^{\infty} B_n(k) \{ \sin [kx - (F_d k + (n^2 + 1_n^2)^{1/2}) t] \\ &\quad + \sin [kx - (F_d k - (n^2 + 1_n^2)^{1/2}) t] \} dk \\ &= \int_{-\infty}^{\infty} B_n(k) \sin(kx - F_d k t) \cos [(k^2 + 1_n^2)^{1/2} t] dk . \end{aligned}$$

Combining this expression with the particular solution (4.2.14) gives

$$\tilde{v}_n(x,t) = \int_{-\infty}^{\infty} \{ A_n(k) \sin nx + B_n(k) \sin(kx - F_d kt) \cos [(k^2 + 1_n^2)^{1/2} t] \} dk$$

and application of the initial condition (4.2.16) leads to

$$A_n = - B_n ,$$

so that the solution simplifies to

$$\begin{aligned} \tilde{v}_n(x,t) &= \int_{-\infty}^{\infty} A_n(k) \{ \sin kx - \sin(kx - F_d kt) \cos [(k^2 + 1_n^2)^{1/2} t] \} dk . \\ &= \frac{2 a_n}{\pi} \int_{-\infty}^{\infty} \frac{\sin \pi k}{(1_n^2 + \lambda^2 k^2)(1 - k^2)} [\sin kx - \sin(kx - F_d kt)] \\ &\quad \cdot \cos [(k^2 + 1_n^2)^{1/2} t] dk . \quad (4.2.19) \end{aligned}$$

The behavior of this integral depends crucially on the singularities due to expression $(1_n^2 + \lambda^2 k^2)(1 - k^2)$. The apparent singularity $k = 1$ is actually removable, as $\sin \pi k \rightarrow 0$ for $k \rightarrow 1$. However, a singularity does exist at $k^2 = -1_n^2/\lambda^2$. If the initial flow is characterized by $F_d^2 > 1$ then $\lambda = (1 - F_d^2)^{1/2}$ is imaginary, k is real, and

$$\omega_- = F_d k - (k^2 + 1_n^2)^{1/2} = 0.$$

The singularity thus occurs when the flow is critical with respect to phase speed. On the other hand, $F_d^2 < 1$ implies that the singularity will occur at imaginary k .

First consider the steady part of the integral in (4.2.19). It is convenient to rewrite this as follows:

$$p_n(x) = \frac{2 a_n}{\pi} \int_{-\infty}^{\infty} \frac{\sin(\pi k) \sin(kx) dk}{(1_n^2 + \lambda^2 k^2)(1 - k^2)} = \frac{2 a_n}{\pi (1_n^2 + \lambda^2)} \cdot \int_{-\infty}^{\infty} \left[\frac{\sin \pi k \sin kx}{1 - k^2} + \frac{\sin \pi k \sin kx}{(1_n^2/\lambda^2) + k^2} \right] dk.$$

These integrals can be evaluated using residues or simply by looking them up in the tables of Gradshteyn and Ryzhik (1965). For $\lambda^2 = 1 - F_d^2 > 0$, the solution is

$$p_n(x) = \frac{a_n \lambda}{2(1_n^2 - \lambda^2) 1_n} \left[e^{-|\pi+x| 1_n/\lambda} - e^{-|\pi-x| 1_n/\lambda} - \frac{2 1_n}{\lambda} \cdot \begin{cases} 0 & |x| > \pi \\ \sin(x) & |x| \leq \pi \end{cases} \right] \quad (4.2.20)$$

For $\lambda^2 = 1 - F_d^2 < 0$, the solution is

$$p_n(x) = \begin{cases} 0 & (x < -\pi) \\ \frac{-a_n}{\lambda^2 + 1_n^2} \left[\sin x + \frac{\lambda}{1_n} \sin \frac{1_n}{\lambda} (x+\pi) \right] & (|x| \leq \pi) \\ \frac{-2 a_n \lambda}{1_n (\lambda^2 + 1_n^2)} \sin \left(\frac{1_n}{\lambda} \pi \right) \cos \left(\frac{1_n}{\lambda} x \right) & (x \geq \pi) \end{cases} \quad (4.2.21)$$

If $\lambda^2 = -1_n^2$, then the dispersion relation for a Poincare wave propagating upstream relative to the flow becomes

$$\omega_- = F_d k - (k^2 - \lambda^2)^{1/2} = F_d k - (k^2 - 1 + F_d^2)^{1/2}.$$

In particular, if the phase speed is zero ($\omega_- = 0$) then $k = 1$ and the wave has the same length as the topography. Thus $\lambda = 1_n$ implies that a wave whose phase is frozen can resonate with the topography, as indicated by the presence of $(\lambda^2 - 1_n^2)^{-1}$ in the above solution. The resonant ($\lambda = 1_n$) version of (4.2.21) is

$$p_n(x) = \begin{cases} 0 & (x < -\pi) \\ \frac{a_n}{1_n^2} [x \cos x - \sin(x+\pi) - \pi \cos(x+\pi)] & (|x| \leq \pi) \\ -\frac{2 a_n}{1_n^2} [\sin(x-\pi) + \pi \cos(x-\pi)] & (x > \pi) \end{cases} \quad (4.2.21a)$$

$(\lambda^2 = 1_n^2 < 0)$

Figure 4.3 contains some sample steady solutions for the three cases: $\lambda > 0$, $\lambda = 0$, and $\lambda < 0$ which correspond to $F_d < 1$, $F_d = 1$, and $F_d > 1$ respectively. These results are compared to Figure 4.4 which shows some semigeostrophic solutions in the corresponding parameter range. If $F_d < 1$, the initial flow is subcritical with respect to the Kelvin mode and the solution decays away from the obstacle in either direction (Figure 4.3a). According to (4.2.20), the length of this decay is $\lambda/1_n$. Therefore the decay scale varies from a value of $1/1_n$ for highly subcritical⁺ flows to zero for nearly critical flows. Upstream influence is felt, but within at most a few obstacle lengths of the topography.

⁺ Unless indicated otherwise the terms subcritical, supercritical and critical are used in connection with the Kelvin wave speed.

If $F_d = 1$, the initial flow is critical with respect to the Kelvin mode and the Fourier integral (4.2.19) blows up, as expected. If $F_d > 1$, the initial flow is supercritical and the steady solutions contain lee waves (Figure 4.3b). According to (4.2.21) these waves have length $2\pi \lambda / l_n$ and are phase frozen in the supercritical flow. They resonate with the obstacle if $\lambda = l_n$ and will grow linearly with distance over a series of obstacles of comparable length. They depend on the ability to align their crests obliquely to the channel axis so as to achieve zero phase velocity in the supercritical flow.

The unsteady part of (4.2.19) is more difficult to evaluate in closed form. However, some progress can be made by inspection of its asymptotic properties for large time. Using the standard arguments of stationary phase (Copson, 1965), we note that as $t \rightarrow \infty$ the major contribution to the integral at points x and t will arise from wave numbers k_s which satisfy

$$x/t = C_g = \omega'(k_s) = F_d - k_s (k_s^2 + l_n^2)^{-1/2}.$$

For points close to the obstacle, x/t is tiny and wave numbers k_s which contribute most will be those for which $C_g(k_s)$ is nearly zero. The Poincaré modes with near zero group velocity can therefore be expected to play a major role in the establishment of the decaying region which flanks the obstacle when $F_d < 1$. (If $F_d > 1$ then $C_g > 0$ for all k_s , and such behavior is not possible.)

The stationary phase approximation to (4.2.19) decays like $[\omega''(k_s) t]^{-1/2}$ as $t \rightarrow \infty$.⁺ Therefore the adjustment takes place somewhat

⁺ This is a standard result which can be found in Copson (1965). If $\omega''(k_s) = 0$ then the decay rate is $(\omega'''(k_s) t)^{-1/3}$. However it is easy to verify that $\omega''(k_s) \neq 0$ in our case.

slower than in the nondispersive case. There the adjustment time is simply $2\pi / (1 - F_d)$: the time necessary for a Kelvin wave to cross the obstacle.

The Kelvin mode is not needed to satisfy the initial conditions on v . However, it is needed to satisfy the initial condition

$$\eta(x, y, 0) = 0,$$

and this synthesis is described in Appendix C. In particular, it is shown that the Kelvin mode satisfies the same time-dependent equation and initial conditions that a long gravity wave would in the nonrotating analog of the problem. Therefore, Kelvin waves will propagate away from the obstacle as isolated packets for $F_d \neq 1$ and will contribute to upstream influence in the steady state left behind.

We have seen that the addition of dispersive waves adds interesting complications to the adjustment and that these features are associated with the idea of criticality. When the flow is subcritical with respect to the group velocity of a dispersive mode the topography causes a response which decays away upstream and downstream. When the flow is critical with respect to phase, the obstacle excites (possibly resonant) lee waves. Despite this, the global upstream influence that is basic to hydraulic control remains possible only when the flow is critical with respect to the Kelvin mode.

It is also interesting to compare the results in Figures 4.3 and 4.4 to Gill's (1976) solution to the dam-break problem (Figure 4.2). As noted earlier, the most striking feature of Gill's solution is the crossing of the boundary flow from the north to the south wall. We first observe that the subcritical solutions shown in Figures 4.3a and 4.4a exhibit no

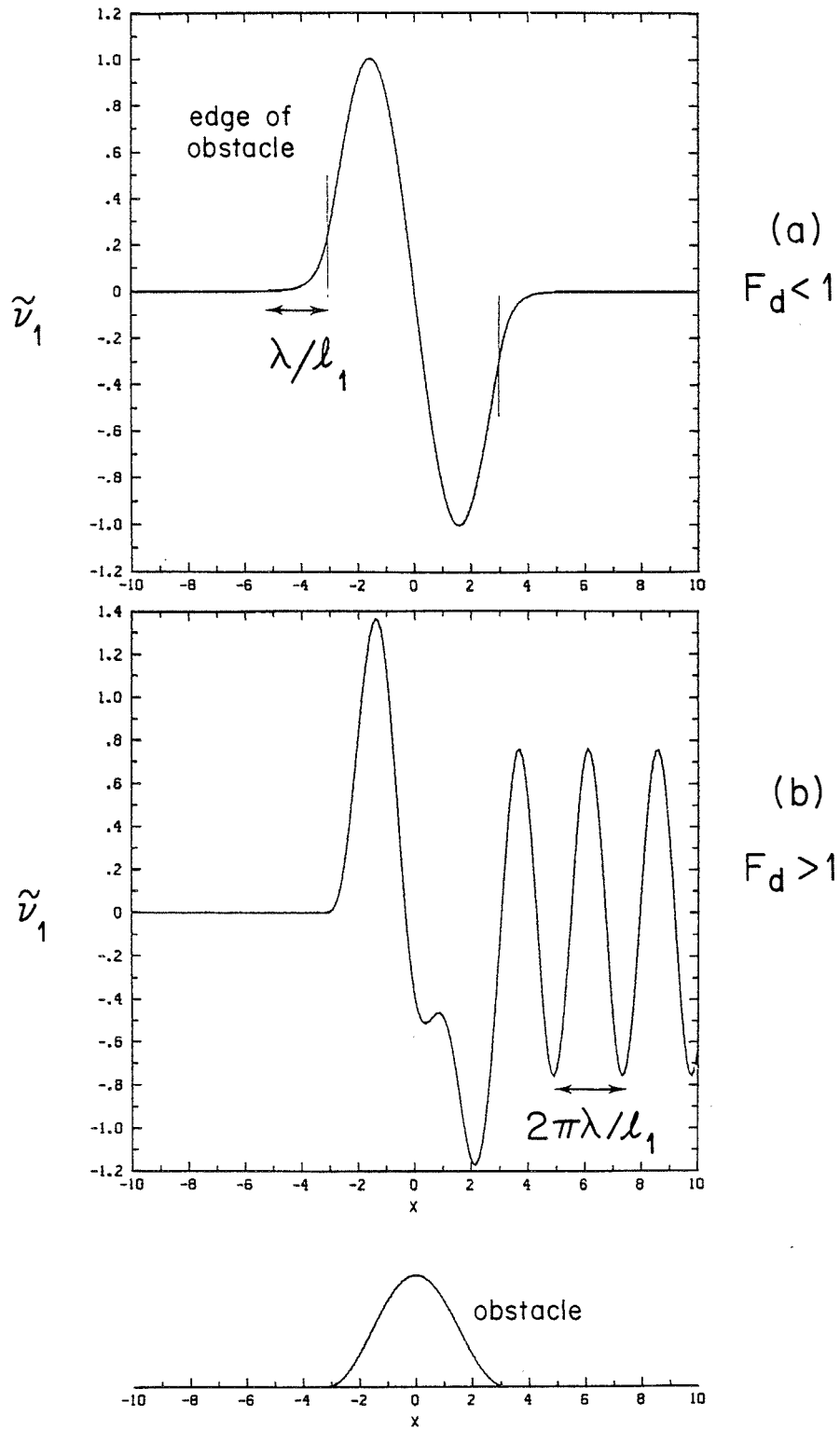


Figure 4.3

Cross-channel velocity at $y = 0$ for dispersive flow over obstacle.
 The mode $n = 1$ is shown.

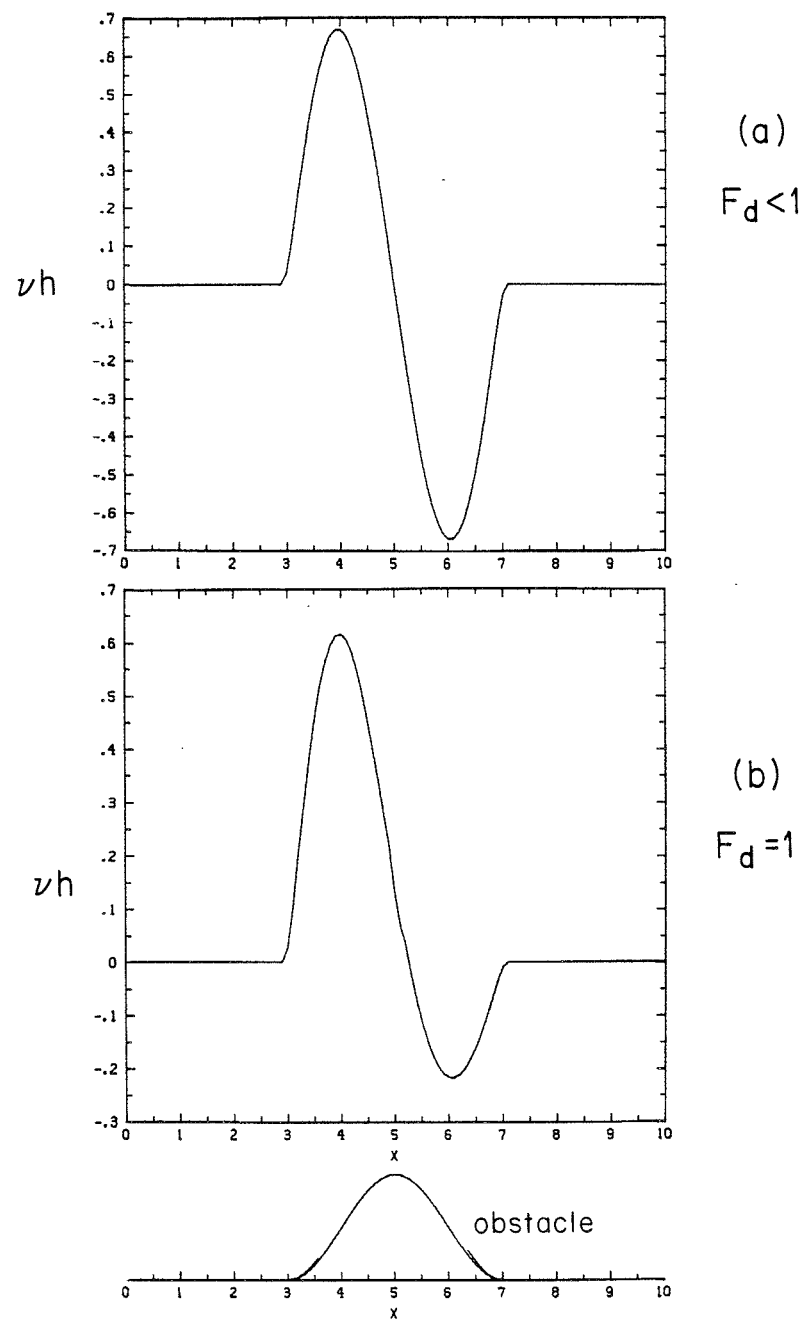


Figure 4.4

Cross-channel transport, b_h , for semigeostrophic flow. The controlled flow ($F_d = 1$) shows a net cross flow.

net crossing of streamlines from one side of the channel to the other. This is evidenced in each case by the symmetry of the cross stream transport, vh , with respect to the sill of the obstacle. In the transitional semigeostrophic flow of Figure 4.4b, however, the flow does exhibit a net transfer of mass flux as evidenced by the asymmetry of vh with respect to the sill. We might therefore associate the crossing of the stream in Gill's solution as evidence of hydraulic control and determine the crossing point as the position of the controlling obstacle.⁺ It is important to note, however, that the cross flow implied in Figure 4.4b is opposite in sense to that in Gill's solution. The downstream boundary layer structure of the flow is determined in a complicated way by the upstream fields and is not, as in Gill's solution, sensitive to the initial potential vorticity distribution.

⁺ It does not seem appropriate to make comparison between Gill's solution and the supercritical solution of Figures 4.3b as Gill's flow was subcritical.

5. Summary

In an attempt to understand the far field effects of deep straits and sills on unsteady abyssal currents, we have studied two problems: the adjustment of a steady current to a sudden change in bottom topography, and the oscillatory upstream forcing of a steady flow over topography. In the analysis special interest has been paid to the applicability of classical hydraulics concepts to the unsteady flows.

We first summarize the conclusions obtained from the results of adjustment problems, in which one of three basic flows is forced to adjust to a sudden change in the height of an obstacle. In the first case (Chapter 2) the basic flow is nonrotating and one-dimensional, while in the second (Chapter 3) the flow is semigeostrophic with constant potential vorticity. Both flows are described by quasilinear, hyperbolic systems of equations in one spatial dimension, allowing the adjustment to small topographic perturbations to be studied conveniently using characteristics. For large changes in topography, a Lax-Wendroff numerical scheme was used to obtain solutions. The third flow considered was a fully two-dimensional, rotating-channel flow and analytic solutions were obtained using equations linearized about the topography.

The adjustment problems reveal how far field influence is established by a topographic feature, such as an obstacle. The results depend to a certain extent on whether the flow is dispersive or nondispersive. In the nondispersive case (the flow is either one-dimensional or semigeostrophic) the obstacle must grow to a certain minimum height before any influence is felt in the surrounding flow fields. If the obstacle height is less than

the minimum required, then obstruction results only in the generation of isolated wave packets which radiate away and leave the neighboring flow unaffected. If the obstacle is grown to a larger height than the minimum, then bores are generated which propagate away from the obstacle and permanently change the neighboring flow fields, partially blocking the upstream flow. This blockage is eventually felt at infinity. Subsequent obstacle growth results in the generation of new bores which alter the neighboring fields, and we say that the obstacle exerts far field influence. Eventually the obstacle reaches a height at which the upstream flow is completely blocked.

In the nondispersive case, the blocking bore provides the means by which the obstacle exercises influence over the far field. If the basic flow is two-dimensional, as in the semigeostrophic case, then the bore can change the potential vorticity of the flow: this change is proportional to the differential rate of energy dissipation along the line of surface discontinuity. Because the bores are essentially breaking Kelvin waves which are banked against the solid channel boundaries, the magnitude of the surface discontinuity (and therefore the energy dissipation) normally decreases with distance from the wall. This allows predictions of the location and sign of potential vorticity change which are verified by numerical results.

If the flow is dispersive (supports Poincaré waves) then the far field influence of a small obstacle differs somewhat from the nondispersive. Because of the limitations imposed by the linear approximation, it is not possible to consider obstacles with height

greater than the critical height. In place of varying the obstacle height we vary the Froude number (based on the Kelvin wave speed) of the initial flow. If the initial flow is subcritical with respect to the Kelvin mode, then the obstacle causes response in the neighboring fluid which decays away from the obstacle. The decaying regions are set up by dispersive modes with near zero group velocity. If the flow is supercritical with respect to the Kelvin wave speed then the upstream response is nil but lee waves are formed behind the obstacle. In either case the obstacle exerts no influence over conditions far upstream, a property that is shared with the nondispersive flows over small obstacles.

The results suggest that it is always necessary to grow the obstacle to a certain finite height in order for upstream influence (hydraulic control) to occur. Based on the asymptotic states that were observed we can list some distinguishing features of controlled flows that might be used in observation work to decide whether or not a given sill exercises control over upstream conditions. In particular, the following are indicative of hydraulic control:

1. The flow is critical with respect to a nondispersive mode.
2. The upstream state is subcritical and the along-stream structure of the flow exhibits strong asymmetries with respect to the bottom elevation. Examples would be the crossing of the stream from one bank to the next or a change in the interface from its upstream basin level to a new downstream basin level.
3. A hydraulic jump downstream of the sill.

The second set of problems involves the oscillatory forcing at some upstream point of a steady, controlled flow. Since analytic solutions for oscillatory flows are generally unavailable, the investigation of this problem involves the use of characteristics and numerical results. Discussion is limited to nondispersive flows.

First considered is the situation in which the oscillations fail to disrupt the general configuration of the characteristic curves of the initial controlled flow. This configuration is distinguished by the x_+ characteristics, which diverge from the sill and connect the sill to all upstream and downstream points. When the flow over the obstacle becomes oscillatory, the divergence of x_+ characteristics occur about a dividing characteristic which oscillates about the sill (see Figure 2.10). The far field flow can now be traced back to the sill through x_+ characteristics which emanate from the neighborhood of the dividing characteristic. Numerical results verify that the far field influence of the obstacle, as computed in terms of time-averages, is similar to the influence the obstacle would have if the flow were steady.

The next question addressed concerns the ability of the forced oscillations to destroy the initial characteristic configuration by sweeping away the dividing characteristic. Numerical experiments suggest that the most effective way to accomplish this is to force the hydraulic jump (which normally exists in the lee of the sill) back upstream over the sill, so that subcritical conditions are created everywhere. Since jumps respond slowly (compared to the forced wave speed) to variations in upstream or downstream conditions, waves with low frequencies are required

to move the jump the required distance. Thus, low frequency waves were found to be the most effective disrupters of control.

An idea which deserves further mention is the relative stability of the steady controlled state to time-dependent disturbances. This property is implied by the diverging pattern of x_2 characteristics (Figure 2.4c) along which disturbances are spread (rather than focused). It is also present in the hysteresis effect (section 2.5) which tends to maintain the controlled state. Finally, the stability is enhanced by the sheltering effect of the obstacle as manifested in the strong dynamic balance and the ability to reflect appreciable ($c_r \geq .33$) amounts of energy upstream.

Because of numerical modeling difficulties (Appendix C) numerical tests with oscillatory flows were made only in the one-dimensional, nonrotating case. Although the general interpretations concerning far field influence are the same in both nonrotating and semigeostrophic systems, we can expect that local behavior of the waves near the obstacle will be quite different. For one thing, the reflection coefficients in the semigeostrophic case (section 3.10) can be much smaller than in the nonrotating case. Thus a greater amount of Kelvin wave energy can be expected downstream of the sill. Competing with this effect, however, is boundary layer effect, which places the transmitted Kelvin wave on the opposite wall as hydraulic jump. The jump is therefore protected from upstream forcing.

Based on the results from the work on nondispersive, oscillatory flows it is possible to make some observations concerning the applicability of classical hydraulics concepts to deep, unsteady strait

and sill flows within the assumed dynamical framework. If the flow is subcritical in the upstream basin and supercritical (with respect to a nondispersive mode) at some point within or downstream of the dividing strait, then the geometry of the strait is crucial in determining the flow in the neighboring basins. This is true whether or not the flow is unsteady, as the basin flow can in either case be traced back to a dividing characteristic within the strait. Furthermore, the flow configuration will be stable, even in the presence of violent upstream forcing, unless a jump exists near the dividing characteristic or the strait contains multiple sills or contractions of similar elevation or width. Therefore, the use of wier formulas is advisable only if the strait contains a single sill or side contraction.

Appendix A

Numerical Method

The numerical method used to model the one-dimensional flows of Chapter 2 is a finite-difference scheme introduced by Lax and Wendroff (1960) and discussed in the textbook of Roache (1972). The scheme is designed to simulate systems of equations written in conservation law form:

$$\frac{\partial w}{\partial t} + \frac{\partial G}{\partial x} + K = 0 . \quad (A1)$$

Where w , G , and K are vector-valued functions of the dependent and independent variables. Lax and Wendroff showed that the quantities conserved in (A1) will also be conserved in their difference equations (obtained from A1 through a Taylor expansion), even in the presence of shocks. If shocks occur in the solution, they are smeared over three or four grid points. Because of these features, the Lax-Wendroff method has been used successfully by a number of authors to compute solutions containing shocks. Roache (1972) gives an excellent review of the literature as well as a derivation of the difference equations.

The one-dimensional version of equations (3.7.1)-(3.7.3) are of the form A1. As we have seen, the conserved quantities implied by (3.7.1)-(3.7.3) are mass and momentum flux. The Lax-Wendroff scheme then tends to insure that the Rankine-Hugonit conditions (2.2.1)-(2.2.2) will be satisfied across the free-surface shocks of Chapter 2.

The initial value problem described in Section 2 was posed in the following manner: uniform values of the dependent variables were specified along 2,000 grid points. An obstacle centered between grid points 950 and 1050 was then grown quickly (within 20 time steps). The

resulting time-dependent motion was then computed with the end conditions (at grid points 1 and 2000) held constant. The computation was terminated before wave reflections from the end points reached the obstacle.

In the numerical solutions involving upstream or downstream forcing, the initial state consisted of a steady flow. The depth of fluid at one boundary was then varied sinusoidally about the initial depth. The corresponding velocity (or flow rate) at the boundary was then calculated using the values of the Riemann invariants carried to the boundary from the interior on characteristics. At the left boundary, for example, the Riemann invariant $R_- = u - 2h^{1/2}$ is specified by the interior. The velocity corresponding to forced values of $h(t)$ is thus $u = R_- + 2h^{1/2}(t)$. As above, the computation was terminated before reflections from the opposite end of the channel could affect the solution.

Solutions that are obtained using the Lax-Wendroff scheme frequently contain numerical oscillations that are due to nonlinear dispersive effects that result from the discretization. In the solutions of Chapter 2, these oscillations remained small, although the oscillations formed in the adjustment to a double sill (Figure 3.15 (b) and (c)) are close to being unacceptably large. The stability criterion (based on linear analysis) for the time step of the numerical scheme is

$$\Delta t < \Delta x / \lambda_{+ \max} \quad (A2)$$

where Δx is the grid spacing and $\lambda_{+ \max}$ is the maximum value of $\lambda_+ = u + h^{1/2}$. The value of $\Delta t / \Delta x$ used was typically between .2 and .4. Satisfaction of A2 prevented the computation from blowing up but did not prevent the short oscillations from forming.

It is possible to extend the original Lax-Wendroff method to two spatial dimensions, however the numerical scheme is extremely cumbersome and time consuming (Roache, 1972). A more economical version is a two-step variation of the Lax-Wendroff method introduced by Richtmeyer (1963). Instead of direct time stepping, the method requires an intermediate calculation to be done between each time step. Although less is known about the properties of the two-step difference equations, the method has been tested successfully in connection with shallow-water wave problems (Sielecki and Wurtele, 1970) and aerodynamic shock computations (Rubin and Burstein, 1967).

Unfortunately, the stability properties of two-dimensional, two-step Lax-Wendroff methods are worse than those of the one-dimensional method (Roache, 1972). For example, the numerical oscillations that occurred downstream of the free-surface shocks in the adjustment experiments of Chapter 3 initially proved to be unacceptably large. For this reason an artificial damping term of the form

$$\nu \frac{\partial}{\partial x} \left(h \frac{\partial u}{\partial x} \left| \frac{\partial u}{\partial x} \right| \right) \quad (A3)$$

was added to the x-momentum balance in order to damp disturbances with short wave lengths. The constant ν is a pseudo viscosity which typically had a value between 0.5 and 1.

Although A3 acts as a potential source of momentum, test runs showed the error in the x-momentum balance due to A3 to be negligible away from

⁺ This form was suggested by E. Isaacson (unpublished manuscript) in connection with a similar computation.

the shocks. Figures A1-A3 show a comparison between an artificially damped solution and an undamped solution obtained using identical initial conditions. In Figure A1 we show the undamped, one-dimensional adjustment of a subcritical flow to an obstacle. The solution is shown shortly after the obstacle appears and contains short numerical oscillations. Figure A2 shows the same problem, with the solution recomputed using $\nu = 1$. A superposition of the two results is shown in Figure A3.

Comparing the first two figures, we see that artificial damping has smoothed the shortest oscillations (which appear in A1 between grid points 150-200). The oscillations that trail the wave lying between $x = 300$ and $x = 350$ are somewhat longer and remain undamped in Figure A2. Also, the hydraulic jump that lies between $x = 170$ and $x = 180$ is smeared by the damping term as indicated by the higher surface elevation at the base of the jump in Figure A2. Finally, the basic structure of the flow away from the bump appears in Figure A3 to be unchanged by the damping. The two solutions are practically indistinguishable in most places.

The addition of the damping term A3 rendered the computation stable for 400 or 500 time steps, a period sufficient for adjustment to become complete within several obstacle lengths of the topography. For longer times, medium-length numerical oscillations grew without bound. These oscillations appear to be associated with the two-step method but not the original one-step method. It may be possible to use the one-step method without damping to compute solutions requiring long computation times.

The initial value problem was posed in the same manner as in the one-dimensional case, with a 15×400 grid forming the channel and the

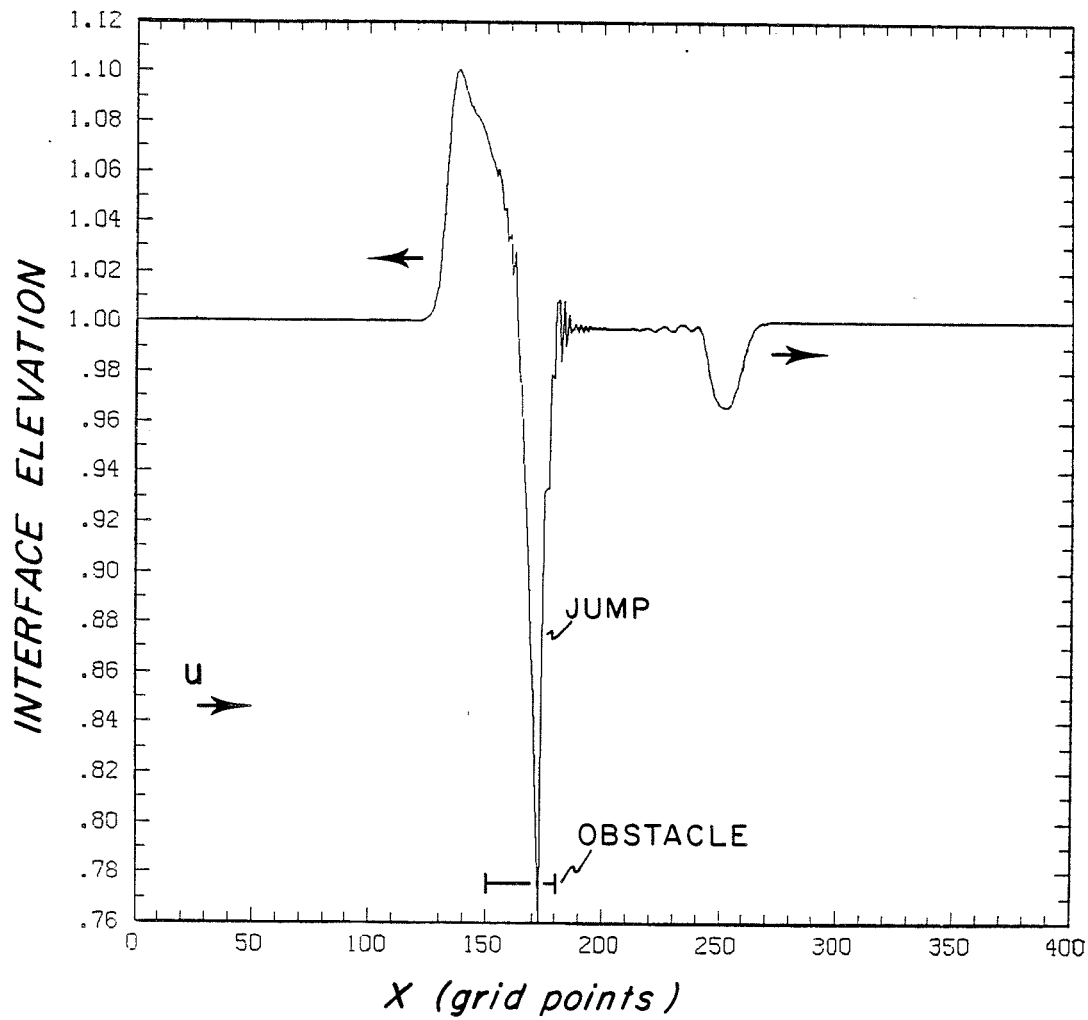


Figure A1

Nonrotating adjustment using two-step Lax-Wendroff method with $\nu = 0$.
(The obstacle is shown in Figure A3.)

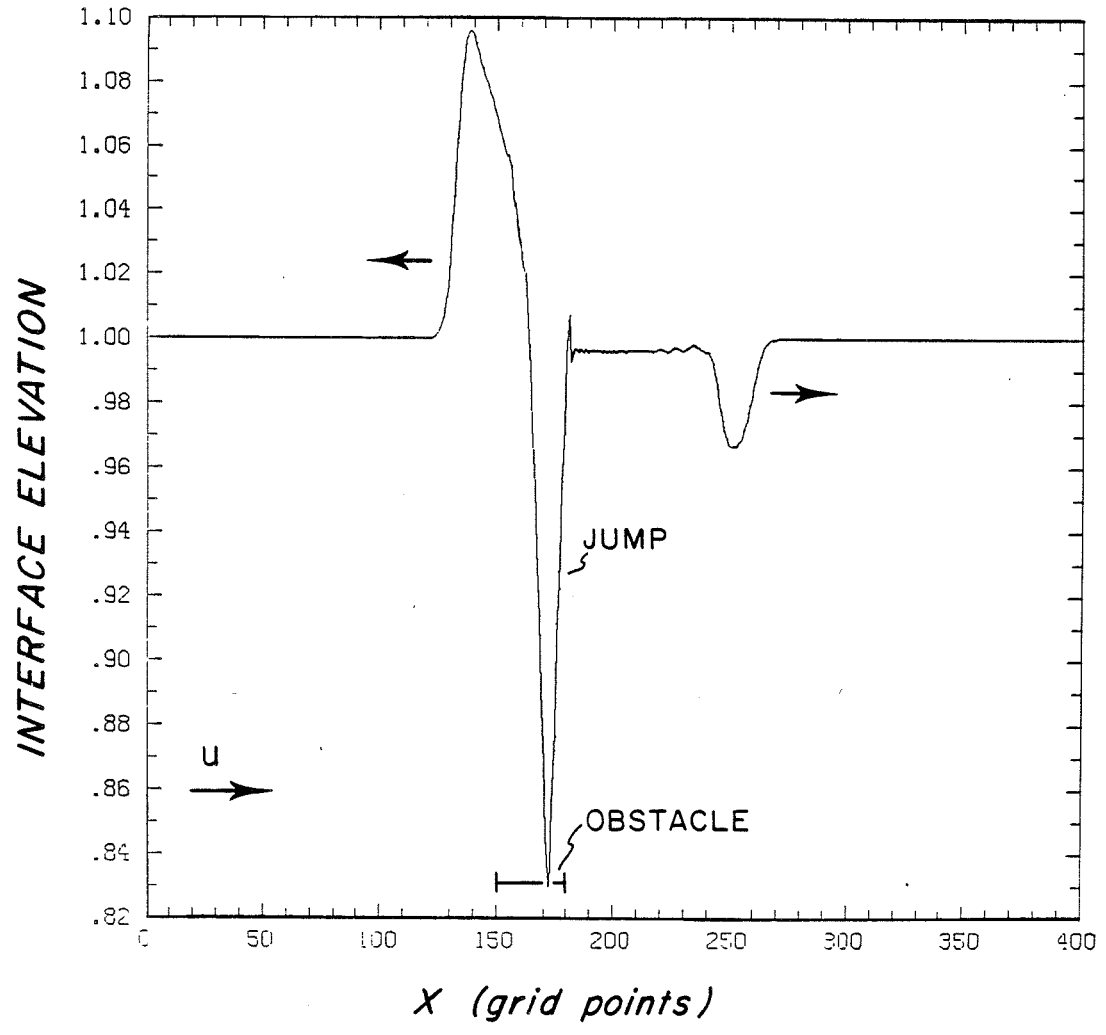


Figure A2

Damped version of solution. $\nu = 1$.

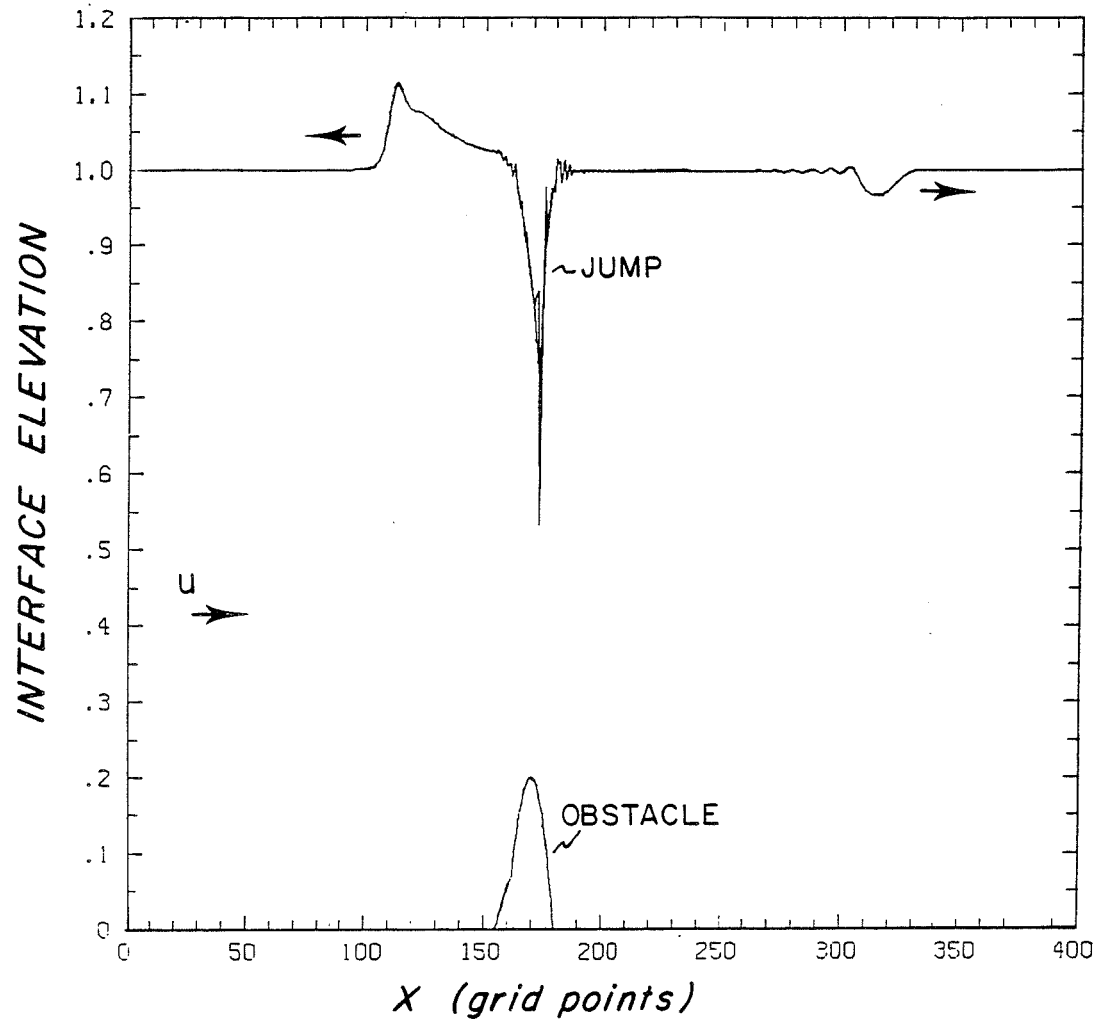


Figure A3

Superposition of results from Figures A1 and A2.

obstacle centered between rows 250 and 300. The side wall boundary conditions were imposed by setting $v = 0$ at side wall grid points and extrapolating from the interior values of u and h through a second order Taylor Expansion.

Appendix B

Proof That

$$G = u_+ h_+ - u_- h_- + QT^{-2} \bar{h}^{-2} (u_+ h_+ + u_- h_-) = 2[\bar{h} \phi^{-1/2} (T^{-1} - T^3) + \phi^{-3/2} (T^3 - T)]$$

Recall the identity derived in section 2.1:

$$\delta u = \phi^{1/2} T (\phi^{-1} - \bar{h}) , \quad (B.1)$$

along with the critical condition,

$$\phi^{1/2} T_c^{-1} Q \bar{h}_c^{-1} = \bar{h}_c^{1/2} [1 - T_c^2 (1 - \phi \bar{h}_c)]^{1/2} , \quad (B.2)$$

and the continuity condition

$$\delta h \bar{h} = -Q . \quad (B.3)$$

We first note that

$$u_+ h_+ - u_- h_- = 2(\delta u \bar{h} + \bar{u} \delta h)$$

$$u_+ h_+ + u_- h_- = 2(\delta u \delta h + \bar{u} \bar{h})$$

so that

$$G = 2[\delta u \bar{h} + \bar{u} \delta h + QT^{-2} \bar{h}^{-2} (\delta u \delta h + \bar{u} \bar{h})] \quad (B.4)$$

If the flow is critical, (B.1)-(B.3) can be used to express G in terms of \bar{h}_c alone. We first note that

$$\begin{aligned} \delta u \bar{h} + \bar{u} \delta h &= \phi^{1/2} T_c (\phi^{-1} - \bar{h}_c) \bar{h}_c - T_c \phi^{-1/2} \bar{h}_c [1 - T_c^2 (1 - \phi \bar{h}_c)] \\ &= \phi^{-1/2} T_c^3 \bar{h}_c - \phi^{1/2} (T_c + T_c^3) \bar{h}_c^2 . \end{aligned} \quad (B.5)$$

Also

$$\begin{aligned}
 QT^{-2}h_c^{-2}(\delta u_{sh} + \bar{u}\bar{h}) &= \phi^{-1/2}T_c^{-1}\bar{h}_c^{-1/2}[1 - T_c^2(1 - \phi\bar{h}_c)]^{1/2} . \\
 \left\{ -\phi^{1/2}T_c(\phi^{-1} - \bar{h}_c)(T_c\phi^{-1/2}\bar{h}_c^{1/2})[1 - T_c^2(1 - \phi\bar{h}_c)]^{1/2} \right. \\
 &\quad \left. + \bar{h}_c^{1/2}[1 - T_c^2(1 - \phi\bar{h}_c)]^{1/2}\bar{h}_c \right\} \\
 &= T^{-1}\phi^{-3/2}[1 - T_c^2(1 - \phi\bar{h}_c)] [\phi\bar{h}_c - T_c^2(1 - \phi\bar{h}_c)] \\
 &= T^{-1/2}T_c^{-1}\bar{h}_c + \phi^{1/2}T_c\bar{h}_c^2 - \phi^{-3/2}T_c + \phi^{-3/2}T_c^3 - 2\phi^{-1/2}T_c^3\bar{h}_c \\
 &\quad + \phi^{1/2}T_c^3\bar{h}_c^2 \quad (B.6)
 \end{aligned}$$

Combining B.5 and B.6 gives

$$G = 2[\bar{h}_c\phi^{-1/2}(T^{-1} - T^3) + \phi^{-3/2}(T^3 - T)]$$

Since $T \leq 1$, the sign of G depends on the magnitude of \bar{h}_c . We only consider flows which are not separated, so that

$$h_+ = \bar{h} + \delta h = \bar{h} - Q/\bar{h} \leq 0 ,$$

in implying that $\bar{h} \geq Q^{1/2}$. This can be used in B.2 to show that

$$\frac{\bar{h}_c}{\phi^{1/2}}(T^{-1} - T^3) \geq \phi^{-3/2}(T^3 - T)$$

Therefore, $G(\bar{h}_c) \geq 0$ for non-separated flows.

Appendix C Computing u and v from v

Since linear Kelvin waves are characterized by $v \equiv 0$, the solutions of Chapter 4 to (4.2.8) contain only Poincaré waves. To synthesize the

Kelvin mode we must compute either η or u . Following Gill (1976) we partition the dependent variables into odd and even parts. For example,

$$\eta(x, y, t) = \eta_{\text{odd}} + \eta_{\text{ev}}$$

where

$$\eta_{\text{odd}}(x, y, t) = \frac{\eta(x, y, t) - \eta(x, -y, t)}{2}$$

$$\eta_{\text{ev}}(x, y, t) = \frac{\eta(x, y, t) + \eta(x, -y, t)}{2}$$

The fact that both $b'(x)$ and $v(x, y, t)$ are even functions of y provides a great simplification. We start by breaking Equations (4.2.4)-(4.2.7) (with $F = 1$ and $\phi = 0$) into odd and even parts: this yields

$$\frac{d_o u_{\text{ev}}}{dt} - v = - \frac{\partial \eta_{\text{ev}}}{\partial x} - \frac{db}{dx}, \quad (\text{B1})$$

$$\frac{d_o u_{\text{odd}}}{dt} = - \frac{\partial \eta_{\text{odd}}}{\partial x}, \quad (\text{B2})$$

(from 4.2.4);

$$\frac{d_o v}{dt} + u_{\text{ev}} = - \frac{\partial \eta_{\text{odd}}}{\partial y}, \quad (\text{B3})$$

$$u_{\text{odd}} = - \frac{\partial \eta_{\text{ev}}}{\partial y}, \quad (\text{B4})$$

(from 4.2.5);

$$\frac{d_o \eta_{\text{ev}}}{dt} + \frac{\partial u_{\text{ev}}}{\partial x} = 0, \quad (\text{B5})$$

(from 4.2.6), and

$$\frac{\partial u_{\text{ev}}}{\partial y} = - \eta_{\text{odd}}, \quad (\text{B6})$$

$$\frac{\partial u_{\text{odd}}}{\partial y} - \frac{\partial v}{\partial x} = - \eta_{\text{ev}}. \quad (\text{B7})$$

(from 4.2.7).

If η_{ev} and u_{ev} can be found, then η_{odd} and u_{odd} can be computed directly using (B4) and (B6). We therefore start by finding η_{ev} and u_{ev} . Combining (B4) and (B7) gives the following equation for η_{ev} :

$$\frac{\partial^2}{\partial y^2} \eta_{ev} - \eta_{ev} = - \frac{\partial v}{\partial x} \quad (B8)$$

while (B3) and (B6) give a similar expression for u_{ev} :

$$\frac{\partial^2}{\partial y^2} u_{ev} - u_{ev} = \frac{d_0 v}{dt} \quad (B9)$$

Using the fact that $v = \sum_{n=0}^{\infty} \tilde{v}_n(x,t) \cos \left[\frac{(2n+1)}{2} \pi y \right]$, we can find the following solutions to (B8) and (B9):

$$\eta_{ev} = \sum_{n=0}^{\infty} \frac{\partial \tilde{v}_n}{\partial x} \left[\frac{(2n+1)^2 \pi^2}{4} + 1 \right]^{-1} \cos \left[\frac{(2n+1)}{2} \pi y \right] + N(x,t) \cosh(y) \quad (B10)$$

$$u_{ev} = \sum_{n=0}^{\infty} - \frac{d_0 \tilde{v}_n}{dt} \left[\frac{(2n+1)^2 \pi^2}{4} + 1 \right]^{-1} \cos \left[\frac{(2n+1)}{2} \pi y \right] + U(x,t) \cosh(y) \quad (B11)$$

At $t = 0$, we have $v = \tilde{v}_n = u = \eta = 0$. It follows that u_{ev} and η_{ev} as well as u_{odd} and η_{odd} must be initially zero. Hence,

$$N(x,0) = U(x,0) = 0 \quad (B12)$$

Substituting (B10) into (B1) and (B5), applying the result at either wall (where $\cos \left[\frac{(2n+1)}{2} \pi y \right] = 0$) and combining the result leads to a wave equation for $N(x,t)$:

$$\frac{d_0^2 N}{dt^2} - \frac{\partial^2 N}{\partial x^2} = \frac{d^2 b}{dx^2} \quad (B13)$$

The same procedure can be followed to obtain a single equation for U , the result being

$$\frac{d_o^2 U}{dt^2} - \frac{\partial^2 U}{\partial x^2} = - F_d \frac{d^2 b}{dx^2} \quad (B14)$$

B13 and B14 are the same equations that govern the nonrotating, one-dimensional analog of the adjustment problem, with N and U the total depth and velocity perturbations. The solutions can be written

$$N(x,t) = b/(F_d^2 - 1) + \int_0^\infty \frac{G_2(k)}{2} [\cos k (x - (F_d - 1)t) + \cos k (x - (F_d + 1)t)] dk \quad (B15)$$

$$U(x,t) = - F_d b/(F_d^2 - 1) + \int_0^\infty \frac{G_2(k)}{2} [\cos k (x - (F_d - 1)t) + \cos k (x - (F_d + 1)t)] dk \quad (B16)$$

where $G_1(k)$ and $G_2(k)$ are determined in terms of the topography by (B12) and (4.2.11):

$$G_2(k) = \frac{-1}{\pi(F_d^2 - 1)} \int_{-\infty}^\infty \cos(kx) b(x) dx = \frac{-2k \sin \pi k}{\pi(F_d^2 - 1)(1 - k^2)} \quad (B17)$$

$$G_2(k) = \frac{F_d}{\pi(F_d^2 - 1)} \int_{-\infty}^\infty \cos(kx) b(x) dx = \frac{2F_d k \sin \pi k}{\pi(F_d^2 - 1)(1 - k^2)} \quad (B18)$$

and where the integrals have been evaluated with the aid of Gradshteyn and Ryzhik (1965).

Finally, the odd parts of η and u can be computed from (B4) and (B6) as

$$\eta_{\text{odd}} = - \frac{\partial u}{\partial y} = \sum_{n=0}^{\infty} \frac{d_o \tilde{v}_n}{dt} \left[\frac{(2n+1)}{2} \pi \right] \left[\frac{(2n+1)^2}{4} \pi^2 + 1 \right]^{-1} \sin \left[\frac{(2n+1)}{2} \pi y \right] \quad (B19)$$

- $U(x,t) \sinh y$

$$u_{\text{odd}} = - \frac{\partial \eta_{\text{ev}}}{\partial y} = - \sum_{n=0}^{\infty} \frac{\partial \tilde{v}_n}{\partial x} \left[\frac{(2n+1)}{2} \pi \right] \left[\frac{(2n+1)^2}{4} \pi^2 + 1 \right]^{-1} \sin \left[\frac{(2n+1)}{2} \pi y \right] \quad (\text{B20})$$

$$- N(x,t) \sinh y .$$

The complete solutions are obtained by combining (B19) and (B20) with (B10) and (B11). It is easy to verify that η and u satisfy the boundary condition

$$u = - \frac{\partial \eta}{\partial y} \quad (x = \pm 1)$$

implied by (4.2.5) with $v = \frac{db}{dy} = 0$. Taking odd and even parts of the above equation, we find

$$u_{\text{odd}} = - \frac{\partial}{\partial y} \eta_{\text{ev}} \quad (x = \pm 1)$$

$$u_{\text{ev}} = - \frac{\partial}{\partial y} \eta_{\text{odd}} \quad (x = \pm 1) .$$

However these are identical to B4 and B5, which have been used to calculate η_{odd} and u_{odd} . Hence, the boundary conditions are automatically satisfied.

References

- Baines, P. O., and P. A. Davies (1980) Laboratory studies of topographic effects in rotating and/or stratified fluids. In Orographic Effects in Planetary Flows, GARP Pub. Ser. No. 23, World Met. Org.
- Blumen, W. (1972) Geostrophic adjustment. Rev. Geophys., 10, 485-528.
- Chow, V. T. (1959) Open-Channel Hydraulics, McGraw-Hill, New York.
- DaFermos, C. M. (1974) Quasilinear hyperbolic systems that result from conservation laws. In: Nonlinear Waves, S. Leibovich and A. R. Seebass (editors), Cornell University Press, pp. 82-100.
- Gill, A. E. (1976) Adjustment under gravity in a rotating channel. J. Fluid Mech., 77, 603-621.
- Gill, A. E. (1977) The hydraulics of rotating-channel flow. J. Fluid Mech., 80, 641-671.
- Gradshteyn, I. S., and I. M. Ryzhik (1965) Tables of Integrals Series and Products, Academic Press, New York.
- Houghton, D. D., and A. Kasahara (1968) Nonlinear shallow fluid flow over an isolated ridge. Comm. Pure Appl. Math., 21, 1-23.
- Hoskins, B. J., and F. P. Bretherton (1972) Atmospheric frontogenesis models: Mathematical formulation and solution. J. Atmos. Sci., 29, 11-37.
- Lax, P., and B. Wendroff (1960) Systems of conservation laws. Comm. Pure Appl. Math., 13, 217-237.
- Long, R. R. (1953) Some aspects of the flow of stratified fluids II, Experiments with a two-fluid system. Tellus, 5, 42-58.
- Pedlosky, J. (1979) Geophys. Fluid Dyn., Springer-Verlag, New York.

- Rayleigh, Lord (1914) On the theory of long waves and bores. Proc. Roy. Soc. London, Ser. A, Vol. 90.
- Richtmyer, R. D. (1963) A survey of difference methods for nonsteady fluid dynamics. NCAR Tech. Note 63-2. Boulder, Colorado.
- Roache, P. J. (1972) Computational Fluid Dynamics, Hermora, Albuquerque, New Mexico.
- Rubin, E. L., and S. Z. Burstein (1967) Difference methods for the inviscid and viscous equations of a compressible gas. J. Comp. Phys., 2, 178-196.
- Sielecki, A., and M. G. Wurtele (1970) The numerical integration of the nonlinear shallow-water equations with sloping boundaries. J. Comp. Phys., 6, 219-236.
- Smith, R. B. (1981) The influence of mountains on the atmosphere. Adv. in Geophys., 21, 87-230.
- Stalcup, M. C., and W. G. Metcalf (1975) Deep Caribbean inflow through the Anegada-Jungfern Passage. J. Mar. Res., Supplement to 33, 15.
- Stern M. E. (1974) Comment on rotating hydraulics. Geophys. Fluid Dyn., 6, 127-130.
- Stoker, J. J. (1957) Water Waves, Interscience, New York.
- Whitehead, J. A., Jr. (1974) Rotating hydraulics of strait and sill flows. Geophys. Fluid Dyn., 6, 101-125.
- Whitham, G. B. (1974) Linear and Nonlinear Waves, John Wiley and Sons, New York.
- Worthington, L. V. (1969) An attempt to measure the volume transport of Norwegian Sea overflow water through the Denmark Strait. Deep-Sea Res., Supplement to 16, 421-433.